The near-infrared activity of Sagittarius A*

INAUGURAL-DISSERTATION

zur
Erlangung des Doktorgrades
der Mathematisch-Naturwissenschaftlichen Fakultät
der Universität zu Köln

vorgelegt von

Leonhard Meyer
aus Düsseldorf

Köln 2008

Berichterstatter:	Prof. Dr. Andreas Eckart Prof. Dr. Claus Kiefer

Tag der mündlichen Prüfung: 9. Januar 2008

Zusammenfassung

Das Ziel meiner Doktorarbeit war es, neue Erkenntnisse über die Eigenschaften des supermassiven Schwarzen Loches im Zentrum unserer Milchstraße und seinen Akkretionsfluss zu gewinnen. Die nicht-thermische Radio-, Nahinfrarot- und Röntgenquelle Sagittarius A* (Sgr A*) ist die elektromagnetische Manifestation des Schwarzen Loches. Sgr A* ist eine einzigartige Quelle zur Erforschung von Akkretion auf ein sehr massives kompaktes Objekt, da es den mit Abstand nächsten Galaxienkern bildet.

Für diese Arbeit habe ich sowohl Beobachtungen als auch theoretische Berechnungen durchgeführt. Für die Beobachtungen wurde die Nahinfrarotkamera CONICA in Verbindung mit dem System für adaptive Optik, NAOS, am Very Large Telescope der Europäischen Südsternwarte verwendet. Hierbei war das Ziel unseres Teams ganz konkret, weitere Hinweise für ein quasi-periodisches Signal von $\sim$17 Minuten in Strahlungsausbrüchen zu finden, welches 2003 zum ersten Mal beobachtet wurde. Die Strahlungsausbrüche – meistens als ,,flare“ bezeichnet – sind Ereignisse von $\sim$50-130 Minuten Länge, während derer der Fluss von Sgr A* im Nahinfraroten bis zu einem Faktor zehn ansteigt und wieder abfällt. Das periodische Signal äußert sich dabei in Form von Spitzen, die in annähernd konstantem Abstand auftreten. Sowohl 2005 als auch 2006 konnten wir erneut eine statistisch signifikante Periodizität finden und damit das vorherige Ergebnis bestätigen. Darüber hinaus haben wir polarimetrische Messungen der Strahlungsausbrüche im Nahinfraroten durchgeführt. Diese bieten die Möglichkeit, nach Spuren der starken Krümmung der Raumzeit in der Nähe des Ereignishorizontes von Sgr A* zu suchen und seine Parameter einzuschränken.

Um dies zu erreichen, habe ich als Modell für die Periodizität ein kreisendes, kompaktes Plasma-Paket gewählt, ein beschränktes, zusammenhängendes Gebiet innerhalb des Akkretionsflusses, das heller als seine Umgebung ist. Ein solcher ,,Blob“ kann z.B. durch magnetische Rekonnektion erzeugt und durch Magnetfeldeffekte zusammengehalten werden. Es ist klar, dass der Blob eine Umlaufbahn nahe des Ereignishorizontes haben muss, um mit der Zeitskala von $\sim$17 Minuten konsistent zu sein. In der Nähe des Ereignishorizontes sind aber Effekte der Allgemeinen und Speziellen Relativitätstheorie

wie z.B. Dopplerverschiebungen, Lensing, Aberration und die Rotation des elektrischen Feldvektors der Strahlung von enormer Wichtigkeit. Um alle diese Effekte zu berücksichtigen, führte ich relativistische Ray-tracing Rechnungen durch, wobei ich auf dem KY Code der Astrophysik-Gruppe am tschechischen Institut der Wissenschaften in Prag aufbauen konnte.

Nun war ich in der Lage, die beobachtete Variabilität des Flusses, des Polarisationswinkels und des Polarisationsgrades zu fitten. Dabei konnte ich zeigen, dass das Modell eines Plasma-Paketes in der Nähe des Ereignishorizontes eine exzellente Beschreibung der Daten darstellt. Obwohl das Modell in seiner verwendeten Form noch recht simpel ist – es wurde die Hydrodynamik des Blobs vernachlässigt und das Hauptgewicht auf die relativistischen Effekte gelegt – liefert es sehr gute Fits an die Beobachtungen. Die Berechnung von Konfidenzkonturen erlaubte es mir, einen großen Bereich des Parameterraumes für Sgr A* auszuschließen. So konnte ich den dimensionslosen Spinparamter auf $a_\star \geq 0.5$, die Inklination auf $i \geq 25°$ und die Orientierung der Normalen zur Äquatorialebene des sich drehenden Schwarzen Loches auf $60° \leq \theta \leq 105°$ (von N nach O gemessen am Himmel) auf einem 3σ-Niveau beschränken.

Abstract

The meaning of my thesis was to obtain new insights about the supermassive Black Hole in the center of our Milky Way and its accretion flow. The non-thermal radio, X-ray, and near-infrared source Sagittarius A* (Sgr A*) is the electro-magnetic manifestation of the Black Hole. Sgr A* is a unique source to study the accretion onto a very massive compact object as it is the closest galactic nucleus.

For this work I conducted observations as well as theoretical computations. The near-infrared camera CONICA in combination with the adaptive optics device NAOS at ESO's Very Large Telescope in Chile were used for the observations. The goal of our group was in particular to find further evidence for a quasi-periodic signal of ~ 17 minutes in radiation outbursts from Sgr A* that has been reported for the first time in 2003. The radiation outbursts – most often termed 'flares' – are periods of $\sim 50 - 130$ minutes in which the flux of Sgr A* in the near-infrared rises up to a factor of ten. The quasi-periodic sub-structure thereby manifests itself as sub-flares with a constant separation superimposed on the larger, underlying flare. In 2005 and 2006 we were able to detect a significant periodicity, hence the previous findings are supported. Furthermore, we conducted polarimetric measurements of the radiation outbursts in the near-infrared. They offer the unique possibility to look for traces of spacetime curvature close to the event horizon of Sgr A* and to constrain its parameters.

In order to achieve this, I have chosen the model of a relativistically orbiting plasma blob to fit the observed polarimetric lightcurves. Such a confined and coherent plasma region which is brighter than the rest of the accretion flow may be created e.g. via magnetic reconnection. It is obvious that such an 'hot spot' has to orbit very close to the event horizon in order to match the timescale of $\sim 17\,\mathrm{min}$. In this region the effects of Special and General Relativity like e.g. Doppler shifts, lensing, aberration and the change of the polarization vector of the emitted radiation are of enormous importance. To take all these effects into account, relativistic ray tracing computations are needed. I conducted such calculations using the KY code of the Astrophysics group at the Czech Institute of Sciences in Prague.

Having a model and the methods at hand, I was able to fit the observed variability in the flux, the polarization angle and the polarization degree of Sgr A*. I showed that the model of an orbiting hot spot leads to an excellent description of the data. Although I neglected the (unknown) detailed hydrodynamics of the blob and put the major role on the relativistic effects, the model fits the observations well. Furthermore, the calculation of confidence contours allowed to exclude a big part of the parameter space for Sgr A*. I was able to constrain the dimensionless spin parameter to $a_\star \geq 0.5$, the inclination to $i \geq 25^\circ$, and the position angle of the normal to the equatorial plane of the Black Hole to $60^\circ \leq \theta \leq 105^\circ$ on a 3σ level.

Contents

1 Introduction **11**

1.1 The Galactic center region across the wavelengths 11

1.2 The nuclear star cluster and stellar orbits 15

1.3 Sagittarius A* 21

1.3.1 The radio source Sgr A*: proper motion and source structure 21

1.3.2 Sgr A*'s spectrum and accretion models 23

1.3.3 Polarization 26

1.3.4 Flares 27

1.4 This thesis 31

2 Observations and data reduction **33**

2.1 Near-infrared observations of the Galactic center 33

2.2 Standard data reduction 39

3 Quasi-periodicities in near-infrared flares from Sgr A* 45

3.1 A QPO in the 2003 lightcurve from Sgr A*? 45

3.2 Polarimetric measurements of Sgr A* 50

3.2.1 The observations from 2006 50

3.2.2 The observations from 2005 54

4 The Kerr metric and observables 59

4.1 The general theory of relativity 59

4.2 The spacetime around a spinning black hole 62

4.3 The concept of a transfer function 67

5 A plasma blob close to the Black Hole horizon 73

5.1 The underlying disk 73

5.2 The hot spot 75

5.3 Magnetic fields and foreground polarization 78

5.4 The fitting procedure and the treatment of higher order images 80

5.5 Results 82

5.5.1 The 2005 data 82

5.5.2 The 2006 data 85

6 On the orientation of the Sgr A* system 91

6.1 Introduction 91

6.2 The data and their reduction 92

6.3 The mean polarization angle 94

6.4 The three dimensional orientation of the Sgr A* system . . 96

7 Summary and outlook 101

Bibliography 107

List of Abbreviations 115

List of Figures 117

Acknowledgements 121

Erklärung 123

Chapter 1

Introduction

Approximately 8 kpc away from us lies the center of our galaxy, the Milky Way. It is the closest galactic nucleus and therefore serves as a template for these kinds of objects – very similar to the outstanding role our sun plays in stellar physics. This introduction briefly describes some unique phenomena that are being met in the Galactic center and also gives necessary background for the following chapters. General introductory references are the books by Eckart et al. (2005) and Melia (2007).

1.1 The Galactic center region across the wavelengths

This thesis focuses on the Black Hole (identified with the electromagnetic source Sgr A*) itself. Before plunging in medias res, however, we will have a brief look at the Galactic center (GC) structures on a larger scale.

Fig. 1.1 shows a 265×200 pc mosaic of the GC at wavelengths of $3.6-8.0\,\mu$m (Stolovy et al., 2006). It shows nicely the richness of phenomena that can be discovered in the Galactic nucleus. In the center of the image the nuclear star cluster around the supermassive Black Hole (SMBH) can be seen. Its structure and properties will be described in the next section. Dark

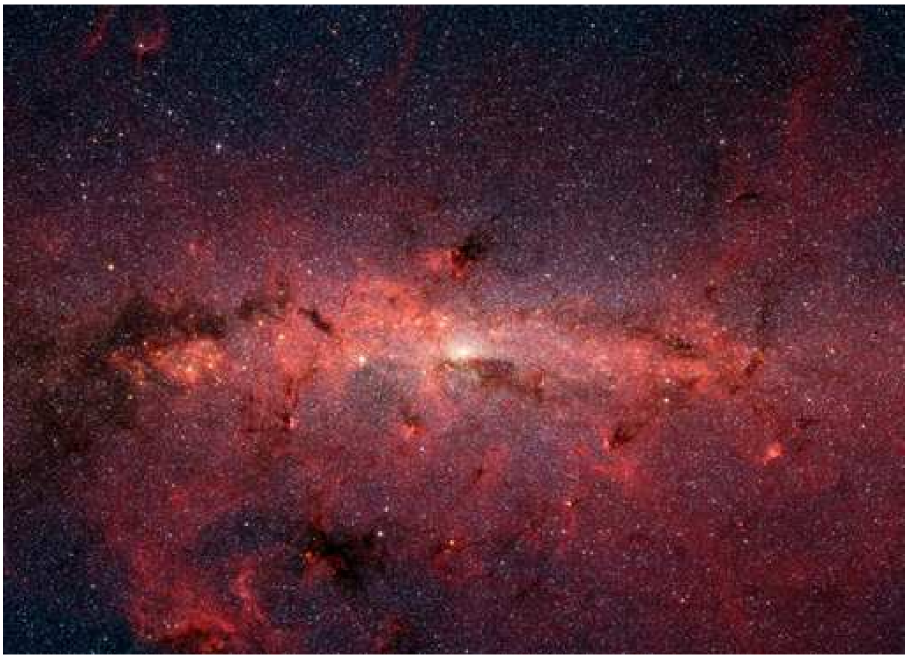

Figure 1.1: *Mosaic of the central* $2^\circ \times 1.5^\circ$ *(*265×200 *pc) of the Milky Way at* $3.6 - 8.0\,\mu m$*. Galactic east is left and north is up. From Stolovy et al. (2006).*

patches trace molecular clouds that absorb the radiation at this frequency. Extinction is also the reason why the GC cannot be observed in the optical. The attenuation of visible light towards the GC amounts to a factor of 10^{-12}. The gas and dust on the line of sight to the center allows only observations in the radio, infrared and X-ray regime.

Besides the BH itself, the surrounding nuclear star cluster and the dense molecular clouds, structural elements of this region of the Galaxy include massive star clusters, several supernova remnants, and a dense, clumpy molecular ring (the so called circum nuclear disk) that orbits the nucleus on scales of a few parsecs. Inside this ring lies a three arm structure of ionized gas that connects the circum nuclear disk with the center of the star cluster. Due to its projected appearance, these gas streams are termed mini-spiral. It can be seen in Fig. 1.2, in which we have now zoomed into the very center of our Galaxy and also changed the observing wavelength. Fig. 1.2 was taken with the Very Large Array at 6 cm, i.e. in the radio range.

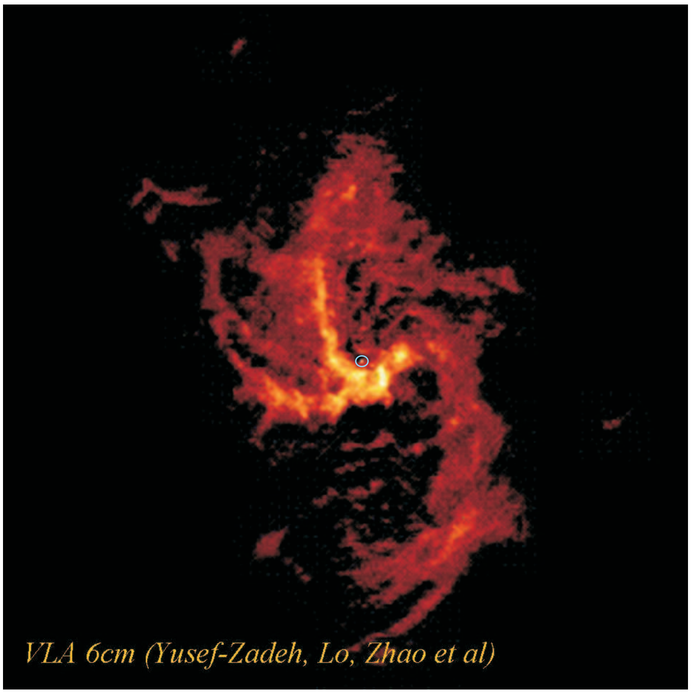

Figure 1.2: *The mini-spiral (Sgr A West) with its three arm structure. Each arm is about three light years in length. The spot in the center of the image, marked with a blue circle, is the radio source Sgr A* identified with a* $3.6 \times 10^6\, M_\odot$ *black hole.*

It was also the radio range in which Sgr A* was discovered in 1974 (Balick & Brown, 1974). The bright radio complex Sagittarius A could be resolved into a nonthermal shell source (Sagittarius A East) which is most likely a supernova remnant, an extended source (named Sagittarius A West) that can be identified with the mini-spiral seen in Fig. 1.2, and a bright radio source with an extent of less than one arcsecond. Due to its compactness, this source was later termed Sagittarius A*. As a high brigthness temperature and small angular size were observed, it was immediately clear that it is a unique astronomical target. In Fig. 1.2, Sgr A* can be seen as the small, bright spot in the center of the image. This central part of the Galaxy is shown again in a magnified view in Fig. 1.3, now at a wavelength of 13 mm. Sgr A* clearly stands out as an one-of-a-kind source in this region.

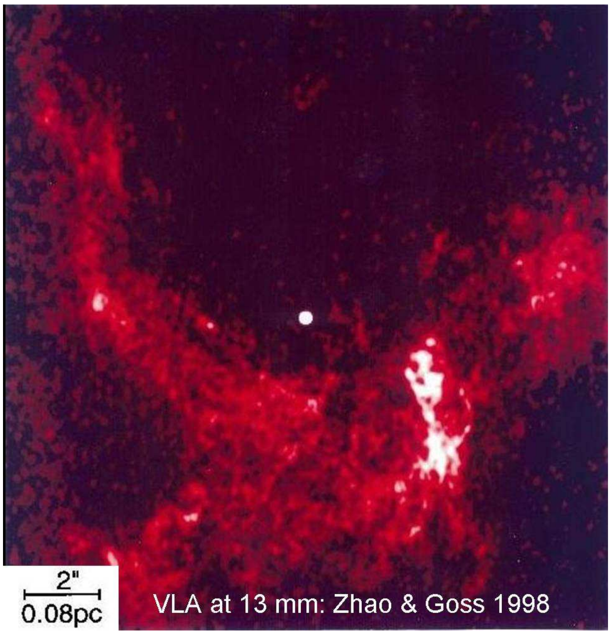

Figure 1.3: *The central part of the mini-spiral and Sgr A*. From Zhao & Goss (1998).*

The highly ionized gas making up the mini-spiral is not standing still. At a distance of roughly three light years from the center, the plasma moves at a velocity of ~ 100 km/s. If the plasma is in Keplerian rotation around the center, this requires a mass concentration of $\sim 3.5 \times 10^6\,\mathrm{M}_\odot$ inside this radius, giving evidence for the Black Hole nature of Sgr A* (see also Schödel et al., 2007, for recent refined mass estimates). To probe the mass distribution inside smaller radii, the near-infrared (NIR) domain – where stars are visible – is ideally suited.

An image taken in this part of the electromagnetic spectrum is shown in Fig. 1.4. More precisely, this is a three color composite so that a wavelength range of $\lambda = 1.5 - 4\,\mu$m is covered. In Fig. 1.4, red stands for the lower frequency and blue for the higher frequency emission. The mini-spiral can only be seen at longer wavelengths, whereas the stars that are not embedded in dust are visible at shorter wavelengths. The properties of the nuclear star cluster seen in Fig. 1.4, i.e. the spectral types of the stars and their radial and proper motions, will be described in the next section.

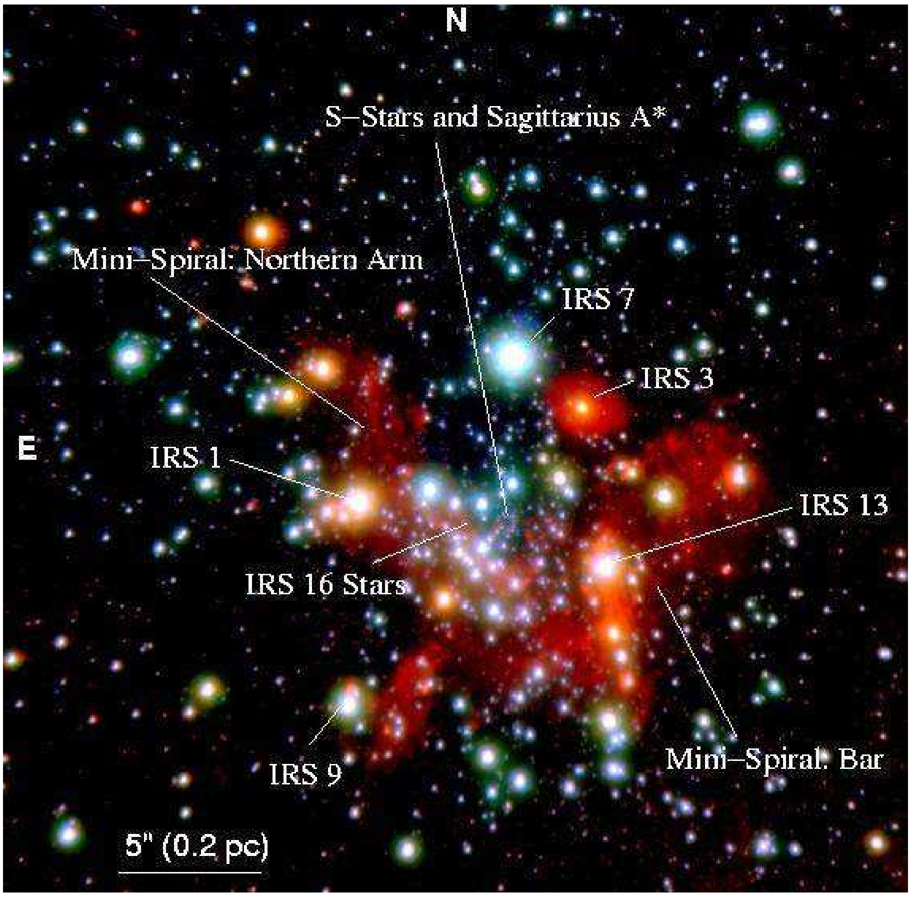
N
S–Stars and Sagittarius A*
Mini–Spiral: Northern Arm
IRS 7
IRS 3
E
IRS 1
IRS 13
IRS 16 Stars
IRS 9
Mini–Spiral: Bar
5" (0.2 pc)

Figure 1.4: *Near-infrared composite ($\lambda = 1.5 - 4\,\mu m$) of the Galactic center. The most prominent sources are labed (IRS stands four Infra Red Source). Sgr A* itself can in general not be seen in the near-infrared images. This image was taken with NACO at Eso's VLT (see Chapter 2 for details). From the GC webpages of the I. Physikalisches Institut, University of Cologne.*

1.2 The nuclear star cluster and stellar orbits

Fig. 1.4 shows that the IRS 16 cluster stars (most of them are probably blue supergiants) and IRS 7 (a red supergiant) dominate the NIR luminosity in the central few arcseconds. Only recent advances in high-resolution imaging techniques like Speckle imaging and/or adaptive optics (see Chapter 2) allowed to study this crowded field in detail. Despite the so far achieved technical sophistication, one has to keep in mind that only stars with magnitudes up to ~ 18 in the K-band (centered at $2.2\,\mu$m) can be observed today. This range includes all red and most blue supergiants, all red giants, and all main sequence stars down to roughly $2\,\mathrm{M}_\odot$. So, images as the one in Fig. 1.4 sample only a fraction of $\sim 1\%$ of the total stellar content of the cluster.

The central star cluster of our Galaxy is *the* template of a star cluster around a SMBH. Due to its proximity, it is the only cluster in the center of a galaxy that can be resolved into individual stars. Important theoretical questions concerning stellar dynamics and star formation under the influence of a SMBH can therefore only be studied in the center of the Milky Way.

At first we want to take a look at the old, underlying, dynamically relaxed stellar population. As the relaxation time is roughly $4 \cdot 10^8$ years, it can be expected that the older stars are in a relaxed equilibrium configuration. How should the equilibrium stellar volume density around a SMBH look like? Further out, i.e. outside the so-called sphere of influence of the BH defined as a spherical volume with a radius $R = GM/\sigma^2$, with σ being the velocity dispersion (root mean square) of the cluster, the stellar density follows a quasi-isothermal profile. This means that the stellar distribution can be characterized by a single energy variable – equivalent to the temperature in a gas – and that it behaves like r^{-2} (see, e.g., Binney & Tremaine, 1987). But inside the sphere of influence, which is ~ 3 pc in the case of the Galactic center, the presence of the SMBH becomes noticeable.

With its extremely strong gravitational field the SMBH destroys and swallows individual stars that come too close to it. The energy thereby gained by the cluster is ported outwards via relaxation among the inner stars. The BH acts as a sink in phase space, removing stars on certain trajectories. This alters the distribution of the inner stars. A so-called cusp emerges. This is a distribution that – formally – diverges at the origin. In a pure isothermal profile without a BH in the center the $1/r^2$ shape would continuously change into a constant plateau for small r. This can be described with a function of the form $\rho \propto (1 + r/r_c)^{-2}$, where r_c is the core radius and

$0 < r < \infty$. A cusp, on the other hand, can be described by a power-law with an non-zero exponent, $\rho \propto r^{\gamma}$, for small r. As a cusp is confined to a region close to the SMBH, and further out an isothermal profile ($\rho \propto r^{-2}$, for big r) is thought to be applicable, a broken-power law should describe the stellar distribution in the nuclear cluster.

Indeed, in a recent study Schödel et al. (2007) could confirm previous findings (Genzel et al., 2003b) that the stellar density in the cluster at the Galactic center can be described by a broken power-law (see Fig. 1.5). A constant plateau in the inner few arcsecs is clearly ruled out. Although cusps can also be generated by other mechanisms than the one sketched above, this finding is interpreted as a clear fingerprint of the SMBH identified with Sgr A*.

Surprisingly, within the stellar cusp not only old, relaxed, low-mass stars but also unrelaxed, apparently young stars with masses of 30-100 $\mathrm{M}_{\odot}$ can be found. These objects are often called He-stars, as they emit strong HeI lines in their outer atmosphere. These stars, of which the IRS 16 cluster seen in Fig. 1.4 is an example, appear to be members of the blue supergiant variety, i.e. stars that have an initial mass $> 40\,\mathrm{M}_{\odot}$ and have evolved off the main sequence (e.g. Krabbe et al., 1995). Probably they are on their way to become Wolf-Rayet stars. Stars with such high masses cannot live long. The He-stars must be the outcome of a star formation event that happened between 2 and 9 million years ago. With such an apparently young age, we can expect them to be dynamically unrelaxed. And indeed, most of the early-type stars within $10''$ of Sgr A* are found to lie within two counterrotating, geometrically thin disks (Genzel et al., 2003b; Paumard et al., 2006). The clockwise disk is more compact with a characteristic radius of $2'' - 4''$. Whether there exists a second, counterclockwise rotating disk is still a matter of discussion (Lu et al., 2006), but proponents describe it with a radius of $4'' - 7''$ (Genzel et al., 2003b; Paumard et al., 2006).

A specific concentration of young stars can be found within $1''$ around Sgr A*. Speckle imaging and adaptive optics spectroscopic observations showed that these so-called ‘S-stars’ are massive, blue, O/B main sequence stars (for recent work see e.g. Ghez et al., 2003b; Genzel et al., 2003b; Martins et al., 2007).

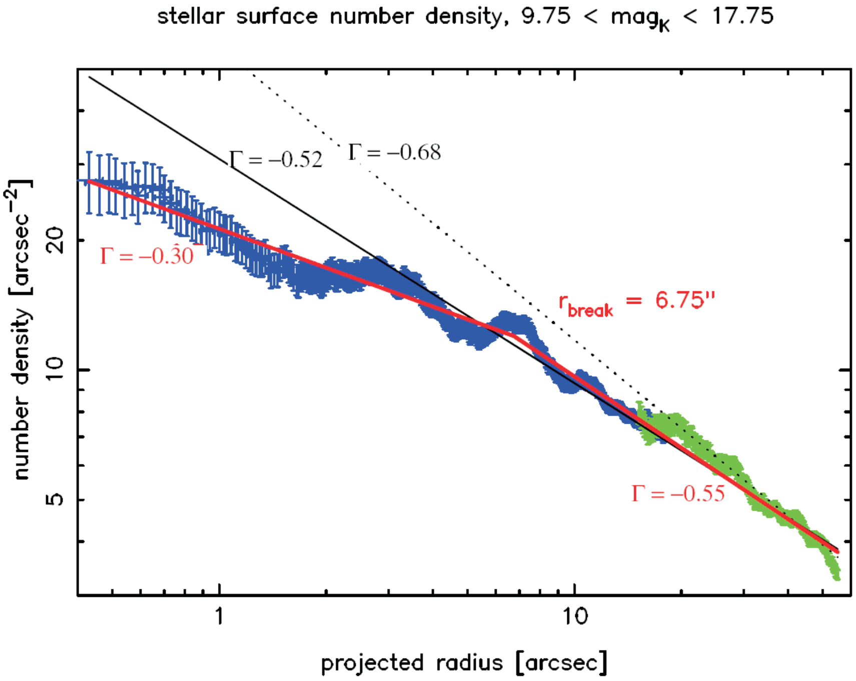

Figure 1.5: *Azimuthally averaged extinction and crowding corrected surface density vs. distance from Sgr A*. Fits to the blue data (observed with NACO) with a single (black) and with a broken (red) power-law are indicated along with the corresponding power-law indices (here, γ is the power-law index of the space density and Γ is the power-law index of the projected stellar density, the quantity that is actually observed). The green data (observed with ISAAC and scaled to the NACO data) were not used for the fits. The 1σ uncertainty of the power-law indices is 0.05 and of the break radius 0.05″ . The dotted line indicates the best-fit power-law for the green (ISAAC) data. From Schödel et al. (2007).*

The presence of young stars in the very center of the nuclear cluster severely challenges the standard theories of star formation. Morris (1993) concluded that the strong magnetic fields, large turbulent velocities, high temperatures, and strong tidal forces induced by the SMBH should prevent condensations of gas from forming protostars in the Galactic center. Formation of O/B stars at greater distances and their migration inwards via dynamical friction appears hardly feasible within the short lifetime of massive

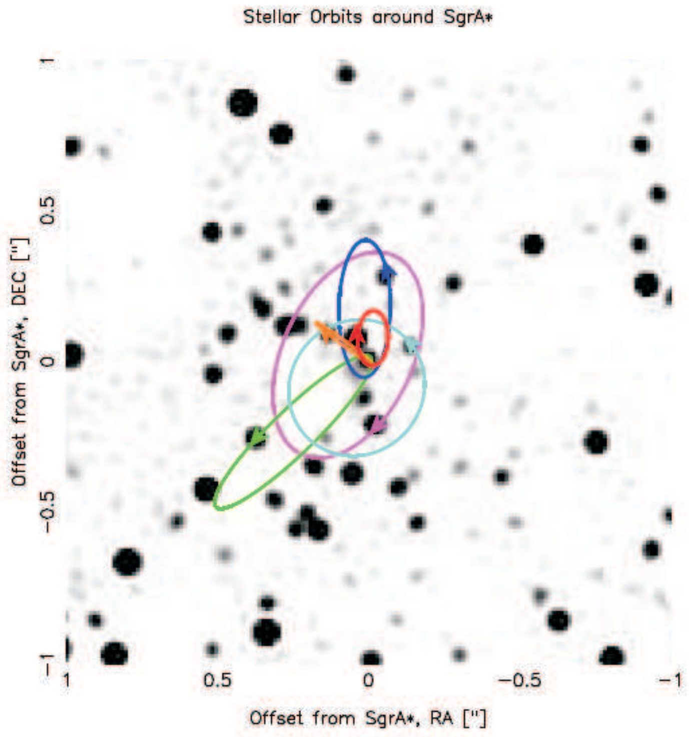

Figure 1.6: *Keplerian orbits of six S-stars as they were determined by a decade of continued observations overplotted onto a near-infrared (2.2 μm) image of the central* $1'' \times 1''$ *of the nuclear star cluster. Sgr A* sits right in the center of the image. The arrows indicate the respective stars and their direction of motion. In the Eckart & Genzel nomenclature, S2 is shown in red, S12 in blue, S1 in purple, S13 in turquoise, S14 in orange and S8 in green. From Schödel et al. (2003).*

stars. Several models have been proposed to solve the problem, e.g. stellar mergers, the infall and dissolution of a massive young cluster with an intermediate mass BH in its center, or the in situ formation of young stars within an accretion disk (see Ghez et al., 2003b; Eisenhauer et al., 2005; Paumard et al., 2006, and references therein). However, no convincing explanation could be found so far for the properties and origin of the He-stars and the O/B main sequence stars in the central cusp. Their existence is currently one of the most challenging problems in the Galactic center research.

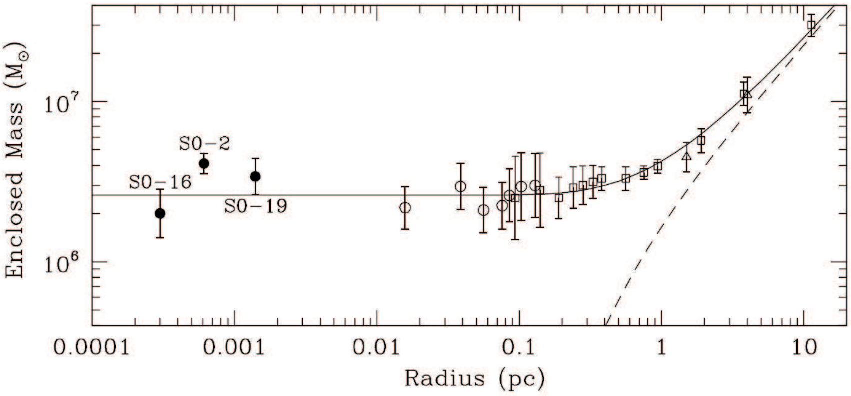

Figure 1.7: *Enclosed mass versus distance from Sgr A*. Non-filled symbols indicate the enclosed mass as determined from velocity dispersion measurements in the nuclear cluster, filled circles represent the mass determination from individual stars. S0-19 is S12, and S0-2 corresponds to S2 in the Eckart & Genzel nomenclature. The solid curve represents the best fit model which consists of BH with mass* $3.6 \pm 0.4 \cdot 10^6\ M_\odot$ *and the luminous cluster. The dashed curve is the enclosed mass due to the star cluster alone. From Ghez et al. (2003a).*

The S-stars in the central arcsecond are not only interesting because of their youth. Their motion also probes the mass distribution very close to the actual center of our Galaxy. First high proper motions of cluster stars have been reported by Eckart & Genzel (1996). The observed dependence of the velocitiy dispersion on the distance from Sgr A* is in agreement with particles on Keplerian orbits in the potential field of a point mass. Acceleration measurements by Ghez et al. (2000) allowed then to pinpoint the location of the dark mass. Since 2002 it became even possible to fit Keplerian orbits to six of the S-stars (see Schödel et al., 2002, 2003; Ghez et al., 2005a; Eisenhauer et al., 2005, and Fig. 1.6). These orbits added the so far strongest piece of evidence for the compactness of the dark mass in the GC. The inferred mass density in dependence of projected distance from Sgr A* (Fig. 1.7) excludes other explanations like a cluster of dark astrophysical objects or agglomerations of exotic particles (Schödel et al., 2002, 2003; Ghez et al., 2000, 2003a). Sgr A* is the electromagnetic manifestation of a

SMBH beyond reasonable doubt.

1.3 Sagittarius A*

1.3.1 The radio source Sgr A*: proper motion and source structure

Sgr A* is one of the brightest radio sources on the sky, and in this wavelength regime it can be monitored continuously in the sense that it never falls under the detection limit as it does in the near-infrared, where Sgr A* can only be seen in a 'flaring state'. The radio brightness of Sgr A* combined with the advent of radio interferometry allow us detailed high resolution studies of the radio emitting plasma that gets accreted by the SMBH.

At first, one might wonder what the proper motion of the radio source Sgr A* is. The stellar orbits showed that there is a concentration of dark mass in the GC and in order that Sgr A* is not a source orbiting around the dark mass, but can be identified with it, it should have zero proper motion.

Between 1995 and 1997, Reid et al. (1999) observed the GC using radio interferometry and arrived at a peculiar motion for Sgr A* of $0 \pm 15\,\mathrm{km/s}$ toward positive galactic longtitude and $15 \pm 11\,\mathrm{km/s}$ toward the north galactic pole (see also Reid & Brunthaler, 2004). Thus, both components are consistent with zero. A conservative upper limit for the proper motion in and out of the Galactic plane is $\sim 20\,\mathrm{km/s}$. As we have seen in the previous section, the S-stars move with very high velocities of $\sim 1000\,\mathrm{km/s}$. Hence, Sgr A* must be way more massive than a star. Detailed N-body simulations showed that an object with an upper limit of $\sim 20\,\mathrm{km/s}$ must be heavier than $\sim 3000\,\mathrm{M}_\odot$, otherwise gravitational Brownian motion induced by the surrounding star cluster would result in a higher proper motion. Consequently, we might identify the radio source Sgr A* with the central dark mass, i.e. the SMBH.

The technique of Very Long Baseline Interferometry (VLBI) even allows to

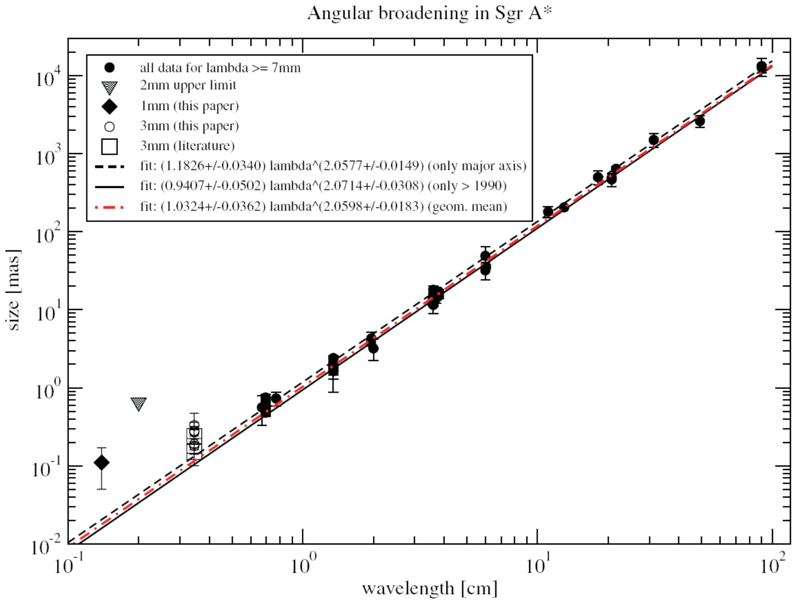

Figure 1.8: *Sgr A*'s angular size versus wavelength. Fits to the scattering law – which is assumed to be of the form $\theta_{scat} = a\lambda^{\beta}$ – are drawn with lines. See text for details. From Krichbaum et al. (2006).*

study the structure of Sgr A* itself. In this technique the signal of individual radio telescope dishes is recorded together with a time signal of an atomic clock. These data are then shipped to a common location where the correlation is done afterwards. This allows the use of baselines as long as the diameter of the earth and even longer (so-called space VLBI). Unfortunately, however, the radio image of Sgr A* was found to be broadened by interstellar scattering. For theoretical reasons a λ^2 dependence is strongly favored. And indeed, with the help of VLBI observations a dominant λ^2 variation of the angular size was observed up to 43 Ghz ($\lambda = 7\,\mathrm{mm}$), see Fig. 1.8. Observations at shorter wavelengths, though, promise the unambigous detection of the intrinsic size of Sgr A*, as the scattering size scales with λ^2, the intrinsic source most likely scales with $< \lambda^2$, and the telescope resolution behaves like λ (Bower et al., 2004). But poor telescope performance and decreased interferometric coherence make sub-mm VLBI an extremely challenging task. An additional disadvantage for observations of the GC, which is at a declination of $-29°$, is that most radio telescopes are located on the northern hemisphere.

Nevertheless, already with the data currently at hand (which go till 3.5 mm; see Fig. 1.8) an intrinsic source size can be derived. This is done via quadrature subtraction, i.e. $\theta_{\rm int} = \sqrt{\theta^2_{\rm obs} - \theta^2_{\rm scat}}$. Consequently, the exact form of the assumed scattering law ($\theta_{\rm scat} = a\lambda^{\beta}$; Fig 1.8) determines $\theta_{\rm int}$ so that the derived sizes are strongly dependent on the form and normalization of the scattering extrapolation. With the assumption that the scattering law is determined accurately at wavelengths longer than $\sim 17\,$cm, the intrinsic size at 3.5 mm of Sgr A* can be determined to $13R_S$ (Bower et al., 2006). Here, $R_S = 2\,GM/c^2$ is the Schwarzschild radius (see Chapter 4), and a BH mass of $M = 4\cdot10^6\,\mathrm{M}_{\odot}$ and a GC distance of $d = 8\,$kpc have been assumed. This extremely tight size constraint, together with the mass measurements from stellar orbits, once more confirms the BH nature of Sgr A* and also sets limits on accretion flow models, which will be discussed in the next section.

1.3.2 Sgr A*'s spectrum and accretion models

The spectrum of Sgr A* is *the* source of information when studying the accretion flow and its emission. The first thing to note is the extreme dimness of Sgr A* relative to other objects of this class. It shines roughly nine orders of magnitude below the Eddington limit. The latter is the theoretical maximum at which BHs of given mass can accrete: consider a spherically symmetric accretion flow onto a BH (a simplifying assumption as the matter will almost certainly have some angular momentum). Then the inner parts of this accretion flow will radiate and the outer parts of the flow will experience an outward driving radiative force. On the other hand, the force that drives the flow inwards is the gravitational force. Assuming that both the gravitational and the radiation source are point-like, both forces scale with r^{-2} so that a radius independent expression for the maximum luminosity – the so-called Eddington luminosity – remains.

The low luminosity of Sgr A* can in part be explained by the accretion rate, which is much lower than the possible Eddington accretion rate. The rate at which the BH is accreting can be estimated e.g. by the observations of resolved X-ray emisson of gas captured by the gravitational influence of Sgr A* (Baganoff et al., 2003). The in this way inferred rate amounts to roughly $10^{-5}\,\mathrm{M}_{\odot}\,\mathrm{yr}^{-1}$, which is four orders of magnitude below the Eddington rate (see also Section 1.3.3 for a more accurate determination of the accretion rate by measurements of the rotation measure). Still, with this accretion rate standard accretion theory would overpredict the luminosity of Sgr A* by several orders of magnitude. It seems that at these low accretion rates the 'standard model' of accretion (Shakura & Sunyaev, 1973) must be modified. The theoretical picture that emerged during the past two decades can be described by radiatively ineffiecient accretion flow (RIAF) type of models. We will briefly sketch the ideas underlying to these models, but at first we want to describe the spectral energy distribution of Sgr A* over all frequencies.

Fig. 1.9 shows the spectrum of the radio, near-infrared, and X-ray source Sgr A* (it also shines in the optical/UV range, of course, but extinction prevents us from detecting it at these frequencies). The low-frequency spectrum (below 10 GHz) slowly rises with a spectral index of $\alpha = 0.1 - 0.3$ (where the luminosity is given as $L_\nu \propto \nu^\alpha$). At higher frequencies the index increases to $\alpha = 0.5$, peaking at $\alpha = 0.7$ at $2 - 3\,\mathrm{mm}$. This feature is most often called 'submillimeter bump' although 'mm bump' might be more accurate. This mm excess is most probably due to the innermost region of the accretion flow that is self-absorbing its own synchrotron radiation, i.e. it is optically thick. The lower frequency radio emission then comes from further out, likely from a non-thermal halo surrounding the BH. The steep drop in the spectrum at sub-mm wavelengths marks the transition from optically thick to optically thin. The compact inner accretion region becomes transparent so that the synchrotron radiation can pass unhindered. This part of the spectrum can again be described with a power-law but this time with $\alpha < 0$. As will be shown in the next sections, Sgr A* is highly variable in the NIR and X-ray regime. A measurement of its 'quiescent spectrum' is therefore hardly feasible and α probably varies with flux (e.g. Gillessen et al., 2006; Hornstein et al., 2006). The variable synchrotron emisson may also radiate in the keV part of the spectrum, but it seems more likely that the relativistic electrons emitting the mm and NIR photons scatter these up to the X-ray regime via inverse Compton scattering (see Fig. 1.9).

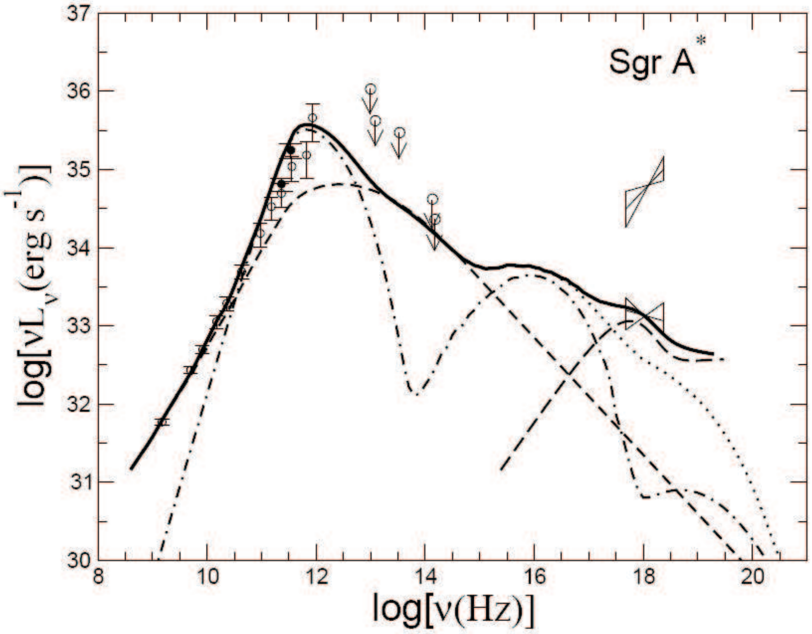

Figure 1.9: The spectrum of Sgr A together with a RIAF model from Yuan et al. (2003). The dot-dashed line shows the synchrotron and synchrotron self-Compton (SSC) emission by thermal electrons, the dashed line is the synchrotron emission by non-thermal electrons, and the dotted line is the total synchrotron and SSC emission. The solid line is the sum of all components which also includes bremsstrahlung emission shown by the long-dashed line.*

Every dynamical model of the accretion flow onto Sgr A* has to explain the enormous difference between the observed bolometric and the Eddington luminosity. As said above, a radiative inefficient accretion flow in which radiation is suppressed can explain the observed spectrum. Narayan & Yi (1994) proposed a two temperature accretion flow where the radiating electrons are decoupled from the non-radiating ions. The latter carry the potential energy and are advected beyond the BH event horizon. This type of flow is therefore also known as advection dominated (ADAF). During the recent years it was realized that many variants of RIAFs provide a reasonable match to the spectral energy distribution (e.g. Blandford & Begelman, 1999). As an expansion of the original ADAF, Yuan et al. (2003) introduced a substantial outflow, increased the turbulent heating, and added non-thermal particles (this model was used for Fig. 1.9). Based on energy arguments it is now clear that some kind of outflow must be present (e.g. Loeb & Waxman, 2007), however its nature is still unknown. The non-thermal expanding halo mentioned above may as well be a jet (see Markoff et al., 2001, 2007, and references therein). The size constraints noted in the last section are in agreement with the jet model. The jet can basically be hidden behind the scattering screen (Markoff et al., 2007). Whether Sgr A* really has a short jet or just some non-collimated outflow is still an open question.

1.3.3 Polarization

Polarimetric information, i.e. the degree of linear and circular polarization and the position angle of the electric field vector, greatly enhances the knowledge about the source under consideration. In this thesis, we present near-infrared polarimetry of Sgr A* and use this information to model the observed radiation outbursts. Therefore, the discussion of NIR polarization will be postponed to the subsequent chapters. In this section, we will summarize the polarization of Sgr A* at longer wavelengths.

Between 1.4 and 112 GHz the emission of Sgr A* shows no linear polarization with upper limits of 0.1% – 2% (e.g. Bower et al., 2001). The absence of linear polarization at these frequencies is very likely intrinsic to the source and not due to Faraday depolarization. The latter effect arises in an ionized, magnetized medium, where electromagnetic waves with positive and negative helicity have different indices of refraction. At frequencies of 150 – 400 GHz, however, Sgr A* shows a degree of linear polarization of up to 10% (Aitken et al., 2000; Bower et al., 2003). From the lack of linear polarization at longer wavelengths, it is natural to conclude that these large measured values at higher frequencies must arise in a somewhat separate component. This strengthens the picture inferred from the spectral energy distribution that the cm radiation arises in a halo around Sgr A*, and the mm/sub-mm to NIR flux stems from a compact, Keplerian emission source that is orbiting within a few Schwarzschildradii of the SMBH (see also the discussion at the beginning of Chapter 5).

Recently, very sensitive and well calibrated measurements of the polarization of Sgr A* at 230 and 345 GHz have been carried out by Marrone et al. (2006a, 2007) using the Submillimeter Array (SMA) and its new polarimeter. For the first time they have been able to show that the polarization varies on hour timescales, as has been observed for the total intensity (see next section). In one night they also found signatures of a polarized blob orbiting the BH (Marrone et al., 2006b), a model that lies at the heart of this thesis (see Chapter 5). Furthermore, they used their observations for the first statistically significant determination of the rotation measure, a measure that describes the change in positon angle of a linearly polarized signal due to Faraday rotation. With this rotation measure the accretion rate at small radii can be estimated to be in the range $2 \cdot 10^{-7} \mathrm{M}_{\odot}\,\mathrm{yr}^{-1}$ to $2 \cdot 10^{-9} \mathrm{M}_{\odot}\,\mathrm{yr}^{-1}$, if the magnetic field is near equipartition and ordered. Finally, the mean intrinsic polarization angle at these frequencies seems to be $167^\circ \pm 7^\circ$ (E of N) with variations of $\sim 30^\circ$.

1.3.4 Flares

Repeated observations of Sgr A* over more than thirty years have shown it to be variable at all frequencies. The by far most dramatic changes in flux can be observed in the X-rays and the NIR regime. Baganoff et al. (2001) reported the first detection of an X-ray flare from the Galactic center BH. During that flare, the X-ray output changed abruptly by a factor of five in less than ten minutes. This type of variability is rarely seen in the emission from a SMBH. Using simple light crossing arguments, the variability on these short timescales points to an emission region with a size of only a few Schwarzschild radii.

The first NIR flare – and therefore also the first emission at these wavelengths at all – was reported by Genzel et al. (2003a, see also Fig. 1.10 for NIR images of Sgr A*). This flare will be discussed extensively in Chapter 3 as it not only shows very short rise and fall timescales like in the X-rays, but also a suggestive quasi-periodic sub-structure might be superimposed on the flare. This quasi-periodicity (QPO) is also indicated in other flares and needs further confirmation and interpretation. These are the main goals of this thesis, and we therefore refer to the subsequent chapters for longer

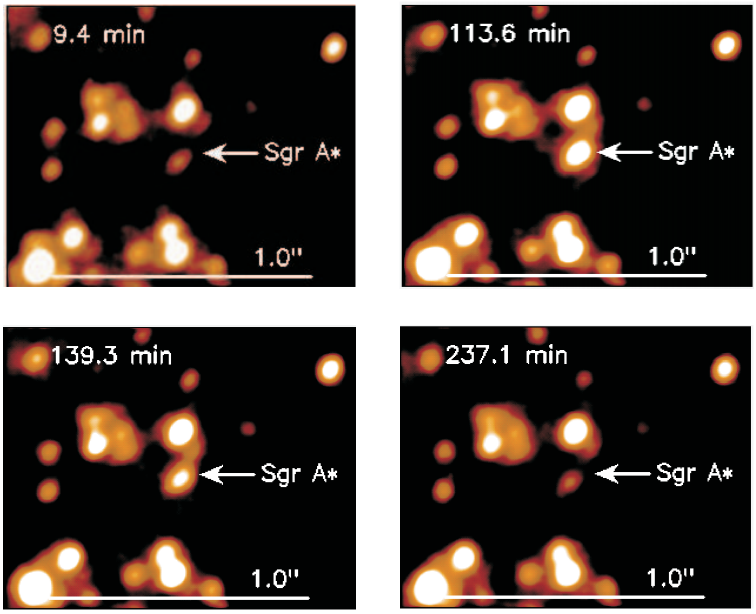

Figure 1.10: *Typical NIR flare data. In these deconvolved and beam restored (see Chapter 2) NACO images at 2.2 μm the time after the start of the observations is shown in the upper left corner. At first, only a stellar source close to Sgr A* can be seen. Sgr A* then starts flaring and can clearly be detected. After some time it is again 'off', i.e. under the detection limit. The data are from our 2007 observing run.*

discussions of NIR flares from Sgr A*. Here we just want to note that the flare activity can be described by a power-law. This description of the flare activity as a power-law under the assumption of a characteristic flare time implies that the 'NIR quiescent phase' of Sgr A* can be regarded as a sequence of frequent low amplitude flares. Such models have been shown by Eckart et al. (2004) and have been described in detail in Eckart et al. (2006a). The observed flares may be the consequence of a clumpy or turbulent accretion flow and the flare power spectrum may be coupled to the power spectrum of accreted clumps or turbulences.

An ideal tool to further constrain the emission mechanisms responsible for the radiation from the immediate vicinity of the central Black Hole are simultaneous observations of Sgr A* from the radio to the X-ray regime. The first successful experiment during which simultaneous X-ray and near-infrared flare emission has been detected was presented by Eckart et al. (2004). They detected a weak $6 \cdot 10^{33}$ erg/s X-ray flare and covered its decaying flank in the NIR. The flux density variability of Sgr A* at radio through sub-mm wavelengths has been studied extensively, showing that variations occur on timescales from hours to years (e.g. Zhao et al., 2003; Herrnstein et al., 2004). Some of the radio variability, however, is probably due to interstellar scintillation. So far the connection to variability at X-ray wavelengths has not been clearly elucidated. Zhao et al. (2004) showed that there is a probable link between the brightest X-ray flare ever observed and the flux density at mm- and short cm-wavelengths (see also Mauerhan et al., 2005).

New simultaneous NIR/sub-mm/X-ray observations of the Sgr A* counterpart were recently presented by Eckart et al. (2006a). The authors investigate the physical processes that may be responsible for the variable emission from Sgr A*. The observations were carried out using the NACO adaptive optics (AO) instrument at the European Southern Observatory's Very Large Telescope (see Chapter 2) and the ACIS-I instrument aboard the Chandra X-ray Observatory as well as the Submillimeter Array on Mauna Kea, Hawaii, and the Very Large Array in New Mexico. Eckart et al. (2006a) detected one moderately bright flare event in the X-ray domain and five events at infrared wavelengths. At 2 - 8 keV the X-ray flare had an excess luminosity of about $33 \cdot 10^{33}$ erg/s. For its entire duration the flare was covered in the X-ray domain and was detected as a simultaneous NIR event with no time lag larger than an upper limit of ≤ 10 minutes – which is mainly given by the required binning width of the X-ray data. This time lag between the NIR and X-ray flare emission is in agreement with a synchronous evolution (see Fig. 1.11). This is indicated by all flares covered simultaneously in 2003 and 2004. Cross-correlation shows that the time lag between the flares at different wavelengths is less than 10 minutes and therefore consistent with zero.

The flaring state can be explained with a synchrotron self-Compton (SSC) model involving up-scattered sub-millimeter photons from a compact source component. Inverse Compton scattering of the THz-peaked flare spectrum by the relativistic electrons then accounts for the X-ray emission. This model allows for NIR flux density contributions from both the synchrotron

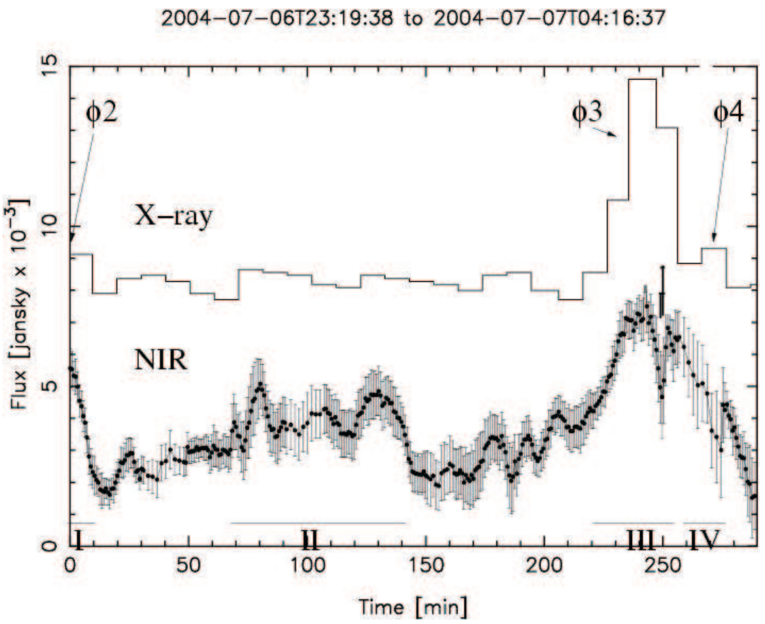

Figure 1.11: *The X-ray and NIR light curves of the 2004 observations plotted with a common time axis. Individual flaring events are numbered. The synchronous evolution of both wavelengths is self-evident. From Eckart et al. (2006a).*

and SSC mechanisms. Indications for an exponential cutoff of the NIR/MIR synchrotron spectrum allow for a straightforward explanation of the variable and red spectral indices of NIR flares (e.g. Gillessen et al., 2006). We can assume that the X-ray flares are predominantly produced by SSC emission rather than synchrotron emission. As a consequence – and in good agreement with the observations – the total number of detected X-ray flares is smaller than that in the NIR.

There was no extensive overlap between radio and the NIR/X-ray measurements in 2004 resulting in no simultaneous flare detections between the NIR/X-ray data and the VLA and SMA data. However, the excess flux densities detected in the radio and sub-mm domain may indeed be linked with the flare activity observed at shorter wavelengths. The radio and sub-mm data show clear indications for variability that appear to occur on somewhat longer timescales than the X-ray and IR variations. The exact relation between the radio/sub-mm domain and the NIR/X-ray domain still remains uncertain due to the lack of sufficient simultaneous coverage. However, the amplitudes and timescales indicated are consistent with a model in which the emitting material is expanding and cooling adiabatically (see also Yusef-Zadeh et al., 2006).

1.4 This thesis

The goal of this thesis is at least twofold. Firstly, we give strong evidence that the suggestive quasi-periodicity in some NIR flares really does exist in the sense that its observation can be repeated and that it is a truely periodic feature instead of frequency dependent, i.e. colored, noise. Secondly, we adopt a simple model to explain this periodicity and by taking all relativistic effects into account, we fit the observed polarimetric lightcurves. This gives constraints on the inclination of the Sgr A* system, its angular momentum, and its position angle on the sky.

In the next chapter we first give an overview about the standard data reduction techniques used throughout the thesis. The following chapter then discusses the significance of the quasi-periodic oscillation (QPO) seen in some NIR flares. A statistical analysis of old data as well as brand new polarimetric data which strongly support the existence of an QPO are presented. In Chapter 4 we introduce some basic concepts of General Relativity. The Kerr metric that describes the spacetime around a spinning BH is presented and the technique and code with which the ray tracing computations have been carried out are explained. Chapter 5 applies the ray tracing code to the model of an orbiting plasma blob around Sgr A* to explain the QPO and fit the recent polarimetric light curves. Chapter 6 evaluates the model fits to constrain the three dimensional orientation of the Sgr A* system, while Chapter 7, finally, concludes this work and gives an outlook on future projects in GC research.

Chapter 2

Observations and data reduction

This thesis is partially based on GC near-infrared (NIR) data taken in 2005 and 2006 with NACO at ESO's Very Large Telescope (VLT). This chapter presents some basic concepts for NIR observations, i.e. the principle of adaptive optics is explained and the VLT in general and the instrument NAOS/CONICA (NACO) in particular are introduced. After this, the standard data reduction techniques in the NIR domain including deconvolution are described. These techniques have been applied to the data that are shown and interpreted in the following chapters. For more details concerning observational techniques in GC research, the reader is referred to Eckart et al. (2005).

2.1 Near-infrared observations of the Galactic center

As we have seen in the previous chapter, the NIR regime plays an outstanding role in GC research. This is especially true since the advent of adaptive optics (AO). AO is a means to overcome the phenomenon called

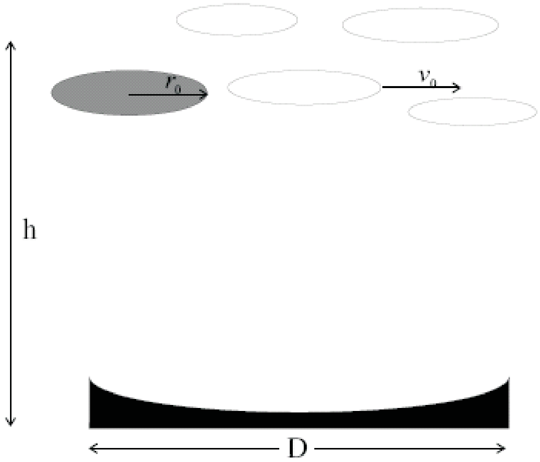

Figure 2.1: *Sketch of a single turbulent layer at height h in the atmosphere consisting of seeing cells with diameter r_0 and velocity v_0 over a telescope aperture with diameter D. From Ott (2002).*

seeing, the blurring of starlight due to the earth's atmosphere. In ideal conditions where nothing disturbs the light propagation from the source to the telescope the angular resolution R that can be achieved is given by

$$R \sim \frac{\lambda}{D},$$

where λ is the observing wavelength and D is the diameter of the telescope. Images in which such a resolution is given are called diffraction limited. However, diffraction limited operation of a single telescope is only possible if the telescope is either in space or the theoretical angular resolution is greater than the air turbulences which are therefore negligible. The latter case typically applies if the observing wavelength is greater than $\sim$ 10 micrometers or the telescope aperture is less than $\sim$ 40 cm (in the NIR) so that R is greater than one arcsecond – the characteristic scale to which point sources are blurred.

A simple model for the atmosphere's turbulences is depicted in Fig. 2.1. So-called seeing cells with a typical diameter r_0, the Fried diameter (Fried, 1966), distort planar wavefronts of an extraterrestrial source. These cells move with a velocity v_0 so that the point spread function[1] (PSF) is also

---

time variable. The spatial variability of the PSF is due to the finite size of the seeing cells. The region over which the PSF is roughly constant is called the isoplanatic patch. With values of r_0 of the order $\sim 40\,\mathrm{cm}$ in the NIR and heights of the (single) turbulent layer of $\sim 10\,\mathrm{km}$ the isoplanatic angle is $\sim 10''$.

The notion of a single turbulent layer consisting of individual seeing cells is over-simplistic mainly because several turbulent layers are responsible for the distortion of the incoming light. However, this picture is extremely helpful in understanding AO imaging[2] where real time corrections of a deformable mirror approximately restores the flatness of the wavefront.

The simplest form of AO is tip-tilt correction which corresponds to the correction of the image motion. This is done by using a rapid moving tip-tilt mirror that makes small rotations around two of its axes. In a more advanced AO system, several mirror segments (which make up the deformable mirror) can tip and tilt independently, thereby correcting for phase errors of an incoming wavefront that are of the order of a few micrometers. These corrections have to work on timescales of $\sim 100\,\mathrm{Hertz}$.

It can be shown (Fried, 1966) that the angular diameter of a seeing cloud defined as

$$\omega \approx \frac{\lambda}{r_0}$$

has the following dependency on the observing wavelength λ:

$$\omega \sim \lambda^{-1/5}.$$

A direct consequence of this is that seeing in the NIR is better than e.g. in the optical, where a typical angular diameter of a blurring cloud is $\sim 1''$ as opposed to $\sim 0.7''$ in the NIR. This implies that the requirements on an AO system, i.e. the computational power, are much higher in the optical. This is why current AO technology is only capable of correcting images at wavelengths longward of one micrometer.

---

[1] The point spread function describes the response of an imaging system to a point source.

[2] Adaptive optics should not be confused with active optics which works on a much longer timescale and has the purpose to correct the geometry of the primary mirror.

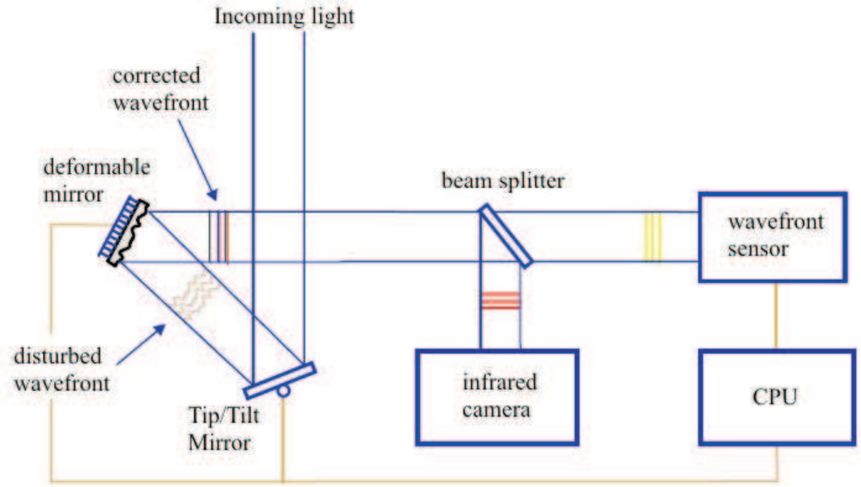

Figure 2.2: *Schematic view of a typical AO system. See text for a detailed description. Adopted from Ott (2002).*

Fig. 2.2 sketches an AO loop. The incoming wavefront gets corrected for the overall image motion at the tip-tilt mirror, is reflected at the deformable mirror and sent to a beam splitter. This is a dichroic mirror that separates the optical train into the imaging path and the wavefront sensing path. The wavefront sensor signal is used by a closed loop control computer to drive the tip-tilt and deformable mirror. This leads then to a flat, almost undisturbed wavefront that produces an image at the diffraction limit of the telescope. The control loop needs to be run by a very fast computer. Within only one millisecond or even less the system uses the wavefront sensor measurements to calculate the commands for the actuators that adjust the deformable mirror accordingly.

Two types of wavefront sensors are mainly used: Shack-Hartmann and curvature wavefront sensors. The latter uses the difference of pairs of extra-focal images to measure the second derivative, i.e. the curvature, of the wavefront. A Shack-Hartmann sensor divides the wavefront into multiple sub-apertures so that several images of a point light source occur on the detector. The displacement of the image in each of these sub-apertures allows to determine the first derivative, i.e. the slope, of the wavefront. With both methods, wavefront sensing is done on a guide star that needs to be sufficiently bright and compact. The measurement is usually done on an optical guide star, even in the infrared domain. This leads to a sky coverage of just a few percent, as there is often only an infrared nearby bright enough point source around. This is why the NAOS AO system at the VLT is also equipped with an infrared wavefront sensor so that the AO loop can be locked on an infrared guide star. In the case of the Galactic center, the supergiant IRS 7 (e.g. Schödel et al., 2003) located 5.5$''$ north of Sgr A* is the ideal source for wavefront sensing. An even better way to circumvent the problem of needing a nearby guide star is to create an artificial one with the help of a laser. This technology uses e.g. a Sodium-laser to excite Sodium in the mesosphere so that a bright compact light source emerges. A laser guide star AO system is already working on the Keck II telescope and has been used for GC observations (Ghez et al., 2005b).

For the observations presented in this thesis we used the Very Large Telescope which is located on Cerro Paranal, 120 km south of Antofagasta, Chile. It is operated by the European Southern Observatory. The choice of a telescope is not a matter of taste. As Sgr A* is very dim in the NIR and embedded in a dense stellar cluster (see Chapter 1), high angular resolution and sensitivity is required. So far, only the VLT and the Keck telescopes – which are only accessible to the University of California and the California Institute of Technology – have been used for high end research on Sgr A*. As the GC is at a declination of $-29°$, a major advantage of the VLT is that it is located on the southern hemisphere.

The VLT is composed of four separate telescopes, each of which has a 8.2 meter mirror, see Fig. 2.3. They can combine their light to make an interferometer (VLTI), but here we are only interested in the properties of a single telescope. The main mirror of each telescope is supported by an active optics system that corrects the geometry of the system approximately once a minute (Fig. 2.4). The instrument NACO is installed in the Nasmyth focus of Unit Telescope four, also called Yepun[3].

NACO is short for NAOS (Nasmyth adaptive optics system)/CONICA

---

[3] The four telescopes are named in the language of the Mapuche people. They are: Antu (sun), Kueyen (moon), Melipal (Southern Cross) and Yepun (Venus).

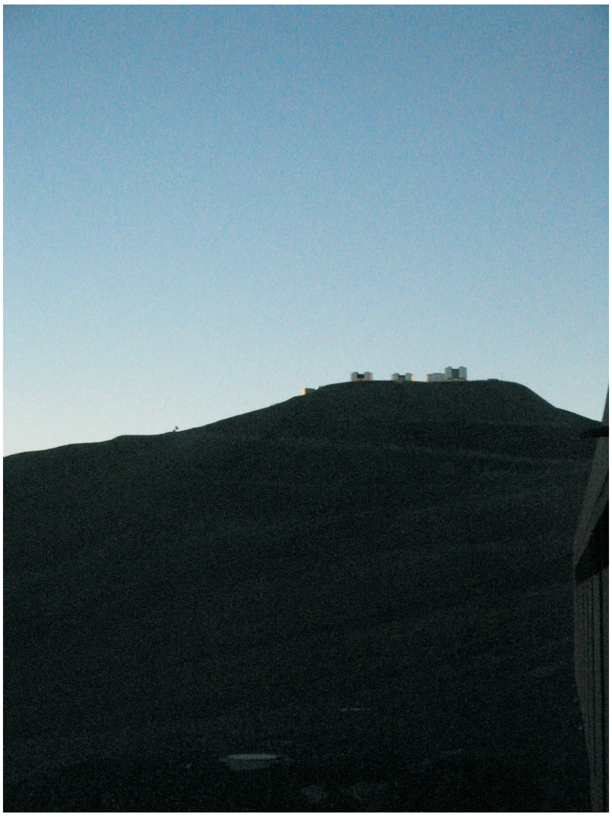

Figure 2.3: *The four domes of the VLT as seen from the base station. The picture was taken during our 2006 observing run.*

(Coude near infrared camera) and is the combined AO system and science camera (e.g. Brandner et al., 2002). NAOS works in principle as shown in Fig. 2.2 and explained before. It offers five different dichroic beam splitters to adopt to the flux and the spectral characteristics of the guide star. It has two wavefront sensors, one for the optical and one for the near-infrared regime so that either a visible or infrared guide star can be chosen. An important feature of CONICA, at least for this thesis, is that it is equipped with a polarimeter. It consists of a birefringent Wollaston prism that separates randomly polarized or unpolarized light into two orthogonal, linearly polarized outgoing beams. This allows the simultaneous measurement of two independent directions of the electric field vector. To rapidly switch to different angles, this system is combined with a half-wave retarder plate that can be rotated quickly. This is crucial in determing the polarization

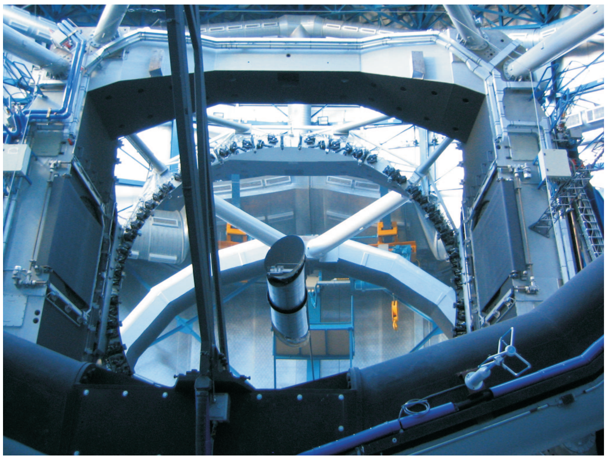

Figure 2.4: *The main mirror on one of the four telescopes. It has a diameter of 8.2 meter. Also the Nasmyth mirror that directs the light to one of the foci can be seen.*

characteristics of a fast time varying source.

2.2 Standard data reduction

The image that is read out of NACO is full of instrumental signatures, i.e. not only the flux of the astronomical source but also the thermal radiation of the telescope (mirrors and mounting) and the atmosphere, the read out noise, the dark current and a non-linear response function of the detector are observed. This is mathematically:

$$I = (S + I_{th}) \cdot F + I_d + N, \tag{2.1}$$

where I is the observed image, S is the science source under consideration, I_{th} is thermal flux from the surroundings, F is the relative response function (the flat field of the detector), I_d is the dark current and N is the read out noise.

The response function of the detector can be determined if it is irradiated homogeneously. To do that one normally uses the twilight sky or a lamp with intensity L. Then $L \cdot F + I_d + N$ is measured. To get rid of the dark current, an image with the aperture closed is needed. This is then subtracted from the twilight or lamp exposure and normalized to one, so that the relative response function (the flat field) is given by

$$F = ||\text{bright} - \text{dark}||,$$

where bright is the homogeneously irradiated image and $|| \cdot ||$ means normalized. Here and in the following we also neglect a noise term.

As a next step we have to deal with the thermal radiation of the earth's atmosphere and the telescope itself. To subtract this part out of our observed image, we obviously have to observe it, i.e. make an exposure of the night sky without any apparent sources. In the case of the Galactic center the closest part of the night sky where there are (almost) no infrared sources is located $713''$ west and $400''$ north of IRS 7. As the thermal radiation is time variable, this exposure must be repeated several times during an observation whereas the amount of sky exposures depends on the exact observing wavelength under consideration. In such an image we observe $sky = I_{th} \cdot F + I_d$. Now we can solve equation (2.1) for the source we are interested in

$$S = \frac{I - sky}{F}. \tag{2.2}$$

What remains to do is a correction for dead/hot pixels, i.e. pixels which have a response function of zero or of a way too high value (relative to the immediate neighbors), respectively. Those pixels should be replaced by an interpolated value.

The resulting image after the above described standard data reduction will still suffer a certain degradation. The finite size of the telescope will cut off parts of the wavefront. This is why a point source observed with a circular aperture results in the familiar Airy pattern, at least when there is no aberration, atmosphere etc. In reality, the PSF will deviate from this ideal case. It will also vary over the detector and in time, as discussed above.

An observed signal S can be described as the deconvolution of the observed object $\mathcal{S}$ with the PSF

$$S = \mathcal{S} * \text{PSF},$$

where $*$ is the convolution operator and we have neglected an additive noise term for simplicity. If the PSF is known, it is in principle possible to cancel it out of the equation and replace it by a Gaussian that has a full width at half maximum (FWHM) comparable to the diffraction limit of the used telescope.

The PSF is a priori not known, of course. However, it can be estimated in an astronomical image, as stars are effectively point sources. An isolated, bright star should be used for the extraction of a PSF. As the GC is a very crowded field, several bright and possibly isolated stars may be used so that the median image of these stars is a good PSF estimator. In this work, the software package *StarFinder* (Diolaiti et al., 2000) was used for PSF extraction. In this program the user has to choose individual stars from which the PSF is then basically extracted in the way described above. The only thing one has to keep in mind is that the PSF varies across the field so that nearby stars have to be chosen and the applicability of this PSF is limited to a certain part of the image only.

With an (estimated) PSF at hand, we can go a step further and deconvolve our image. Many deconvolution algorithms exist, but here we just want to briefly describe the one we actually used in this thesis. For a comparison study of different deconvolution methods, the reader is referred to Eckart et al. (2005). We have chosen the most suitable one for our purposes. It is called Lucy-Richardson deconvolution and goes back to Lucy (1974). It is an iterative scheme. In the first step, the current estimate of the true image $\tilde{\mathcal{S}}$ is convolved with the PSF

$$\Gamma_n = \tilde{\mathcal{S}}_n * \mathrm{PSF}.$$

This is then compared to the observed image S

$$R = \frac{S}{\Gamma_n} * \mathrm{PSF}.$$

Here again a convolution is carried out, but this is only to serve as a low-pass filter that reduces the influence of noisy high frequencies. As the last step, the current image estimate is multiplied with the correction function

$$\tilde{\mathcal{S}}_{n+1} = R \cdot \tilde{\mathcal{S}}_n.$$

Fig. 2.5 compares a non-deconvolved to a convolved image. As can be seen, the disadvantages of the Lucy-Richardson algorithm are a tendency to resolve diffuse background into distinct sources and a sucking up of faint sources by brighter ones, which leads to the dark areas around the brightest stars. The described deconvolution algorithm has been implemented in the software package DPUSER, which has been used throughout this thesis, by Ott (2002).

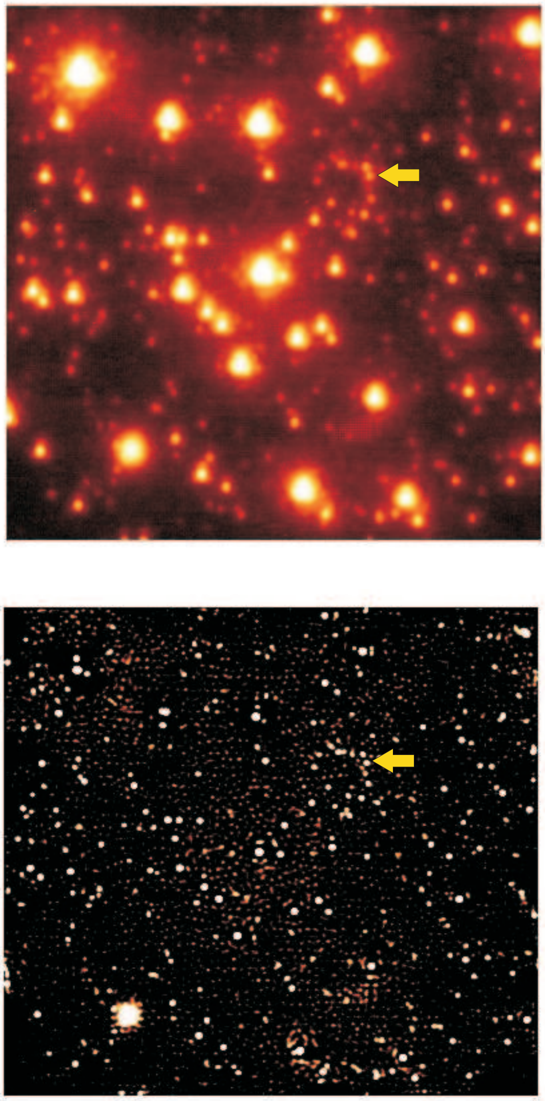

Figure 2.5: *Top: Reduced but non-deconvolved image of the Galactic center at* $\lambda = 2.2\,\mu m$. *Sgr A* is marked with an arrow. It is in a flaring state so it can be seen in this image. Bottom: The same image as above but this time deconvolved with the Lucy-Richardson algorithm. It was convolved afterwards with a Gaussian beam with a FWHM of* ~ 60 *milliarcseconds which corresponds to the diffraction limit.*

Chapter 3

Quasi-periodicities in near-infrared flares from Sgr A*

In this chapter we give strong support for the existence of a quasi-periodic sub-structure in some NIR flares of Sgr A*. We first carry out a statistical analysis of a flare observed in 2003 and then present recent polarimetric measurements which clearly show sub-flares at a seperation of $\sim$ 20 minutes. Parts of this chapter have been published in Meyer et al. (2006a,b) and Eckart et al. (2006b).

3.1 A QPO in the 2003 lightcurve from Sgr A*?

In a few NIR and X-Ray flares a suggestive quasi-periodicity of roughly $\sim$ 20 minutes has been reported (Genzel et al., 2003a; Eckart et al., 2006b; Aschenbach et al., 2004; Belanger et al., 2006). It manifests itself in the lightcurve as sub-flares superimposed on the underlying main flare (see Figure 3.1). It is not clear yet, how these quasi-periodicities (QPOs) are created. The timescale of the lightcurve variations and the rather small volume around Sgr A*, where these variations originate, indicate that rapid motion in strong gravity is involved. High-frequency QPOs in microquasars scale with the inverse mass of the BH, and the frequency of the suggestive QPO in Sgr A* indicates that an extrapolation from the stellar-mass BH case in microquasars to the MBH case is applicable (Abramowicz et al., 2004; McClintock et al., 2004, and references therein).

The timescale of $\sim$ 20 minutes is comparable to the orbital timescale T near the innermost stable circular orbit (ISCO) of a spinning MBH (see eq. (4.11) or Bardeen et al., 1972). This can be written as

$$T \doteq 110 \left(r^{3/2} + a_{\star}\right) \frac{M}{3.6 \cdot 10^{6} M_{\odot}} \text{ [sec]}, \tag{3.1}$$

where $a_{\star}$ is the BH dimensionless spin parameter ($-1 \leq a_{\star} \leq 1$), and r is a circumferential radius within the equatorial plane given in units of the gravitational radius $r_g \equiv GM/c^2$. Therefore it appears reasonable that corresponding frequencies are present in the flare lightcurves. In this context, we would like to point out the rapid variability in the lightcurve of the NIR flare of 16 June 2003 shown in Fig. 3.1 (originally reported by Genzel et al., 2003a). Variations greater than 5σ can be seen on timescales of a few minutes, inferring an upper limit of the size of the source of less than 10 Schwarzschild radii if assuming that the cause responsible for the flare propagates at the speed of light. It can be expected, however, that the actual signal in the source propagates with a speed comparable to the sound speed or to the Alfvén speed, i.e. a few orders of magnitude slower than c. Therefore it appears again reasonable to assume orbital motion of a compact source as the cause of the rapid variability.

Furthermore, global MHD simulations show that the inner accretion flow is very inhomogenous and nonuniform, so that local overdensities build up (Machida & Matsumoto, 2003; De Villiers et al., 2003). Modeling these overdensities as hot spots orbiting around the BH gives lightcurves very similar to the observed ones (Broderick & Loeb, 2005, 2006; Eckart et al., 2006b). Recent polarimetric measurements showed that the sub-flares have a degree of linear polarization of up to $\sim$ 20% and that they come along with a swing in the polarization angle (Eckart et al., 2006b). The new information provided by the polarization state is extremely useful because it breaks the degeneracy of various model parameters. In this thesis we demonstrate that the available data are consistent with an orbiting spot model and that they offer a new avenue to constrain BH parameters in the future.

A serious limitation for the possible detection of quasi-periodicities in NIR flares are observational constraints. Several factors must coincide: (i) the occurrence of a flare; (ii) the flare must be fairly bright and last long enough in order to be able to sample a sufficient number of oscillations; (iii) atmospheric conditions must be good (seeing $\lesssim 0.8''$ and $\tau_0 \gtrsim 3\,\mathrm{ms}$ at NACO/VLT) and – above all – stable during the entire observation, i.e. several hours. We estimate from our observational experience that these conditions are fulfilled only 10-20% of the total time dedicated to observations with NACO at the VLT. An additional problem is caused by gaps in the observational sequence that may be introduced into the time series due to the necessity of sky background measurements in NIR observations. Due to the extremely crowded field of the stellar cluster in the GC, the background cannot be extracted from the on-source observations. Also it is not clear whether each flare would be accompanied by a QPO. A new window into QPOs may have been opened by the discovery of Eckart et al. (2006b), who found that possible periodic variations can be observed in polarized light while not being detectable in the overall flux.

In the context of QPOs, it is also important to refer to the debate concerning the existence of QPOs in AGN. In many cases X-ray light curves of these objects appear to be characterised by red noise, which may lead to an overestimation of the significance of periodic signals in the light curves (see e.g. Vaughan, 2005; Timmer & König, 1995; Benlloch et al., 2001).

In this section we re-analyse the so far best case for NIR quasi-periodicity in Sgr A*, that is the K-band flare from 16 June 2003 which was originally reported by Genzel et al. (2003a). Contrary to the other two mentioned flares, it has the advantage that apparent QPOs could be followed over 7 cycles. The imaging data were observed with the AO system/infrared camera NACO at the ESO VLT. The detector integration time was 10 s. Several images were averaged before saving the data. The effective time resolution is about one image every 40 s. We reduced the data in a standard way (sky subtraction, bad pixel correction, flat fielding, see Chapter 2). Applying a sliding window, the median of 5 images at a time was constructed.

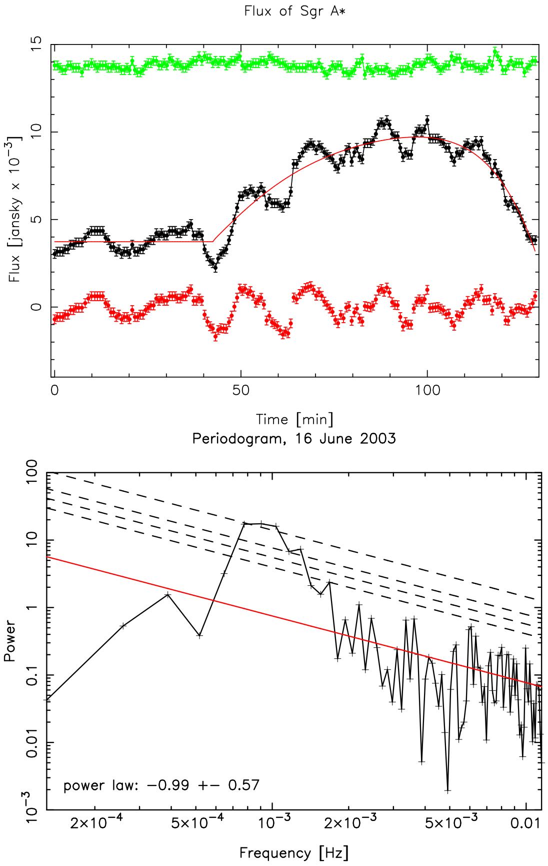

Figure 3.1: *Sgr A* NIR flare from 16 June 2003. Upper panel: Light curve of Sgr A* in black. A polynome fit to the overall flare and the residuals after subtracting this fit are shown in red. The light curve of a constant star, S1, is shown in green. Lower panel: Periodogram of the Sgr A* flare after subtraction of the overall flare, i.e. corresponding to the lower, red curve in the upper panel. The straight red line shows a de-biased power law fit to the data points when considering all frequencies greater than* 2×10^{-3} *Hz. The dashed lines give the 1-, 2-, 3- and* 5σ *confidence bands derived with the method of Vaughan (2005).*

From these images, the PSF was extracted via point-source fitting with the program *StarFinder* (Diolaiti et al., 2000). Subsequently, the images were deconvolved with a Lucy-Richard deconvolution and beam restored with a Gaussian beam. The flux of Sgr A* and of stellar sources in the field was extracted via aperture photometry with a sufficiently large aperture to contain the entire flux of the objects. Photometry calibration was done relative to several stars in the field with a known flux. The resulting extinction corrected light curve (assuming $A_K = 2.8$ mag) is shown in the upper panel of Fig. 3.1. The black curve shows the flux of Sgr A* and the upper, green curve the flux of S1, a star at $\sim 0.4''$ distance from Sgr A*. Its lightcurve is assumed to be constant. The lower, red curve shows the light curve of Sgr A* after subtracting a constant (0-40 min) plus a 5th-order polynomial fit (40-130 min) to the overall flare.

The lower panel of Fig. 3.1 shows a non-oversampled Lomb-Scargle periodogram of the Sgr A* flux after subtraction of the overall flare. There is a broad peak visible around 2×10^{-3} Hz that corresponds to the $16 - 21$ min variability that can be seen in the lightcurve. In order to examine the significance of this peak, we followed the recipe of Vaughan (2005). The assumed underlying power law is indicated by the straight red line in the lower panel of Fig. 3.1. This power law with an index of -0.99, i.e. a classical red noise, was found by fitting all data points in the frequency range $\geq 2 \times 10^{-3}$ Hz. The prescription of Vaughan (2005) takes the bias into account that originates when fitting the logarithm of the periodogram. Dashed lines in the plot of the periodogram indicate the 1-, 2-, 3- and 5σ confidence bands which can be calculated analytically. We also used Monte Carlo simulations to derive these confidence limits which lead to the same result.

It can be seen that the peak around 10^{-3} Hz reaches the 5σ threshold. Even after correcting for the model uncertainty, as it is suggested in Vaughan (2005), the significance is still at the 4.2σ level.

The critical point in this procedure is the choice of the slope of the power spectrum. We followed the prescription of Vaughan (2005). We think our approach is justified because the periodogram shows a clear component of red noise (see also discussion in Belanger et al., 2006).

We conclude that, on the one hand, there are strong indications for a quasi-periodicity in the NIR flare from 16 June 2003. On the other hand, this single flare by itself is not enough to present ironclad evidence. However, more events were reported that support the presence of a periodicity in the considered time range: the second K-band flare reported by Genzel et al. (2003a) and the flares observed in polarimetry which will be described in the next section.

3.2 Polarimetric measurements of Sgr A*

3.2.1 The observations from 2006

Using the NIR camera CONICA and the adaptive optics (AO) module NAOS on ESO's Very Large Telescope UT4 on Paranal in Chile, we observed Sgr A* in the K_S-band during the night between 31 May and 1 June 2006. To achieve good time resolution, a Wollaston prism was combined with a half-wave retarder plate. This allows the simultaneous measurement of two orthogonal directions of the electric field vector and a rapid change between different angles. The detector integration time was 30 s. Including the overheads due to the need to turn the half-wave plate and telescope offsets, individual frames could be taken every 70–80 s.

During the observation, the optical seeing ranged between $0.6''$ and $1''$ and the AO correction was stable. Sky measurements were taken by observing a dark cloud a few arc-minutes to the north-west of Sgr A*. To minimize the effects of dead pixels, the observations were dithered. The data were reduced in a standard way, i.e. sky subtracted, flat-fielded, and corrected for bad pixels. For every individual image, the point spread function (PSF) was extracted with the code *StarFinder* by Diolaiti et al. (2000). Each exposure was deconvolved with a Lucy-Richardson deconvolution and restored with a Gaussian beam. The flux of Sgr A* and other compact sources in the field was obtained via aperture photometry on the diffraction-limited images. The background flux density was determined as the mean flux measured with apertures of the same size at five different positions in a field that shows no individual stars. Photometric calibration was done relative to stars in the field with a known flux. For the extinction correction we assumed

$A_K = 2.8\,\mathrm{mag}$ (Eisenhauer et al., 2005). Estimates of uncertainties were obtained from the standard deviation of fluxes of nearby constant sources. The calibration was performed using the overall interstellar polarization of all sources in the field, which is 4% at 25° (Eckart et al., 1995; Ott et al., 1999).

Fig. 3.2 (top) shows the dereddened light curve of Sgr A* for all four measured polarization angles. Please note that the flux was calibrated relative to stars of known flux in the field-of-view for each angle separately. Therefore, the mean of the shown lightcurves is as high as the total flux of a source, i.e., actually the figure shows twice the flux for each angle (the same convention was used in Eckart et al., 2006b).

The lightcurve shown in Fig. 3.2 shows that two peaks, i.e. sub-flares, can clearly be distinguished at all four polarization angles. In contrast to the data of 2005 (next section and Eckart et al., 2006b), these two sub-flares show up in each polarization channel.

Fig. 3.3 shows a periodogram of the emission from Sgr A* for the first 50 min of the flare. For clarity, the periodogram has been oversampled by a factor of two. A clear peak is present at a period of 15.5±2 min. There is no indication of red noise. This was also checked by plotting a log-log version of the periodogram, where red-noise would show up as a straight line with slope one. It is certainly statistically questionable to infer quasi-periodicity from just two peaks. However, considering that very similar periodicities have already been reported for several NIR flares clearly changes the picture. The probability of this happening in the case of pure red noise is extremely low (see discussion in the next section).

The Stokes parameters I, Q, and U were obtained by measuring the flux at position angles (PA) of the electric field vector of 0°, 45°, 90°, and 135° (E of N). The total flux, the polarization angle, and polarization degree can be inferred from the single polarization channels and are also shown in Fig. 3.2 (lower panel). The PA of $80° \pm 10°$ during the sub-flares agrees very well with the value of $60° \pm 20°$ reported by Eckart et al. (2006b, see next section). This is a strong indication of a stable arrangement of the accretion flow with respect to the spin axis of the MBH, which may point to a permanent accretion ring with a radial extent of $\sim 2\,R_S$ (see also Chapter

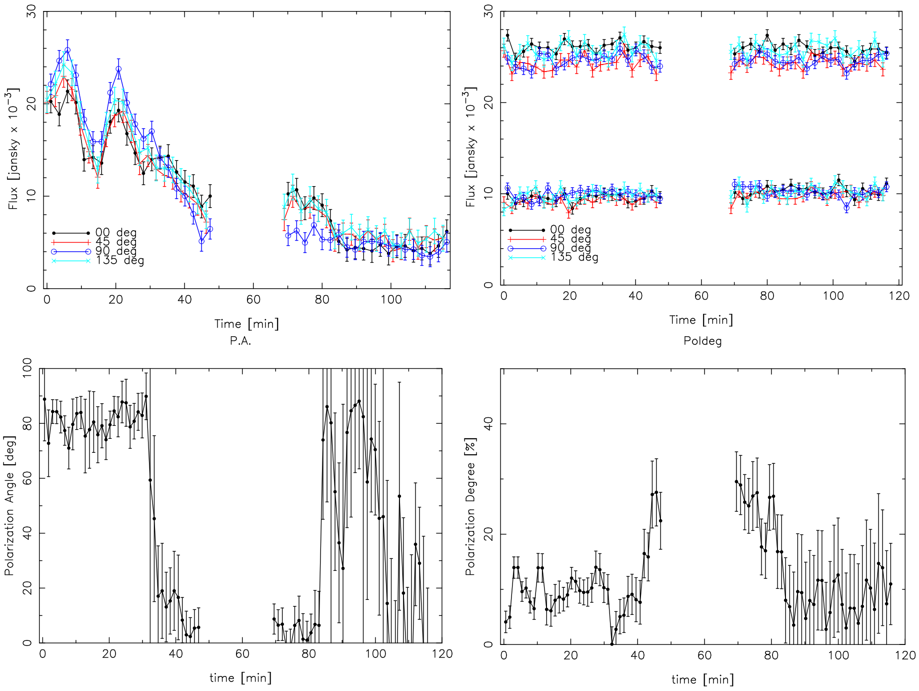

Figure 3.2: *Dereddened flux of Sgr A* (top left) and of the two comparison stars W6 and S7 (top right) at the different polarization angles. The comparison stars are located within* $< 1''$ *of Sgr A*. Due to the presence of two stellar sources at the position of Sgr A* (see Fig. 1 in Eisenhauer et al., 2005), its lightcurve stays at a constant level of about 5 mJy after the flare. The light curves of the channels have been calibrated to an overall polarization of 4% at an angle 25° east of north (Eckart et al., 1995; Ott et al., 1999). Also, the curves are shifted to the* total *flux of the sources, i.e. the flux per channel is only half of the flux shown in the plots. The inferred polarization angle (bottom left) and the degree of linear polarization (bottom right) of Sgr A* are also shown.*

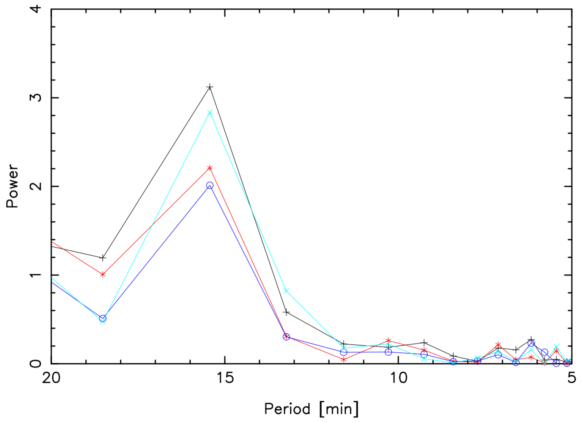

Figure 3.3: *Periodogram of the lightcurves of Sgr A* for all four observed polarization angles. The periodogram has been oversampled by a factor of 2.*

5 and Moscibrodzka et al., 2006). Therefore the flow is probably not fully advective very close to the BH horizon. Since the accretion over a disk is more effective than that of an advective flow, solutions within radiatively inefficient accretion flows (RIAFs) might be preferred where $\dot{M}$ is small and the outflow is large.

A striking feature is the large amplitude of the two sub-flares. It reaches about 50% of the overall flare intensity. The observed frequencies of QPOs in X-ray binaries scale with the BH mass, which can be extrapolated to the mass of Sgr A*. Therefore the large amplitude is remarkable since the amplitude of high-frequency QPOs observed for X-ray binaries shows variability amplitudes not larger than a few percent (see reviews by Nowak & Lehr, 1998; McClintock et al., 2004).

The lightcurves show an interesting feature between $\sim 40-85$ min. The polarization degree rises sharply up to $\sim 30\%$ and the PA swings to 0° (see Fig. 3.2). It is not clear whether this is an effect intrinsic to Sgr A*. The feature occurs after the bright flare phase, when Sgr A* is quiescent, i.e. in a low flux state. Therefore the polarization measurements are less certain. On the other hand, this feature shows some robustness, as it is visible before and after the sky observations. Also, the FWHM of the PSFs that have been extracted from each image shows no conspicuous behavior during that time, which means that the AO correction is most probably not responsible for this property of the lightcurves. It could be possible that this effect is a flare of Sgr A* that is mainly visible in polarization. A similar observation was recently made by Eckart et al. (2006b), who found that some sub-flares may only show up in the polarized flux. These observations will be described now.

3.2.2 The observations from 2005

The same polarimetric experiment as described above was also done in 2005. We observed Sgr A* with NACO during the night between 29 and 30 July 2005. The atmospheric conditions (and consequently the AO correction) were stable during the observations with optical seeing values ranging between $0.5''$ and $0.8''$. Therefore the AO could provide a stable correction with a high Strehl ratio (of the order 50%).

Fig. 3.4 shows the reduced and calibrated dataset. Three sub-flares can be identified. But note that sub-flare 2 (as labeled in Fig. 3.4) can mainly be seen in the 90°channel. A non-polarimetric measurement would have missed the peak and therefore the detection of the QPO. That there is indeed a periodic signal can be seen in the periodograms depicted in Fig. 3.5.

So, up to now, quasi-periodicities in NIR flares from Sgr A* have been reported for the four K-band flares described in Genzel et al. (2003a), Eckart et al. (2006b), and Meyer et al. (2006a). In fact, every time sub-flares have been observed so far, they showed a period that lies within the $20 \pm 3\,\mathrm{min}$ interval. The likelihood of seeing sub-flares at this interval in consecutive observations is small. The probabilities multiply and can be estimated simply: the probability to detect a peak in the periodogram of a single observation is at most at the percent level, see Fig. 3.1. That means that the chance to observe a peak at the same frequency interval in three runs that consecutively showed sub-flares is $\sim 0.1\%$, and $\sim 0.01\%$ for a fourth NIR flare showing sub-flares with a period of $\sim 20\,\mathrm{min}$. Therefore we believe that the evidence for an intrinsic cause of these modulations must be taken serious.

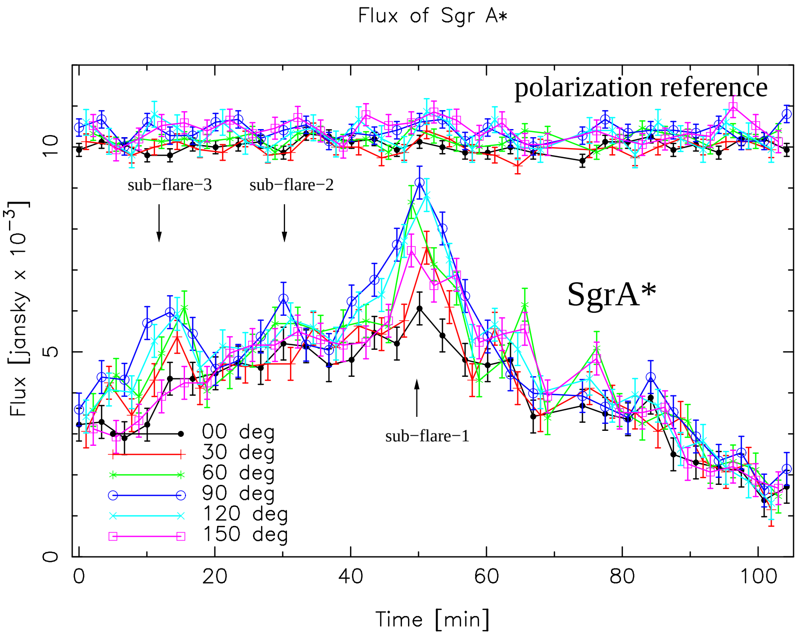

Figure 3.4: *Flux density at different PAs of the Wollaston prism for the polarization reference star* $\sim 0.38''$ *north of Sgr A* and the NIR counterpart of Sgr A* on the nights between 29 and 30 July 2005. Six polarization angles 0°, 30°, 60°, 90°, 120° and 150° (East of North) were used. For display purposes the flux density values of the reference star have been shifted upwards by 5 mJy.*

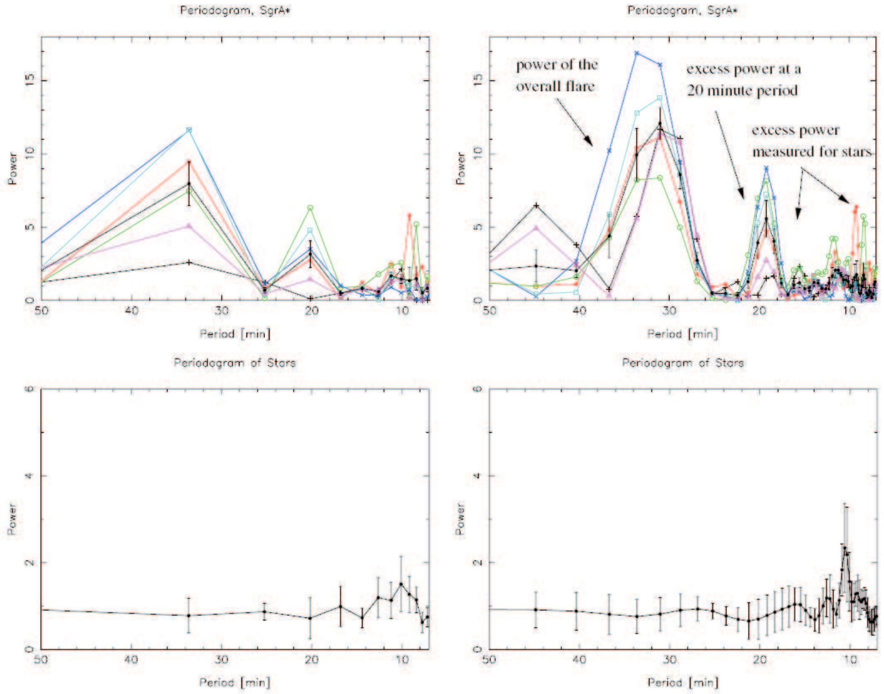

Figure 3.5: *Top left: periodogram of the July 2005 polarized flux density data from SgrA* at individual polarization angles (see color coding information in Fig. 3.4) and for the mean (black). Bottom left: mean and standard deviation calculated from periodograms of 7 stars within* $1.5''$ *radius of Sgr A*. Top and Bottom right: the same as top and bottom left but oversampled in order to allow a better estimate of the peak widths. Note that both the mean and PA* 0° *curves are printed in black. They can, however, be clearly distinguished from each other since only the data points of mean curve have error bars associated with them.*

The above described evidence for QPOs all come from $2.2\,\mu$m observations conducted at the VLT. Their detection at longer wavelengths has not yet been reported on. The reason for this may be indicative for a lower sub-flare contrast at longer wavelengths due to intrinsic spectral properties of the source and to the fact that at these wavelengths flux contributions from an extended dust component complicates the determination of the flux density from Sgr A* (Eckart et al., 2006a; Ghez et al., 2005b). Concerning the X-ray regime, there seems to be also one fairly firm case of QPOs in a flare observed by XMM (Belanger et al., 2006).

Chapter 4

The Kerr metric and observables

In the remaining part of the thesis we will interpret the QPOs in terms of a relativistically orbiting blob. This chapter therefore introduces some basic concepts of General Relativity like they can be found in many textbooks (for recent books see e.g. Carroll, 2004; Hartle, 2003; Wald, 1984). In the last section we will also sketch the functioning of the ray-tracing code by Dovciak et al. (2004) that has been used for the modeling described in the following chapters. Throughout this chapter we use geometrized units, in which $G = 1$ and $c = 1$ where mass, length, and time all have units of length.

4.1 The general theory of relativity

If General Relativity (GR) had to be summarised in one sentence, one good phrase would be: gravity is not a force, it's geometry! Spacetime is curved and without interactions other than gravity, test-particles still move on geodesics. But due to the curvature of spacetime, these geodesics are not straight lines anymore. In this sense gravity is not a term on the right hand side of Newton's second law, $m\,\vec{a} = \vec{F}$, but a whole new equation of motion has to be derived.

The fact that spacetime can be curved was the ingenious insight of Albert Einstein. This idea is motivated by Einstein's Equivalence Principle: *In small enough regions of spacetime, the laws of physics reduce to those of special relativity; it is impossible to detect the existence of a gravitational field by means of local experiments.* The fact that in small enough regions of spacetime a gravitational field cannot be detected leads to the mathematical concept of a curved manifold, because a manifold is, roughly speaking, a set of points that looks locally like $\mathbf{R^n}$ (e.g. a n-dimensional sphere or torus). Furthermore, the crucial property of gravity is its universality. It cannot be screened and it affects all particles (energy-momentum) in the same way. Einstein's idea was that something so universal could be most easily described as a fundamental feature of the background on which matter fields propagate, as opposed to a conventional force.

A major consequence of the spacetime curvature is that the concept of a derivative has to be changed. To differentiate a function means to compare its value at different places with respect to the same coordinate system. But if spacetime is curved, the coordinate system gets rotated from point to point. Therefore a quantity is needed that lets the derivative become a true tensor. The desired quantity is a collection of numbers which are called the connection coefficients $\Gamma^{\nu}_{\mu\lambda}$. Now a covariant derivative can be defined:

$$\nabla_\mu V^\nu = \partial_\mu V^\nu + \Gamma^{\nu}_{\mu\lambda} V^\lambda, \tag{4.1}$$

where V^ν is a four vector and ∂_μ is the ordinary partial derivative $\partial/\partial x^\mu$. Throughout the thesis we use the common four vector notation in which Greek superscript indices run from 0 to 3 so that e.g. x^μ stands for $x^0 = c\,t$, $x^1 = x$, $x^2 = y$, $x^3 = z$. The connection coefficients, in turn, are defined in terms of the spacetime metric tensor $g_{\mu\nu}$:

$$\Gamma^{\nu}_{\mu\lambda} = \frac{1}{2} g^{\nu\sigma} \left(\partial_\mu g_{\lambda\sigma} + \partial_\lambda g_{\sigma\mu} - \partial_\sigma g_{\mu\lambda} \right). \tag{4.2}$$

The metric is *the* basic quantity in GR. As we will see, it[1] (i) replaces the Newtonian gravitational field; (ii) allows the computation of path length and proper time; (iii) determines the shortest distance between two points and therefore the motion of test particles; (iv) supplies a notion of past and future; (v) provides a notion of locally inertial frames and therefore a sense of 'no rotation'; (vi) determines causality; (vii) replaces the traditional Euclidean three-dimensional dot product of Newtonian mechanics.

---

[1] The following list is adopted from Carroll (2004).

With the notion of the covariant derivative at hand we can now proceed to motivate the equation of motion for freely-falling particles in GR. In Newtonian physics force-free particles move on straight lines. This can be expressed as the vanishing of the second derivative of the parametrized path $x^\mu(\lambda)$, where λ is an affine parameter (e.g. the proper time in case of a massive test particle):

$$\frac{d^2x^\mu}{d\lambda^2} = 0.$$

Using the chain rule this becomes

$$\frac{d^2x^\mu}{d\lambda^2} = \frac{dx^\nu}{d\lambda}\frac{\partial}{\partial x^\nu}\frac{dx^\mu}{d\lambda} = 0.$$

If spacetime is curved, the ordinary derivative has to be replaced with the covariant one. This leads to

$$\frac{dx^\nu}{d\lambda}\nabla_\nu\frac{dx^\mu}{d\lambda} = \frac{d^2x^\mu}{d\lambda^2} + \Gamma^\mu_{\rho\sigma}\frac{dx^\rho}{d\lambda}\frac{dx^\sigma}{d\lambda} = 0.$$

The right hand side is the famous geodesic equation:

$$\frac{d^2x^\mu}{d\lambda^2} + \Gamma^\mu_{\rho\sigma}\frac{dx^\rho}{d\lambda}\frac{dx^\sigma}{d\lambda} = 0. \tag{4.3}$$

It describes the motion of force-free test particles in a curved background, i.e. under the influence of gravity. This is the analogue to $m\ddot{x} = 0$ in Newtonian physics.

This equation is of crucial importance in this thesis, as the photons from Sgr A* travel along geodesics to the earth. They are emitted very close to the BH horizon and there the shape of the geodesics differs significantly from straight lines. As we will see in the next two sections, equation (4.3) has to be integrated numerically to model the polarimetric NIR lightcurves from Sgr A*.

The quantity needed to solve the geodesic equation is the metric tensor $g_{\mu\nu}$. It – and therefore the curvature of spacetime – is determined by the presence of energy-momentum. This relationship is manifested in Einstein's equations, which is the heart of GR:

$$R_{\mu\nu} - \frac{1}{2} R g_{\mu\nu} = 8\pi G T_{\mu\nu}, \tag{4.4}$$

$R_{\mu\nu}$ is the Ricci tensor, R is the Ricci scalar, G is Newton's constant of gravitation and $T_{\mu\nu}$ is the energy-momentum tensor. For the exact definition of these quantities see e.g. Carroll (2004). Here we just want to mention that the Ricci tensor and scalar are functions of the metric and its first and second derivatives. Hence, Einstein's equation is a set of second-order differential equations for the metric tensor field $g_{\mu\nu}$.

We give equation (4.4) here merely for completeness. In this thesis we don't need to worry about it as the solution describing a spinning BH was found in 1963 by Roy Kerr. We will explore this metric in the following section.

4.2 The spacetime around a spinning black hole

We are interested in a BH solution of Einstein's equation, i.e. a solution that has the property of an event horizon. An event horizon is a hypersurface that separates those spacetime points that are connected to infinity by a timelike path from those that are not. It is remarkable that only a very small number of stationary BH solutions exist in classical GR. If electromagnetism is the only long-range non-gravitational field, three parameters suffice to describe every BH solution. This is the statement of the no-hair theorem: *Stationary, asymptotically flat BH solutions to GR coupled to electromagnetism that are nonsingular outside the event horizon are fully characterized by the parameters of mass, electric charge, and angular momentum.* We are interested in stationary solutions because they are the outcome of a gravitational collapse. Furthermore, in astrophysical applications a charged BH will be quickly neutralized by interactions with matter in the vicinity of the hole. Hence, we only need to deal with two parameters: mass and spin.

The solution to Einstein's equation describing a BH with mass M and angular momentum per unit mass a was found by Roy Kerr. In the so-called

Boyer-Lindquist coordinates (t, r, θ, ϕ) the metric tensor (here expressed through an infinitely small line element $ds^2 = g_{\mu\nu}\, dx^\mu\, dx^\nu$) reads

$$\begin{aligned} ds^2 &= -\left(1 - \frac{2Mr}{\rho^2}\right) dt^2 - \frac{4Mar\sin^2\theta}{\rho^2}\, dt\, d\phi + \rho^2\, d\theta^2 \\ &\quad + \frac{\rho^2}{\Delta}\, dr^2 + \frac{\sin^2\theta}{\rho^2}\left((r^2+a^2)^2 - a^2\Delta\sin^2\theta\right) d\phi^2, \end{aligned} \tag{4.5}$$

where

$$\Delta \equiv r^2 - 2Mr + a^2, \qquad \rho^2 \equiv r^2 + a^2\cos^2\theta.$$

Remember that we have set $G = c = 1$. A derivation of the Kerr metric can e.g. be found in the book by Straumann (2004).

Note that for $a \to 0$ the familiar Schwarzschild solution is recovered. For a fixed and $M \to 0$ flat spacetime shows up, not in polar coordinates but in ellipsoidal coordinates. The Kerr metric is singular when ρ vanishes and when Δ vanishes. This is similar to the Schwarzschild case where one singularity turns out to be a true singularity (at $r = 0$), and one is a mere coordinate singularity, which disappears in other coordinate systems, but turns out to give the location of the event horizon. With this similarity in mind, we just want to present the results of the singularity studies for the Kerr case. Details can be found e.g. in the books by Wald (1984) or Hartle (2003).

The singularity at $\rho = 0$, which happens when $r = 0$ and $\theta = \pi/2$, is a real singularity, i.e. a place of infinite spacetime curvature. It is the generalization of $r = 0$ in the Schwarzschild case, and in fact for $a = 0$ this value is recovered. For $a \neq 0$ the singularity is not a point in spacetime anymore, but a ring with radius a. Remember that for $M \to 0$ flat spacetime with *ellipsoidal* coordinates is described.

The other singularity can then be expected to be a coordinate singularity which gives the location of the event horizon. We have

$$\Delta = r^2 - 2Mr + a^2 = 0,$$

what leads us to

$$r_\pm = M \pm \sqrt{M^2 - a^2}. \tag{4.6}$$

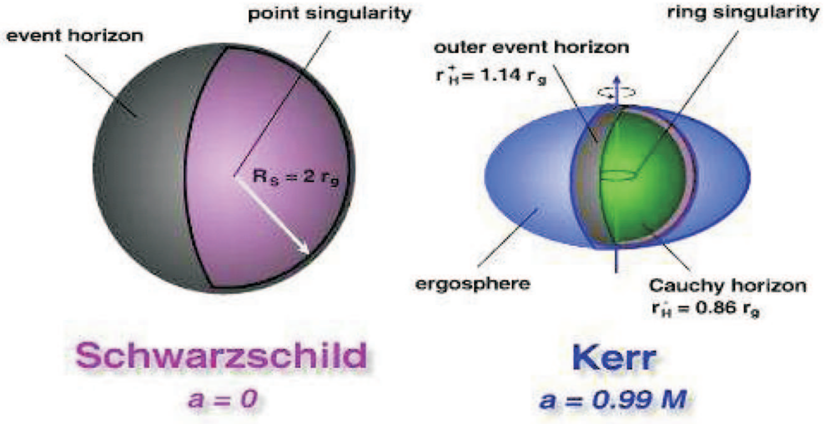

Figure 4.1: *The structure of the event horizons, the singularities and the ergosphere for a Schwarzschild (left) and a Kerr (right) BH.* R_S *is the Schwarzschild radius,* $R_S = 2GM/c^2$, *and* r_g *is the gravitational radius,* $R_S = 2r_g$. *The* $r_H^{\pm}$ *is denoted by* $r_{\pm}$ *in the text. From Müller (2007).*

For $a > M$ the solution would lie in the complex plane. In this case there would be no event horizon and a naked singulartity, i.e. a singularity which is not hidden behind a horizon, would remain. Following the cosmic censorship conjecture (e.g. Wald, 1997): *Naked singularities cannot form in gravitational collapse from generic, initially nonsingular states in an asymptotically flat spacetime obeying the dominant energy condition*, we restrict ourselves to values $a \leq M$. Both solutions $r_{\pm}$ are event horizons, but of course only the outer one r_+ is of astrophysical relevance. r_- is a so-called Cauchy horizon and marks the end of predictability.

The Kerr metric possesses another interesting feature: Close to the outer event horizon is a region in which no stationary observers are allowed. Every massive body is necessarily dragged along with the Black Hole's rotation inside this region. It is possible to enter and leave that area called the ergosphere, but it is not possible to remain stationary. Figure 4.1 summarizes the horizon structures for a Schwarzschild and a Kerr BH.

The BH nature of Sgr A* is certain beyond reasonable doubt (see Chapter 1 and the references given there). It grows by accreting matter. Most of the matter inevitably has angular momentum, and therefore also Sgr A* can be expected to have angular momentum, i.e. $a \neq 0$. Its gravitational field is hence necessarily described by the Kerr spacetime metric. To describe the matter that gets accreted, and the photons that travel along trajectories from Sgr A* to the earth, we need to solve the geodesic equation with the Kerr metric. Like in classical Newtonian mechanics, possible constants of motion can be used to simplify the task of solving the equation of motion dramatically. With enough constants of motion only a set of *first*-order differential equations has to be solved. Luckily, the Kerr spacetime offers four constants of motion so that the problem can be reduced to four coupled equations, for each spacetime coordinate one.

As a Kerr BH is stationary, the total energy $E = -p_t$ is conserved. Here, the minus sign is needed to have the energy positive at infinity. Due to the axisymmetry, the component of angular momentum parallel to the rotation axis, $L = p_\phi$, is conserved as well. There is another constant of motion, called Carter's constant (Carter, 1968), that has no obvious physical cause (for its interpretation see below):

$$Q = p_\theta + \cos^2\theta \, \left(a^2(\mu^2 - p_t^2) + p_\phi^2/\sin^2\theta\right) .$$

Here μ is the rest mass of the test particle. We will set $\mu = 0$ in the following, as we are mainly interested in photons. Otherwise we could set $\mu = 1$ for particles and deal with E, L and Q on a per unit rest mass basis. A trivial fourth constant is $p_\mu \, p^\mu = -\mu = 0$ (for photons). With an affine parameter λ and $p^\mu = dx^\mu/d\lambda$ we arrive then at (Bardeen et al., 1972):

$$\rho^2 \frac{dt}{d\lambda} = -a(aE\sin^2\theta - L) + (r^2 + a^2)T(r)/\Delta, \tag{4.7}$$

$$\rho^2 \frac{dr}{d\lambda} = \pm\sqrt{V(r)}, \tag{4.8}$$

$$\rho^2 \frac{d\theta}{d\lambda} = \pm\sqrt{V(\theta)}, \tag{4.9}$$

$$\rho^2 \frac{d\phi}{d\lambda} = -\left(aE - L/\sin^2\theta\right) + aT(r)/\Delta, \tag{4.10}$$

with

$$\begin{aligned} V(r) &= T(r)^2 - \Delta\left((L-aE)^2 + Q\right), \\ V(\theta) &= Q - \cos^2\theta\left(L^2/\sin^2\theta - a^2E^2\right), \\ T(r) &= E(r^2+a^2) - L\,a. \end{aligned}$$

The most important class of orbits is the circular orbits within the equatorial plane of the Kerr BH, i.e. the plane normal to its symmmetry axis. The matter that gets accreted has angular momentum and is most likely initially orbiting around the BH in arbitrary planes at large radii. Interactions between matter on different planes force it to settle in one common plane which will be the equatorial plane (Bardeen & Petterson, 1975). The circular orbits are so prominent, because it is much easier to lose energy (via radiation) than angular momentum, and every orbit with fixed angular momentum and minimal energy is a circular orbit.

A necessary and sufficient condition for the motion of a test particle to stay in the equatorial plane for all time is $Q = 0$. Every orbit with $Q > 0$ crosses the equatorial plane. For a particle to describe a circular orbit at radius r, its initial radial velocity, and the radial acceleration must vanish:

$$V(r) = 0, \qquad \text{and} \qquad \frac{dV(r)}{dr} = 0.$$

These equations can be solved for E and L. Then, by dividing the resulting expression for $d\phi$ by the one for dt, one arrives at the angular velocity of a circular orbit:

$$\frac{d\phi}{dt} \equiv \Omega = \pm\frac{M^{1/2}}{r^{3/2} \pm aM^{1/2}}, \tag{4.11}$$

see also equation (3.1). Here, the upper sign refers to direct (corotating with $L > 0$) orbits, while the lower signs refers to retrograde (counterrotating with $L < 0$) orbits. This equation is valid for photons as well as massive particles.

Not all circular orbits are stable. Stability requires

$$\frac{d^2V(r)}{dr^2} \leq 0,$$

which yields

$$r \geq r_{\mathrm{ISCO}},$$

where r_{ISCO} is the innermost stable circular orbit. It reads:

$$\begin{aligned} r_{\mathrm{ISCO}} &= M\left(3 + Z_2 \mp \sqrt{(3 - Z_1)(3 + Z_1 + 2Z_2)}\right), \qquad (4.12) \\ Z_1 &= 1 + (1 - a^2/M^2)^{1/3}\left((1 + a/M)^{1/3} + (1 - a/M)^{1/3}\right), \\ Z_2 &= \sqrt{3a^2/M^2 + Z_1{}^2}. \end{aligned}$$

The existence of an innermost stable circular orbit is a purely relativistic effect. This orbit is extremely important in BH astrophysics. Suppose a BH is surrounded by an accretion disk. The time evolution of a matter element within the disk is roughly the following: it is moving along a practically circular orbit, slowly losing its angular momentum (probably through the so called magneto-rotational instability, Balbus & Hawley, 1991). After some time it reaches the position of the ISCO. After that, it falls almost freely into the BH (without the need of removing any further angular momentum). Magnetic field effects within the accretion flow could alter this behavior, because the above conclusions hold for geodesics only. But matter subject to non-gravitational forces will in general not follow a geodesic. Nevertheless, the ISCO should be a good approximation for the boundary that separates stable circular orbits within the equatorial plane from unstable ones (Krolik & Hawley, 2002).

4.3 The concept of a transfer function

Now that we know the metric of the spacetime around a (possibly) spinning BH, we can tackle the task of computing the influence of strong gravity effects on electro-magnetic radiation, that is emitted by the accreted matter. To do this, Cunningham (1975) introduced the concept of a transfer function. Such a function relates the flux as seen by a local observer comoving with an accretion disk to the flux as seen by an observer at infinity. To account for all relativistic effects several transfer functions are needed, as it will be shown in this section.

In this thesis, the so-called KY code by Dovciak et al. (2004) has been used to calculate the relativistic effects. It offers pre-calculated and stored transfer functions for various values of the BH spin parameter and the viewing angle. So, what follows is a description of how the transfer functions are calculated in their code, and how they can be used to model the relativistic imprints in the flux of Sgr A*. As all the details concerning the KY code can be found in Dovciak et al. (2004) and Dovciak (2004), we here merely give a sketch of the underlying methods.

Let us consider the gravitational and Doppler frequency shift first. As the emitting matter is in orbital motion around the BH, the radiation will be Doppler red shifted on the receding side of the accretion disk and blue shifted on the approaching side. Also, the photons have to move out of the BH's potential well and will therefore be red shifted. The combined shift, the so called g-factor, is the ratio of the observed photon frequency ν_o and the emitted frequency ν_e:

$$g = \frac{\nu_o}{\nu_e} = \frac{p_{o\,t}}{p_{e\,\mu} U^\mu} = \frac{E_\infty}{p_{e\,\mu} U^\mu}. \tag{4.13}$$

Here, $p_{o\,t}$ means the time component of the photon's four momentum as measured by an observer who is at rest at infinity (that is why the 0th-(time) component is projected out). Note that the energy at infinity has been normalized to -1 in Dovciak et al. (2004). $p_{e\,\mu}$ means the four[2] momentum of the emitted photons, U^μ is the velocity of the accreted matter that emits the photons. As we are assuming that single elements in the accretion disk are moving on circular orbits within the equatorial plane, the velocity is known as a function of radius. But the momentum of the emitted photons is needed. Eqs. (4.7)-(4.10) reveal that for every r and ϕ the constants of motion L and Q are needed. Therefore, the geodesic equation (4.3) has to be integrated numerically from infinity (observer) to the disk, which is optically thick and geometrically thin. Only null geodesics starting at the observer at infinity and ending at the equatorial plane of the BH (without crossing it) have been taken into account. In the code of Dovciak et al. (2004) approximately 10^5 geodesics have been integrated. They cover the disk from the event horizon to an outer radius of $\sim 500 R_S$

---

[2] We will neglect the additional 'four' in the following. It should be clear whether four- or ordinary three-vectors are meant.

in such a way that the region closest to the horizon is most densely covered. They have thus obtained values of the transfer function on a non-regular grid over the disk, which have been interpolated to a regular grid.

Of course, not only the frequency of the emitted photons gets changed but also the emission angle, i.e. aberration is important as well. The general relativistic expression for the emission angle is in analogy to special relativity:

$$\mu_e = \cos\delta_e = -\frac{p_{e\,\alpha}\, n^\alpha}{p_{e\,\mu}\, U^\mu}, \tag{4.14}$$

where n^α are the known components of the disk normal.

The g-factor and the emission angle are just two examples of transfer functions. To completely describe the influence of strong gravity on the *intensity* of light, the effect of lensing still needs to be invoked. In Dovciak et al. (2004) the lensing function l is defined as the ratio of the cross section of the light tube at infinity to the cross section of the same light tube at the disk. Again a numerical integration is needed, see Dovciak (2004) for details. Furthermore, as the local emission from the disk within our hot spot model is non-stationary, it is necessary to take the relative time delay with which photons from different parts of the disk arrive at the observer into account.

The question remains how exactly these transfer functions have to be used to convert the local flux at the disk to the flux at the observer. Let $N_l(E_l, r, \phi, \mu_e, t-\Delta t)$ be the local flux at the disk (the local number of photons[3]) with energy in the interval $[E_l, E_l + dE_l]$, at radius r and angle ϕ, with emission angle μ_e, emitted at time $t - \Delta t$ (Δt is the relative time delay with which photons arrive at the observer from different parts of the disk). Then the integrated flux per energy interval, ΔE, at the observer within a solid angle Ω is (see equation (2.11) in Dovciak, 2004):

$$\begin{aligned}\Delta N_o^\Omega(E, \Delta E, t) \quad = \quad & N_0 \int_{r_{in}}^{r_{out}} dr \int_\phi^{\phi+\Delta\phi} d\tilde{\phi} \int_{E/g}^{(E+\Delta E)/g} dE_l \\ & \cdot N_l(E_l, r, \tilde{\phi}, \mu_e, t-\Delta t)\, F\, r, \end{aligned} \tag{4.15}$$

---

[3] It is important to note that in Dovciak et al. (2004) the properties of radiation are described in terms of photon numbers as it is common in X-ray astrophysics.

with $F \equiv F(r,\phi) = g^2\, l\, \mu_e$, the so called overall transfer function. So, we see that the product $g^2\, l\, \mu_e$ of transfer functions describes the changes in the light intensity which are due to relativistic effects.

The emission mechanism responsible for the radiation from Sgr A* is synchrotron radiation. Therefore we can expect the light to be partially polarized. Indeed, as we have seen in Chapter 3, recent polarimetric measurements in the optically thin regime have verified this expectation. So, also the effects of spacetime curvature on the polarimetric properties of the radiation have to be investigated. A direct consequence of the curvature is that the polarization vector gets rotated as the light propagates through spacetime. Therefore, one additional transfer function that describes the change of the polarization angle that occurs between the emission of light at the disk and its reception by the observer at infinity is needed. One method to calculate this change of the polarization vector is to integrate the equation of parallel transport along the geodesic. However, Connors & Stark (1977) introduced a method which is more elegant as it exploits a complex constant of motion (Walker & Penrose, 1970). When we want to describe the local intrinsic polarization of the emitting source at the disk (which depends on the source geometry as well as the geometry of the magnetic field), we also need to involve the azimuthal emission angle of the photons. Thus, two more transfer functions are needed when also the polarization of the radiation is under investigation. For more details concerning these two functions the reader is again referred to Dovciak (2004).

Stokes parameters are used for the polarization studies. Let us remember briefly how they are defined. Consider an almost monochromatic, plane electromagnetic wave propagating in the z-direction. The components of the electric field vector at a given point in space can be written as

$$E_x = a_x(t)\cos\left(\omega_0 t - \theta_x(t)\right), \qquad E_y = a_y(t)\cos\left(\omega_0 t - \theta_y(t)\right).$$

Almost monochromatic means here that all time dependent quantities develop slowly compared to ω_0^{-1}. The Stokes parameters are now defined as the following temporal means:

$$\begin{aligned}
I &\equiv \langle a_x^2\rangle + \langle a_y^2\rangle && \text{(intensity)}, && (4.16)\\
Q &\equiv \langle a_x^2\rangle - \langle a_y^2\rangle && \text{(horizontal/vertical polarization)}, && (4.17)\\
U &\equiv \langle 2a_x a_y \cos(\theta_x - \theta_y)\rangle && (+45^o \text{ / -}45^o \text{ polarization}), && (4.18)\\
V &\equiv \langle 2a_x a_y \sin(\theta_x - \theta_y)\rangle && \text{(circular polarization)}. && (4.19)
\end{aligned}$$

For unpolarized light we have $Q = U = V = 0$. I and V are physical observables; they are independent from the chosen frame of reference. That is not true for Q and U, which describe linear polarization. If the coordinate system is rotated in the $x - y-$ plane with the angle φ, we arrive at the new quantities Q' und U':

$$\begin{aligned}
Q' &= Q\cos(2\varphi) + U\sin(2\varphi),\\
U' &= -Q\sin(2\varphi) + U\cos(2\varphi).
\end{aligned}$$

An invariant of this transformation is

$$Q^2 + U^2 \equiv P^2, \tag{4.20}$$

where P is the linear polarized flux. The polarization angle which gives the direction of the electric field vector in the $x - y-$ plane is given by:

$$\alpha \equiv \frac{1}{2}\tan^{-1}\frac{U}{Q}. \tag{4.21}$$

In the code by Dovciak et al. (2004) the Stokes parameters are used in the following specific way:

$$i_\nu := \frac{I_\nu}{E}, \quad q_\nu := \frac{Q_\nu}{E}, \quad u_\nu := \frac{U_\nu}{E}, \quad v_\nu := \frac{V_\nu}{E},$$

where I_ν, Q_ν, U_ν, and V_ν are the Stokes parameters for light with frequency ν, and E is the energy of a photon at this frequency[4]. Now, the integrated Stokes parameters per energy bin that the observer measures can be calculated from the local ones like in eq. (4.15):

---

[4] We will drop the index ν in the following.

$$\begin{aligned}
\Delta i_o(E,\Delta E) &= N_0 \int dS \int dE_l \, i_l(E_l)\, F\, r, \\
\Delta q_o(E,\Delta E) &= N_0 \int dS \int dE_l \left(q_l(E_l) \cos 2\Psi - u_l(E_l) \sin 2\Psi \right) F\, r, \\
\Delta u_o(E,\Delta E) &= N_0 \int dS \int dE_l \left(q_l(E_l) \sin 2\Psi + u_l(E_l) \cos 2\Psi \right) F\, r, \\
\Delta v_o(E,\Delta E) &= N_0 \int dS \int dE_l \, v_l(E_l)\, F\, r.
\end{aligned}$$

Here, Ψ is the angle by which a vector parallelly transported along the light geodesic rotates, i.e. the change of the polarization angle. F is again the overall transfer function, $F = g^2\, l\, \mu_e$. The integration over dS means an integration over the two-dimensional disk. Note that the first of these equations is the same as eq. (4.15). The whole argument of the local Stokes parameters has been suppressed for simplicity.

With the Stokes parameters, as seen by an observer at infinity, at hand we can use eq. (4.20) and eq. (4.21) to arrive at the polarized flux (the degree of linear polarization is just the linear polarized flux divided by the overall flux i_o) and the polarization angle. As we are in this thesis mainly interested in lightcurves and not in spectral information, each Stokes parameter $i_o, q_o, ...$ has to be summed over and multiplied by energy before calculating the polarization degree and angle.

Chapter 5

A plasma blob close to the Black Hole horizon

We have seen in Chapter 3 that some NIR flares from Sgr A* are accompanied by quasi-periodic sub-flares. In this chapter we now model the underlying flare in terms of an accretion disk while for the sub-flares we use a somehow confined plasma blob in a relativistic orbit. Detailed fitting will constrain the parameters of the BH. Parts of this chapter have been published in Meyer et al. (2006a,b).

5.1 The underlying disk

Disk accretion is generally thought to be the source of galactic nuclear luminosity and the driver of activity whenever the angular momentum dominated disk-type accretion takes place. In the case of Sgr A*, the accretion rate onto the central black hole and the net angular momentum of the accreted gas appear to be very small ($\simeq 10^{-7} M_{\odot}$ yr^{-1}, see Bower et al., 2003) and a persistent accretion disk is not present (Coker & Melia, 1997). Despite this fact, the very occurrence of the flares and the minute timescale of their rise and decay indicate that the immediate neighbourhood of the black hole is not entirely empty; likely, episodic accretion takes place. In fact, Moscibrodzka et al. (2006) suggest that a transient torus develops at a distance of a few or a few ten gravitational radii and exists for several dynamical periods. The inner disk/torus is subject to violent instabilities, but it is difficult to identify the dominant mechanism responsible causing its destruction. This makes it tempting to attribute the outbursts to some type of disk instability, for instance of the limit-cycle type as known in dwarf novae (albeit with the possibility of a physical cause different from the hydrogen ionization/recombination there). Disks in the vicinity of black holes live in a relativistic environment, and proper modeling requires relativistic (magneto-)hydrodynamics (see e.g. Tagger & Melia, 2006). In the following, however, disk instabilities can be ruled out by such a wide margin that a non-relativistic order-of-magnitude treatment suffices our purpose.

So close to the black hole, self-gravity will not play a role, allowing for the standard one-zone approximation of the vertical hydrostatic equilibrium, which relates the azimuthal velocity v_φ, the sound velocity c_s, the (half-)thickness of the disk h, and the radius s by

$$\frac{h}{s} = \frac{c_\mathrm{s}}{v_\varphi}. \tag{5.1}$$

The rise time Δt_+ of a disk outburst may be estimated by the radial range of the disk involved in the outburst, Δs, and the propagation speed of the outburst, which is αc_s (Meyer, 1984; Liu & Melia, 2002),

$$\Delta t_+ \approx \frac{\Delta s}{\alpha\ c_\mathrm{s}} \geq \frac{\Delta s}{c_\mathrm{s}} = \frac{\Delta s}{v_\varphi}\frac{s}{h} \approx t_\mathrm{dyn}\frac{s}{h}\frac{\Delta s}{s} \tag{5.2}$$

with the dynamical timescale $t_\mathrm{dyn} \approx \frac{s}{v_\varphi}$. Here α is a parameter related to the disk viscosity and is of order unity or smaller. For the outburst to be a disk phenomenon and not just something happening in a small ring, it is required $\Delta s \gg s$.

Even for an only moderately thin disk of, let's say, $h/s = 10^{-0.5}$ this then requires rise times which are more than an order of magnitude longer than the dynamical time scale. The smallest dynamical time scale allowed for is the one at the ISCO. As discussed in Chapter 3, however, the entire outburst (rise plus decline) encompasses only a few dynamical timescales.

This ratio of the observed timescales makes a *normal* disk instability an exceedingly unlikely cause of the outbursts. It furthermore shows that, at best, a relatively small radial range of the disk ($\Delta s \sim s$), close to the ISCO, may be involved in whatever causes the outbursts.

It is, however, noteworthy that, for a moderately thin accretion disk, the duration of the outburst is of the order of the timescale a sound wave needs to travel around the black hole once. This makes a scenario attractive in which the outburst is caused by some non-axisymmetric process (be it a disk instability of a non-axisymmetric type, confined to the innermost disk regions, be it material falling into the disk there locally), and a sound wave originating from this event and traveling the inner disk until the outburst comes to an end when the actual source of it has been accreted into the black hole. While the sub-flares tracing the actual local event disappear suddenly as soon as that region has been accreted, the outburst itself ceases somewhat slower as the soundwave, of course, travels not only azimuthally, but also radially outwards, though only a small distance as shown above.

5.2 The hot spot

Motivated by these considerations, we adopt a two component hot spot/ring model in order to fit the data presented in Eckart et al. (2006b) and Meyer et al. (2006a), see Chapter 3. In this model, the broad underlying flare is caused by a truncated disk/ring. The sub-flares are due to a compact emission region on a relativistic orbit around the MBH. Such hot spots can be created e.g. in reconnection events, in which thermal electrons are accelerated into a broken power law (Yuan et al., 2004). General relativistic effects imprint on the synchrotron radiation of such inhomogeneities (Broderick & Loeb, 2005, 2006; Dovciak et al., 2004; Hollywood et al., 1995; Hollywood & Melia, 1997; Bromley et al., 2001; Falcke et al., 2000; Pineault, 1981). Redshifts, lensing, time delay, change in emission angle and change in polarization angle belong to these. The code by Dovciak et al. (2004) takes these special and general relativistic effects into account by using the concept of a transfer function (Cunningham, 1975). A transfer function relates the flux as seen by a local observer comoving with an accretion disk to the flux as seen by an observer at infinity (see Section 4.3). This transfer of photons is numerically computed by integration of the geodesic equation. Fig. 5.1 shows how an observer at infinity would see a circular spot in a relativistic orbit around a SMBH, if he had a perfect telescope and there were no interstellar scattering. For the change of polarization angle the method of Connors & Stark (1977) has been used. In the geometrical optics approximation, photons follow null geodesics and their propagation is not affected by the spin-spin interaction with a rotating black hole (Mashhoon, 1973). This means that wave fronts do not depend on the photon polarization, and so the ray-tracing through the curved spacetime of the black hole is adequate to determine the observed signal.

Following the discussion from the last section, we have fixed the radial extent of the disk to $2R_S$, beginning at an inner edge. We realize that there is a range of definitions for an inner edge that depend on the accretion rate and may be non-axisymmetric and time-variable (Krolik & Hawley, 2002). They are, however, generally located in the vicinity of the marginally stable orbit. For simplicity we have assumed that for $a_\star \gtrsim 0.5$ both coincide, and our general result – that the observed time variability is compatible with a discription of a spot/ring combination orbiting a central MBH – does not depend strongly on this assumption. Due to the observed timescale of the QPOs, the spot is within the marginally stable orbit for $a_\star \lesssim 0.5$. In this case we assumed the spot to be freely falling and the disk to have its inner edge at $\sim R_S/2$ above the event horizon. Magnetic field effects could bar the spot from freely falling (Krolik & Hawley, 2002) but require full relativistic MHD simulations that are beyond the scope of this work.

The disk/ring's time behaviour was assumed to be Gaussian and to account for the main flare. The spot is orbiting within the disk and the equatorial plane of a Kerr BH. Its intrinsic luminosity follows a two-dimensional normal distribution with $\sigma \sim 1.5R_S$, but being cut off in the radial direction to fit within the disk. The spot follows a circular trajectory ($a_\star \gtrsim 0.5$) chosen such that the observed periodicity is matched. Note that the radius for the corresponding orbit is spin dependent, see equation (3.1) or Bardeen et al. (1972). In the case $a_\star \lesssim 0.5$ the spot is freely falling and it has to be checked whether the timescale can be matched within its uncertainty.

We identify all sub-flares of each epoch with the same spot. This can well be

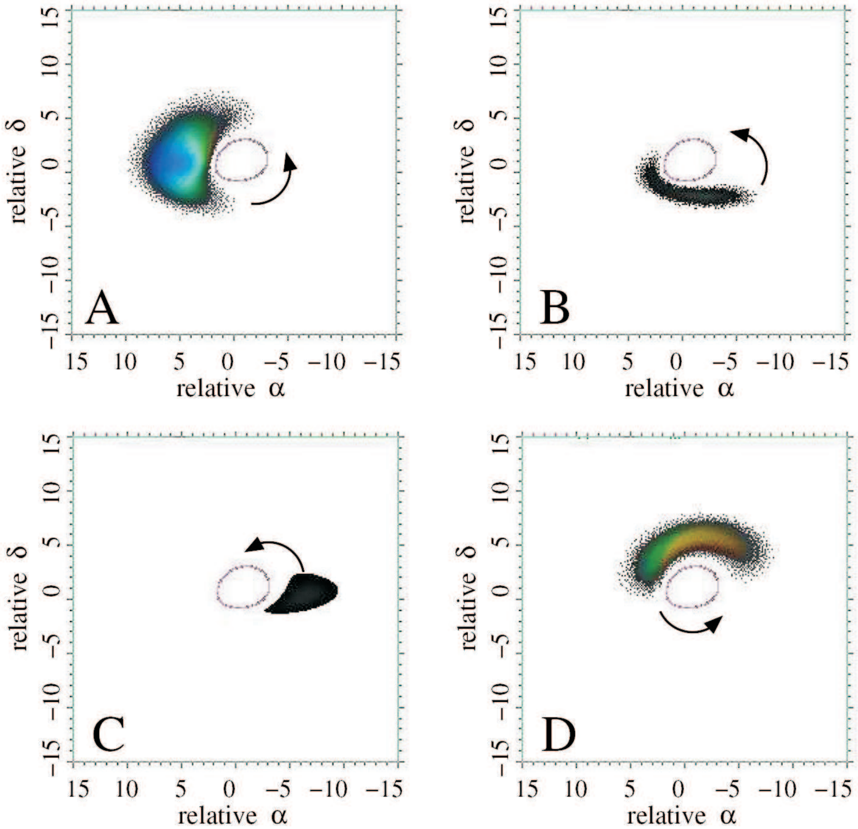

Figure 5.1: *Apparent images of an orbiting circular hot spot as seen by an observer on earth. The images have been calculated for a case of* $i = 60^\circ$*,* $a_\star = 1$ *and for a spot at a distance of four gravitational radii (*r_g*) from the Black Hole (Dovciak et al., 2004). Colours indicate the energy shift, the blackest structures correspond to the faintest spot images. The axes lables represent the relative distance from Sgr A* in units of* r_g*. Effects due to interstellar scattering and the finite resolution of a telescope are not taken into account.*

matched with the corresponding synchrotron cooling timescale (Eckart et al., 2006a,b; Yuan et al., 2003, 2004). The observed differences in the flux of each sub-flare in the 2005 data are very likely due to intrinsic changes of the spot, i.e. the spot is very likely to evolve. Regarding the fact that the physics of such an inhomogeneity in the accretion flow is unknown at present, we simply model the changes of the intrinsic luminosity by hand. This is done by changing the value for the spot luminosity discontinuously instead of some parametrization which would not be very meaningful, because we do not know the actual underlying physics. Normalized to the third revolution ($\sim 36 - 54$ min, see Fig. 5.3) the spot has an intrinsic luminosity of 50% between 0-18 min, 20% between 18-36 min and 10% after 54 min. The small jumps seen in some light curves are an artifact of this procedure.

Another approach would be to assign different spots to different sub-flares. Assuming a typical spot-lifetime of approximately one revolution and that every spot is on roughly the same radius, multiple single spots can reproduce a peak in the periodogram (Schnittman, 2005). This procedure could naturally lead to better fits, because the phase of each spot would be a free parameter for every single sub-flare. We rejected that approach, however, as it only increases the already large number of degrees of freedom.

5.3 Magnetic fields and foreground polarization

As only rough estimates can be given on the magnetic field of the spot, we did the fits for two different field configurations as an approximation (Pineault, 1981). The first configuration is such that the resulting projected E-Vector is always perpendicular to the equatorial plane. Such preferred orientation could result from perturbations in the disk similar to sunspots (see also Shakura & Sunyaev, 1973). As a second configuration we have allowed for a global azimuthal magnetic field. This behaviour may be caused by the magneto-rotational instability and is motivated by global MHD simulations (e.g. Hirose et al., 2004). Contrary to the first case, this configuration leads to a rotation of the E-vector along the orbit from a Newtonian perspective (see Fig. 5.2).

As was explained in Chapter 4, the KY code by Dovciak et al. (2004) needs local Stokes parameters to describe the intrinsic polarization. Hence, we need to translate these two magnetic field configurations into Stokes parameters. The first case is fairly easy. If we want the E-vector to be always perpendicular to the equatorial plane, we just set $i_l = q_l$, see Chapter 4. The

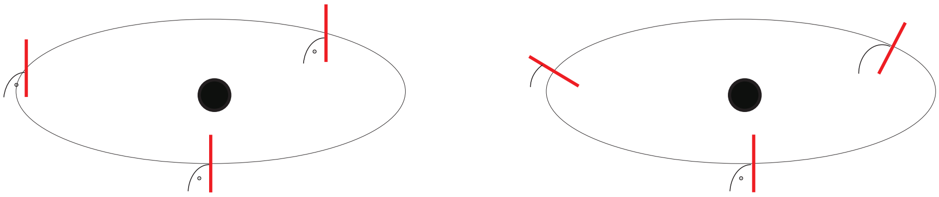

Figure 5.2: *Sketch of the Newtonian behaviour of the E-vector (red) for the two magnetic field configurations. The black circle represents the MBH, the ellipse within the equatorial plane indicates a projected Keplerian orbit of a hot spot in the local comoving frame. Left: the case where the E-vector is always constant. Right: the case of an azimuthal magnetic field (like the ellipse) where the E-vector of the emitted synchrotron radiation rotates.*

azimuthal magnetic field is slightly more involved. To arrive at an intrinsic polarization which rotates along the orbit as sketched on the right side in Fig. 5.2, the following local Stokes parameters have to be used:

$$\begin{aligned} q_l &= -i_l \cos\big(2 \arctan\left[\tan\left(\phi_e\right)\cos\delta_e\right]\big), \\ u_l &= i_l \sin\big(2 \arctan\left[\tan\left(\phi_e\right)\cos\delta_e\right]\big). \end{aligned}$$

Here, δ_e is the emission angle in the local frame co-moving with the disk, see eq. (4.14). ϕ_e is the azimuthal emission angle (in the local frame), for which also a transfer function is needed.

As the observational data include the effects of foreground polarization, these also need to be taken into account in the simulations. Following the calibration of Eckart et al. (2006b) and Meyer et al. (2006a), we fix the foreground polarization to be 3.4% at 25°. To incorporate this into the KY code, we used the formalism of so-called Mueller matrices (e.g. Serkowski, 1962). Within this formalism, the foreground polarization is treated as an imperfect polarizer. The corresponding Mueller matrix needs to be multiplied by the Stokes parameter vector $(I, Q, U, V)^T$. The result is then the Stokes vector for light that went through the imperfect polarizer. The needed Mueller matrix reads (Serkowski, 1962):

$$M \propto \begin{pmatrix} 1 & p\,\cos 2\theta & p\,\sin 2\theta \\ p\,\cos 2\theta & 1 - p\,\sin^2 2\theta & p\,\cos 2\theta \sin 2\theta \\ p\,\sin 2\theta & p\,\cos 2\theta \sin 2\theta & 1 - p\,\cos^2 2\theta \end{pmatrix}$$

The degree to which the interstellar medium polarizes an unpolarized background source is p and θ is its angle. We omitted the V component of the Mueller matrix, as it describes circular polarization and this cannot be measured with NACO yet. Accordingly, we can neglect any V part in the calculations. Note that this Stokes parameter does not couple to any of the others for an imperfect polarizer.

5.4 The fitting procedure and the treatment of higher order images

To investigate the parameters of Sgr A* we have fitted for the inclination angle i, the dimensionless spin parameter $a_\star$, the brightness excess of the spot with respect to the disk, the initial phase of the spot on the orbit, the orientation of the equatorial plane on the sky, and the polarization degree of the disk (constrained to $\leq 15\%$) and the spot ($\leq 70\%$, a value that can well be achieved via synchrotron radiation). As the last five parameters can be changed after the ray tracing, it costs little computational effort to find the least χ^2 values for given spin and inclination (we used the Levenberg-Marquardt algorithm implemented by Lourakis, 2004). For the two parameters $a_\star$ and i we have chosen a discrete grid with $0 \leq a_\star \leq 1$ and steps of 0.1 and an inclination angle $10^\circ \leq i \leq 70^\circ$ with steps of 5°; $i = 0^\circ$: face-on. For $i \gtrsim 70^\circ$ multiple images could become important, which are not included in our treatment.

Multiple images are higher order images that occur when a light ray crosses the equatorial plane of the BH several times before it reaches the observer. While they offer the unique possibility of testing general relativity in a strong field quantitatively (Broderick & Loeb, 2006), their detection is extremely difficult and lies well beyond present observational capabilities. Interferometry in the NIR or sub-mm domain may resolve this question in the future (see Chapter 7). Only for special geometries, where strong lensing is very important, they yield a non-negligible contribution (Broderick & Loeb, 2006; Bozza & Mancini, 2004; Horak & Karas, 2006a,b). The lack of multiple images in our models excludes their applicability to edge-on configurations where caustic lensing might occur (we have therefore chosen 70°as a conservative upper limit). One may, however, speculate, what signatures of multiple images to look for. Time delay between 1st and 2nd images is a very characteristic number, related to BH mass: it is given by the circumference of the photon circular orbit, $R_p = 2(1+\alpha)GM/c^2$, where $\alpha = \cos[\frac{2}{3}\arccos a_\star]$ (Bardeen et al., 1972). Hence, the expected delay is of the order of 575 $\big(M/(3.6\times10^6 M_\odot\big)$ sec in the Schwarzschild case ($a_\star = 0$; this interval becomes roughly a factor of 3 shorter in case of a maximally rotating black hole and prograde orientation of the photon trajectory, while it is about 1.3 times longer for the retrograde orientation). Unfortunately, the second image provides an order of magnitude less photons, and higher order (indirect) images are still weaker because the observed radiation flux decreases exponentially with the image order n increasing (its observed flux is roughly proportional to $\exp(-2\pi n)$; cf. Luminet, 1979), unless, again, a special geometry is assumed in which caustic lensing occurs.

In fact, the importance of significant lensing enhancement of the observed flux from accretion disks has been traditionally neglected, because it would require large inclination angles. Such geometry is not likely in case of standard (optically thick) accretion disks, because self-obscuration does not allow to observe the indirect images. However, the situation is different for optically thin flows (as noticed by Bursa et al., 2004). Therefore, Sgr A* is a suitable object in which the flux fluctuations could be considerably modulated by strong-gravity lensing if the inclination of the putative disk is very large (see also Falcke et al., 2000; Bromley et al., 2001).

In case of non-zero rotation of the BH, the expected lightcurves exhibit stronger fluctuations because the structure of light-ray caustics is more complex (e.g. Hollywood & Melia, 1997; Rauch & Blandford, 1994; Viergutz, 1993). Rapid decay of the signal strength with increasing n holds also for a rotating black hole, although the prospect of detecting the higher-order images appears even more tempting, because their mutual delays at the point of arrival and relative polarization degree can set tight constraints on the black-hole angular momentum. In conclusion, higher order images are not possible to measure yet, though it would be very useful and should be attempted in the future because their interpretation could be less ambiguous.

5.5 Results

5.5.1 The 2005 data

Figure 5.3 shows the fit with the least χ^2 value within the discrete grid discussed in Sect. 5.4 in case of a constant E-vector. High inclination and high spin give the best solutions. The case of the azimuthal magnetic field can be seen in Figure 5.4. Here high inclination and medium spin is preferred. Within the hot spot model the degree of polarization does not necessarily have to be fitted. The spot may have influence on the disk and may polarize the disk flux.

The confidence contours shown in Figure 5.5 reveal that for both magnetic field cases the spin paramter $a_\star$ cannot be well constrained from the current data with its uncertainty. Within the 3σ limit $a_\star$ can be inferred to lie in the range $0.4 \leq a_\star \leq 1$. The range of the inclination is different for the two magnetic field scenarii. As the χ^2-minimum is lower for the constant E-vector, this case should be weighted more. That means the inclination is $\gtrsim 35^\circ$ on a 3σ level.

Our solution with $a_\star \geq 0.4$ is in agreement with Genzel et al. (2003a) and Belanger et al. (2006), who inferred values of $a_\star \geq 0.5$ and $a_\star \geq 0.22$, respectively. They arrived at these lower limits by interpreting the peak in the power spectra of their measured lightcurves using the hot spot model. As it is not possible to decide where the spot is orbiting, only a lower bound can be given with the equality applying if the spot is exactly on the ISCO. Only polarimetric observations together with a relativistic modeling can improve on this within the spot model due to the additional indepent information. Our analysis of recent polarimetric measurements, however, shows that very accurate data are needed to give strong constraints on the spin parameter.

But one should be careful about the role of general relativistic effects for polarization fluctuations and there does not seem to be a clear way towards a unique interpretation at the present stage. Likewise the inferred values of $a_\star$ and the inclination are subject to many uncertainties – mainly concerning the geometry of the source and its intrinsic polarization.

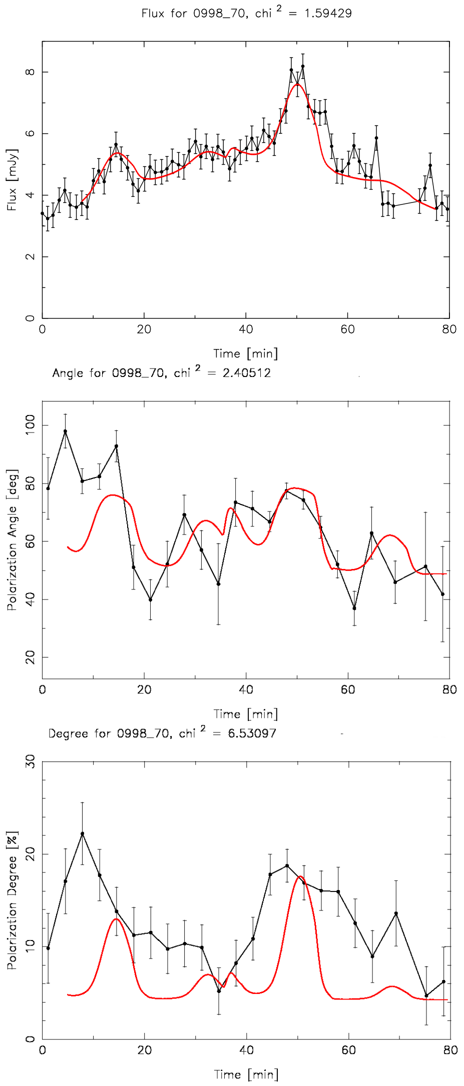

Figure 5.3: *The best fit solution (in red) for the data from 29/30 July 2005 (see Fig. 3.4). The constant E-vector scenario was assumed. Shown is the flux (top), polarization angle (middle), and polarization degree (bottom). The parameters of the fit are* $i = 70°$, $a_\star \approx 1$, *a location of the projection of the disk on the sky of* $100°$ *and a polarization degree of the disk (spot) of* 4% (60%). *The spot is orbiting at a radius* $r = 4.4r_g$. *The reduced-*χ^2 *values for each fit are indicated above each graph.*

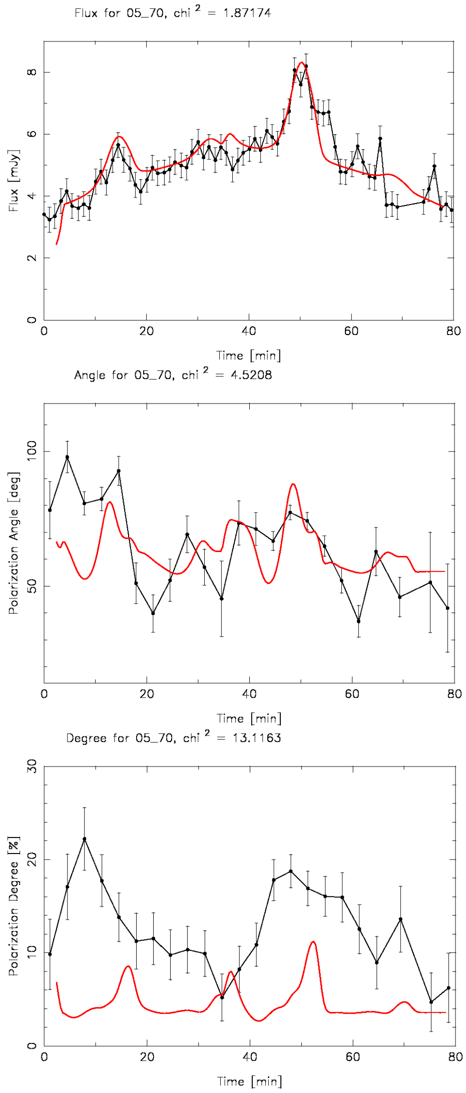

Figure 5.4: *The best fit solution (in red) for the data from 29/30 July 2005 (see Fig. 3.4). A global azimuthal magnetic field was assumed. Shown is the flux (top), polarization angle (middle), and polarization degree (bottom). The parameters of the fit are* $i = 70°$, $a_\star \approx 0.5$, *a location of the projection of the disk on the sky of* $0°$ *and a polarization degree of the disk (spot) of* 9% (60%). *The spot is orbiting at a radius* $r = 4.5r_g$. *The reduced-*χ^2 *values for each fit are indicated above each graph.*

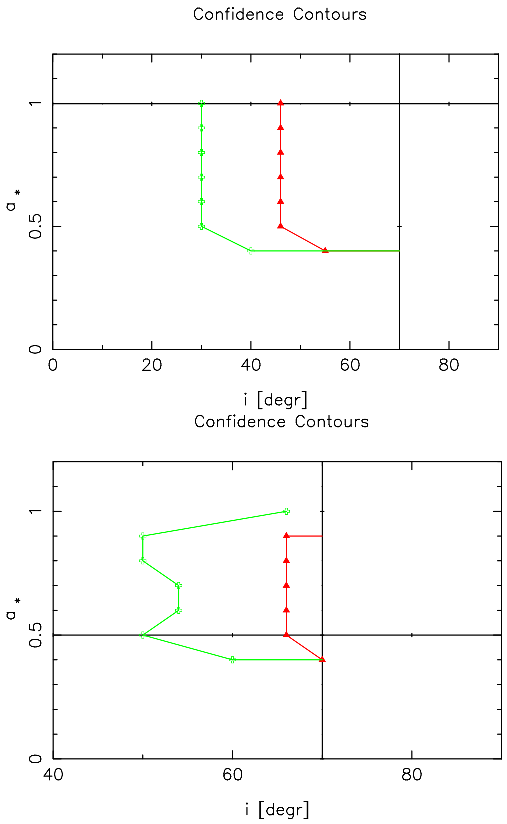

Figure 5.5: *The confidence contours for the constant* E*-vector (top) and the azimuthal magnetic field case (bottom) inferred from the 29/30 July 2005 data. The red (green) line is chosen such that the projection onto one of the parameter axes gives the* 1σ *(*3σ*) limit for this parameter. The respective* χ^2*-minimum is marked by the big cross. Note the different scales on the abscissae.*

5.5.2 The 2006 data

The fit with the least reduced-χ^2 value is shown in Fig. 5.6. A dimensionless spin parameter of $a_\star \approx 1$ and an inclination of $i \approx 58°$ give the best solution. Only the time interval $\leq 30\,\mathrm{min}$ was fitted because the spot emission disappears afterwards. The magnetic field corresponds to the constant E-vector scenario, which gives better fits than the azimuthal-field case. It is also interesting that the best-fit values for the intrinsic polarization degree of the disk/ring and the spot are the same ($\sim 17\%$). This is a profound difference to the data presented by Eckart et al. (2006b, see last section) where the spot was intrinsically highly polarized ($\sim 60\%$), while the disk was unpolarized ($\sim 5\%$).

As noted in the last section, a property of the model is a relatively weak dependence on the spin parameter. Figure 5.7 (top) shows the confidence contours for the constant E-Vector case within the $a_\star$-i-plane. The spin parameter can only be constrained to the region $a_\star \gtrsim 0.5$ on a 3σ level. Note that the observed timescale of roughly 15 min means that the spot is inside the least stable orbit, i.e. freely falling, for $a_\star \lesssim 0.6$. The inclination is $i > 20°$ on a 3σ level. The confidence contours for the azimuthal magnetic field are shown in Fig. 5.7 (bottom). The minimum χ^2 value here is at 1.2 higher than in the upper case, indicating a worse fit. The inclination can be constrained to $i \geq 55°$ on a 3σ level.

Our results from 2006 agree very well with the ones from 2005, where we found least reduced-χ^2-values for high spin parameters ($a_\star \approx 1$) and high inclinations ($i \approx 70°$), but with the same characteristic of a weak dependence, see blue dashed lines in Fig. 5.7. To progress in the description of the Sgr A* system, bright, strongly polarized sub-flares and a faint, low-polarized disk emission have to be observed. Accurate data of this type not only could give tighter constraints on the inclination and the spin parameter but also test the Kerr metric qualitatively. Due to slightly different observed frequencies of the different epochs, the hot spot has must have orbited on slightly different orbits. However, this should lead to the same spin parameter, as the mass of the BH is not expected to change significantly.

Although it would actually be difficult to explain why a single blob survives that long in a place where shearing is enormous, the repeated observation of 16–20 min separation among individual sub-flares justifies our assumption that assigns the same confined region to different peaks (see Section 5.2). This empirical indication can be taken as a constraint that needs to be imposed on theoretical models for the origin and confinement of blobs and the onset of flares in Sgr A*.

The observation of QPOs seems to favor the orbiting spot model instead of an adiabatically expanding plasma blob, a model that is also proposed

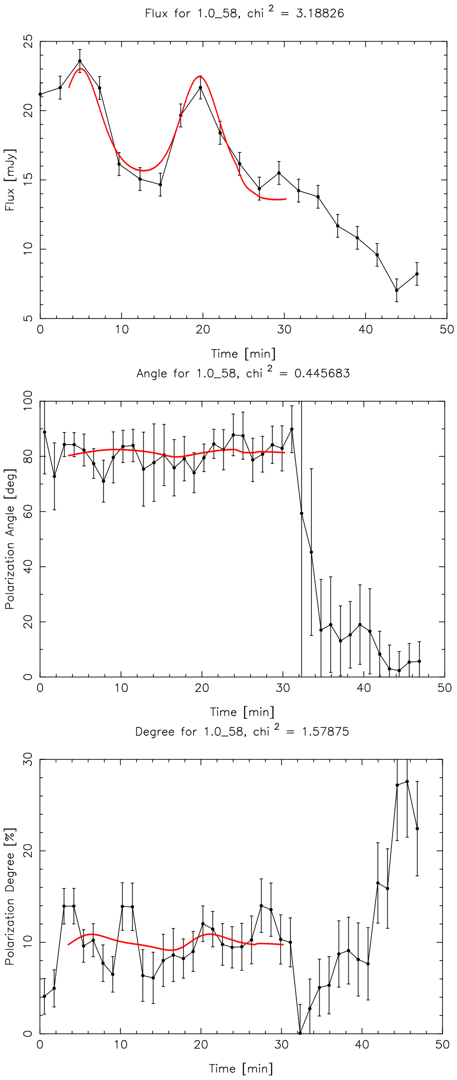

Figure 5.6: *The data from 31 May/1 June 2006 (see Fig. 3.2): the best fit solution (in red) for the constant E-vector case. Shown is the flux (top), the polarization angle (middle), and the degree of linear polarization (bottom). The parameters of the fit are $i = 58°$, $a_\star \approx 1$. The spot is orbiting at a radius $r = 4\,GM/c^2$. The disk/ring and the spot both have an intrinsic polarization degree of $\sim 17\%$. The reduced-χ^2 values for each fit are indicated above each graph.*

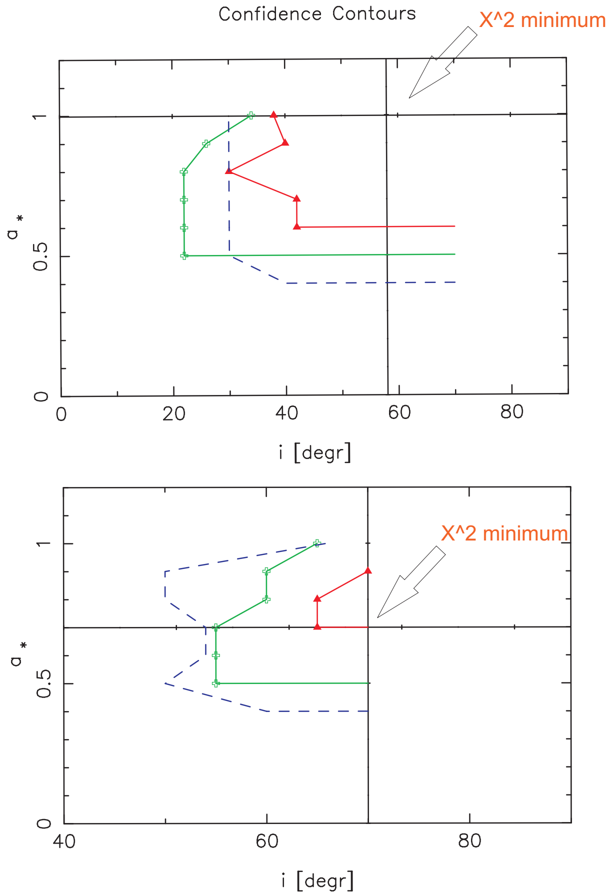

Figure 5.7: *The data from 31 May/1 June 2006 (Fig. 3.2): confidence contours for the constant E-Vector case (top) and the azimuthal magnetic field (bottom). The red (green) lines are chosen such that the projection onto one of the parameter axes gives the 1σ (3σ) limit for this parameter. The blue dashed lines indicate the 3σ contour for the 2005 data from the last section. The* χ^2*-minimum for the 2006 data is marked by the big cross. The* χ^2*-minimum of the 2005 epoch lies at* $a_\star = 1$, $i = 70°$ *(top) and* $a_\star = 0.5$, $i = 70°$ *(bottom). Our analysis is limited to* $i \lessapprox 70°$*, see the discussion of higher order images in Section 5.4.*

to explain the NIR flares from Sgr A* (Yusef-Zadeh et al., 2006; Eckart et al., 2006a). Such a model of relativistic plasma clouds expanding in a cone-jet geometry combined with suitable instabilities within the jet can also account for the flares and sub-flares of Sgr A*. In fact, the inclusion of both models offers a possibility of linking the NIR/X-ray activity to the sub-mm/radio regime: a plasma blob that is orbiting very close to the BH horizon (as described above) and then adiabatically expanding along a short jet-like geometry or within its orbit may explain the observed variability of Sgr A* across all wavelengths (Yusef-Zadeh et al., 2006; Eckart et al., 2006a).

Chapter 6

On the orientation of the Sgr A* system

In this chapter the fits to the 2006 data (introduced in Chapter 3 and modeled in the last chapter) are evaluated such that the three dimensional orientation of the Sgr A* system can be constrained. The results of this chapter have been published in Meyer et al. (2007).

6.1 Introduction

In this thesis we focus on polarimetric measurements of Sgr A* in the NIR and their interpretation in terms of the orbiting spot model, i.e. Keplerian motion in strong gravity is adopted as the cause for the sub-flares. As was shown in the previous chapter, the orbiting blob model can be tested (and perhaps rejected), although the task cannot be achieved now, given the insufficient quality of data available at present. In principle, constraints can be imposed on the model by tracking all four Stokes parameters and comparing their time evolution against the model. It is known that general relativity should imprint specific features in the time evolution of a polarized signal when a blob orbits near to a Black Hole (which is what we suggest here); the direction of the polarization vector should wobble within a range determined by the distance of the blob from the hole and the viewing angle of the observer (e.g. Connors et al., 1980, see also Chapter 4 and 5). Here, we discuss in particular the constraints that this modeling sets on the position angle of the normal to the equatorial plane of the spinning BH.

In the next two sections we first report so far unpublished polarimetric data of Sgr A* from 2003 that show that the mean polarization angle fluctuated only slightly for at least four years. Afterwards, this preferred direction is interpreted within the blob model.

6.2 The data and their reduction

The data we present here are polarimetric observations of Sgr A* at 2.2 μm from October 2003[1]. They have not been published before and are important to identify a favored orientation of the Sgr A* system. They have been taken with the near-infrared camera and adaptive optics system NACO at ESO's Very Large Telescope (VLT) in combination with a wire-grid. The observations have been conducted in such a way that after ~ 5 min the wire-grid has been rotated. While it is now clear (Genzel et al., 2003a; Eckart et al., 2006b) that this time resolution is too low due to the high variability of Sgr A* in the NIR, nevertheless a mean polarization angle can be inferred. The data are of very high quality and show an exceptionally bright flare.

We carried out standard reduction techniques, i.e. sky subtraction, flat fielding and bad pixel correction. The point spread function was extracted on each individual image (Diolaiti et al., 2000) and then used for a Lucy-Richard deconvolution. After restoration with a Gaussian beam, aperture photometry on the diffraction limited images for individual sources with known flux and Sgr A* was done. For the extinction correction we assumed $A_K = 2.8\,\mathrm{mag}$. Estimates of uncertainties were obtained from the standard deviation of fluxes from nearby constant sources. The calibration was per-

---

[1] They are freely available on the ESO archive, program 072.B-0285(A)

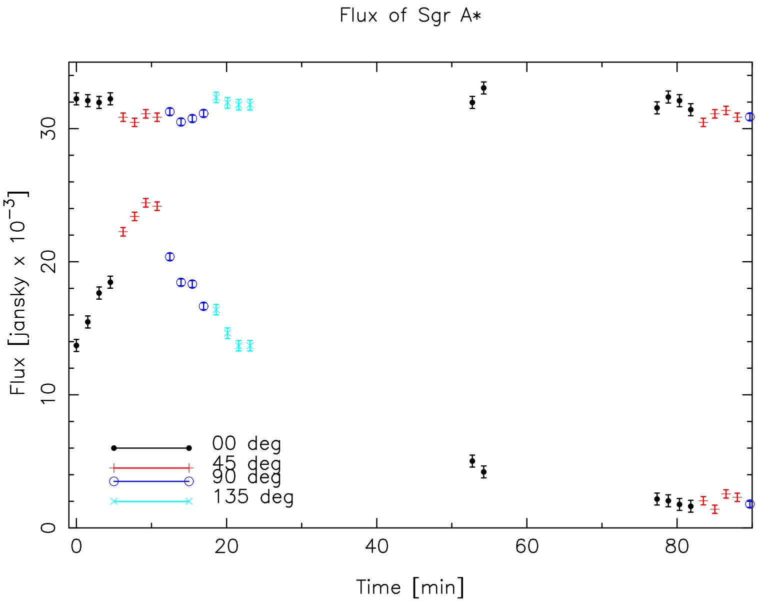

Figure 6.1: *Dereddened flux of Sgr A* and the constant reference star S2 (shifted 15 mJy upward for better comparison). Note that the duration of the single sub-flare is ∼ 20 min. The flux for each channel is calibrated such that it matches the total flux, i.e. each Stokes parameter is individually calibrated to the total flux of the references sources and not the sum of two orthogonal angles.*

formed using the overall interstellar polarization of all sources in the field, which is 4% at 25° (Eckart et al., 1995; Ott et al., 1999).

The dereddened flux of Sgr A* and of a nearby constant star is shown in Figure 6.1. The flux was calibrated such that each angle seperately matched the total flux of known sources. That means that actually Figure 6.1 shows approximately twice the flux for each angle. The first gap between ∼ 25 − 50 min is due to sky observations, the reason for the second gap is not traceable. The observations started exactly at the base of the peak.

6.3 The mean polarization angle

Figure 6.1 shows the high variability of Sgr A* with a very short rise and fall timescale consistent with previous observations. From these observations (Genzel et al., 2003a; Eckart et al., 2006b; Meyer et al., 2006a; Trippe et al., 2007, and Chapter 3) the following phenomenology of K-band flares has emerged: the first component is a broad underlying flare that lasts 50-120 min. The second component is sub-flares that are superimposed on the broad flare and show a constant seperation of $17 \pm 3\,$min. Having this context in mind and regarding the incompleteness of the data here, the single peak seen in the lightcurve in Figure 6.1 may be interpreted as one sub-flare superimposed on an underlying flare. Note that although only one possible sub-flare can be seen, its duration is ~20 min and therefore exactly what is expected from previous observations that showed suggestive QPO activity.

The polarimetric observing technique that was chosen for these observations here is certainly unsuitable as is known by now. The high variability demands the simultaneous measurement of all four position angles of the electric field vector. However, a shape of the sub-flare can be assumed and fitted to the data to allow a statement on the polarization angle and degree. Here, we approximate the sub-flare by a Lorentz profile of the form

$$f(x) = \frac{s}{s^2 + (x-t)^2}, \qquad s > 0, \quad -\infty < t < \infty.$$

The choice of a Lorentzian to fit this part of the lightcurve is of course not unambigous. This clearly brings some uncertainty to the inferred polarization properties. Figure 6.2 shows fits of a Lorentzian to each polarization angle.

The polarimetric observations of Sgr A* from 2004 – 2006 (Chapter 3 and Eckart et al., 2006b; Meyer et al., 2006a; Trippe et al., 2007) have shown that the degree of linear polarization and the polarization angle vary during a flare. The angle wobbles around a mean value during the high flux phase and then goes to different values in the decaying part of the flare (it is important to keep in mind that Sgr A* is at $2.2\mu m$ only detectable in its 'flaring state' so that nothing is known about the polarization properties in

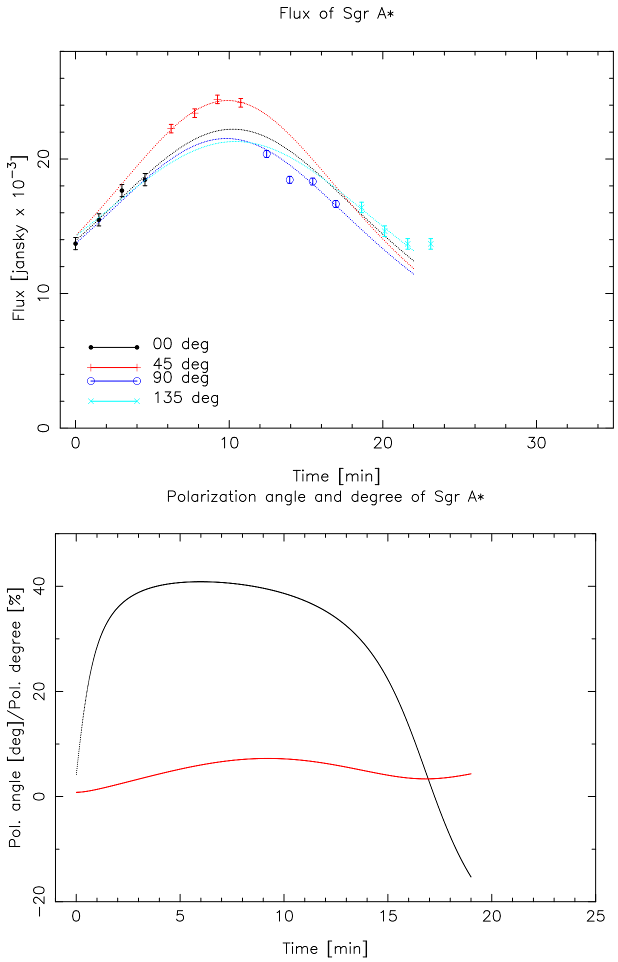

Figure 6.2: *Fits of a Lorentz profile to each channel of Figure 6.1 (upper panel). With this approximate behavior, the polarization angle and degree of linear polarization can be inferred. They are shown in the insert in the lower panel. The polarization angle is represented by the black line, the polarization degree is the red line.*

its low flux phase). The lower panel of Figure 6.2 shows that the Lorentz profile fits reproduce this behavior from previous observations qualitatively. The mean angle can be read off to be ∼ 40° (east of north).

Eckart et al. (2006b) report a mean angle of 60° ± 20° for observations in 2004 and 2005. While this is within the range inferred here, Meyer et al. (2006a) and Trippe et al. (2007) arrive at a mean angle of 80° ± 10° and 80° ± 25°, respectively, for the 2006 observing run. Concerning the uncertaintiy of the procedure adopted here, a conclusion that suggests itself is that the mean polarization angle of Sgr A* changed only slightly during the past four years. This is especially true if one takes into account that a strict stability of the mean polarisation appears to be rather unphysical. Small fluctuations in the magnetic field configuration and/or a precession of the inner accretion disk seem likely. In this regard, our conclusion that the roughly constant mean polarisation points to a preferred position of the Sgr A* system seems reasonable.

6.4 The three dimensional orientation of the Sgr A* system

The existence of a favored polarization angle allows to investigate the orientation of the Sgr A* system on the sky. Here, we want to study it within the orbiting blob model. Meyer et al. (2006a,b, see also Chapter 5) calculated polarimetric lightcurves from an orbiting spot (here we use spot and blob interchangeably) around Sgr A* and compared them to observations. This showed that this simple model, in which general relativistic effects on the radiation of a somehow confined, locally heated region plays the major role, leads to very good fits of the measurements. More precisely, in this model the sub-flares are due to a blob on a relativistic orbit around the MBH, while an underlying ring accounts for the broad overall flare. Relativistic effects like beaming, lensing, and change of polarization angle imprint on the emitted intrinsic radiation (e.g. Dovciak et al., 2004; Connors & Stark, 1977; Hollywood & Melia, 1997; Bromley et al., 2001; Falcke et al., 2000; Broderick & Loeb, 2005, 2006; Schnittman, 2005). In our model we assume that the variability in the polarization angle and the polarization degree are only due to the relativistic effects. As the emitted radiation of Sgr A* is synchrotron radiation (emitted in the disk corona), we assumed two different magnetic field configurations to fit the light curves with our model. The first is analogous to a sunspot and results in a constant E-vector perpendicular to the disk. The second configuration is a global azimuthal magnetic field that leads to a rotation of the E-vector along the orbit. With this model at hand, observed polarimetric lightcurves can be fitted to investigate the parameters of the Sgr A* system. The inclination angle, the dimensionless spin parameter $a_\star$, the brightness excess of the spot with respect to the disk, the initial phase of the spot on the orbit, the orientation of the equatorial plane on the sky, and the polarization degree of the disk and the spot are the free parameters. In Chapter 5, we focused on the viewing angle and the spin parameter of Sgr A*. In this chapter, we extend the discussion to the position angle of the system, i.e. the angle of the equatorial plane normal.

Figure 6.3 shows the $1\sigma-$ and $3\sigma-$confidence contours in the position angle (θ) – inclination angle (i) plane. The contours are results of the fits to the 2006 data presented in Chapter 5. The magnetic field configuration corresponds to the sunspot case. The contours have been calculated such that on each point in the $\theta - i$ plane the χ^2-minimum with respect to the other free parameters has been taken. The only exception is the dimensionless spin parameter $a_\star$ which has been fixed to $a_\star = 0.6$ throughout the calculations. The overall χ^2-minimum lies then at $\theta = 105°$, $i = 55°$ (marked with the black dot). As the contours show, this minimum is not unambigous, but it is nevertheless noteworthy that the formal χ^2-minimum coincides exactly with the finding of Markoff et al. (2007). In their paper, they fitted spectral and morphological properties of Sgr A* within the jet model. They also arrive at a position angle of 105° (east of north) for the jet axis together with an almost edge on viewing angle. The inclination angle in our work (Figure 6.3) may not be strict edge-on, but it has the trend to be. Also note that our approach can only cover the region $i \lessapprox 70°$, see discussion in Section 5.4. Furthermore, Muno et al. (2007) and Eckart et al. (2006b) present X-ray and NIR data of one long, narrow feature of synchrotron-emitting particles that point toward Sgr A* and may be identified as a jet. The angle of this jet-like feature on the sky is close to the 105° inferred here and thereby supports our finding.

It is interesting that different models and methods seem to converge to a viewing angle which is close to edge-on. Not only Markoff et al. (2007) and Meyer et al. (2006a) but also Falanga et al. (2007) and Huang et al. (2007) find such a configuration. Using the Rossby wave instability model (Tagger & Melia, 2006), Falanga et al. (2007) arrive at an inclination angle of $i \approx 77°$. Huang et al. (2007) noted that large inclination angles are

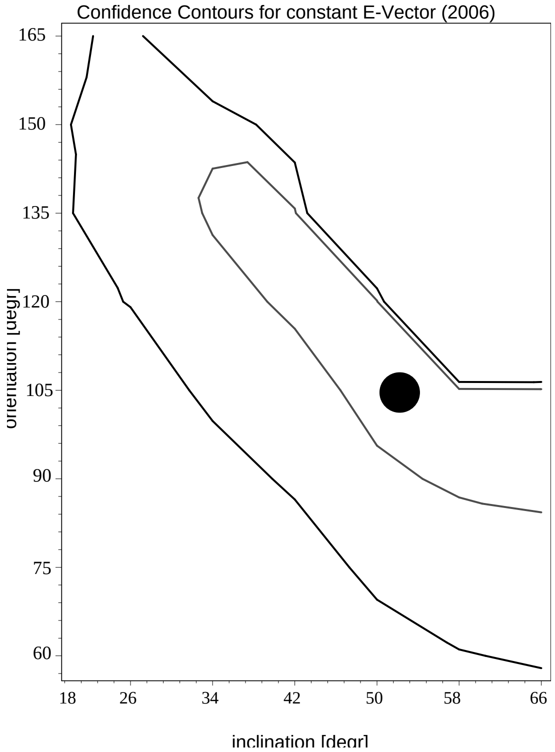

Figure 6.3: *$1\sigma-$ and $3\sigma-$confidence contours calculated from fits to the 31 May/1 June 2006 data (see Fig. 3.2 and Fig. 5.6). The assumed magnetic field configuration corresponds to the sun spot scenario. The vertical axis shows the position angle of the normal to the equatorial plane of the black hole on the sky (east of north). The horizontal axis shows the viewing angle ($0°$: face-on). The χ^2-minimum is represented by the black dot.*

preferred when a radiatively inefficient accretion flow model is coupled to a ray tracing algorithm and compared to recent VLBI size measurements. Taking the high inclination for granted, Figure 6.3 shows that our model predicts a position angle of $\sim 60° - 108°$. This quite broad range includes the result from Markoff et al. (2007) and Muno et al. (2007) as well as – at least in the 3σ limit – Muzic et al. (2007). The latter work investigated the proper motion of thin filaments at the Galactic center, which may be driven by some kind of collimated outflow. Sgr A* is identified as one possible source for such an outflow and if this is true, a preferred ejection direction of $\sim 60°$ is possible.

It is only useful to show the fits to the 2006 data here. This is for two reasons. First, the confidence contours of the 2005 and 2006 data are very similar and second, the 2006 data are of far better quality than the 2005 data. But it is of major importance to also note the shortcomings of our approach. First of all, the magnetic field geometry of the blob is completely unknown. As described above we used two simple approximations to describe the spot's field: (i) a sunspot like geometry in which the resulting $\vec{E}$-vector is always perpendicular to the equatorial plane, (ii) an azimuthal magnetic field, which is suggested by MHD simulations of magnetized accretion disks that often develop a toroidal component of the magnetic field. The former leads to better fits, that is why we have discussed it at length. But the latter case cannot be discarded. The corresponding confidence contours are shown in Figure 6.4. Unfortunately, its χ^2-minimum lies at rather small position angles, so the above conclusions get weakened. However, this minimum lies $\Delta\chi^2 \approx 5$ higher than in the sunspot scenario ($\chi^2 \approx 3$ and $\chi^2 \approx 8$, respectively; all values are reduced-χ^2 values). Although this is not a 3σ exclusion, it makes the sunspot scenario more likely. Another caveat concerns the unknown foreground polarization. Its value at the position of Sgr A* is important in the determination of the position angle. We had to assume that it is equal to the average value in the field. With these restrictions in mind, our work at least shows the consistency of independent findings with our model.

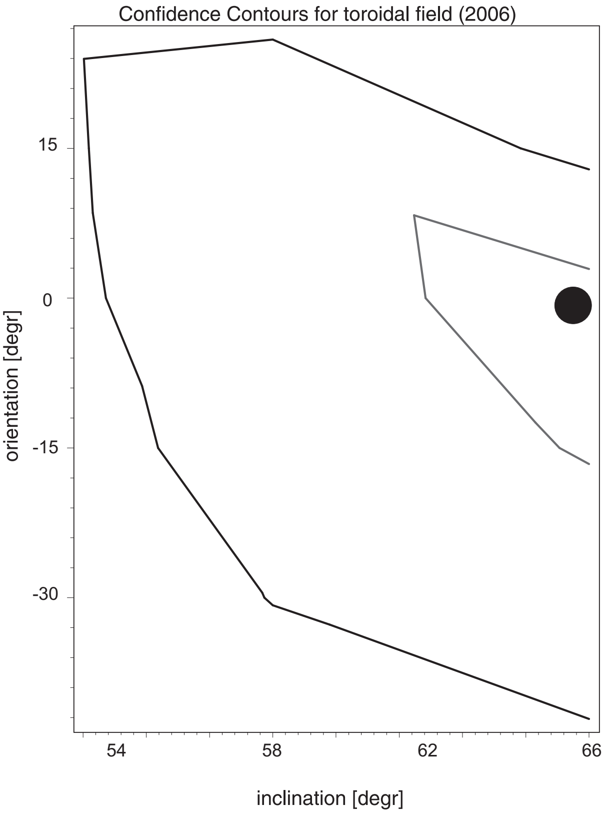

Figure 6.4: *$1\sigma-$ and $3\sigma-$confidence contours calculated from fits to the 2006 data (Fig. 3.2). An azimuthal magnetic field has been assumed. The vertical axis shows the position angle of the normal to the equatorial plane of the black hole on the sky (east of north). The horizontal axis shows the viewing angle ($0°$: face-on). The χ^2-minimum is represented by the black dot.*

Chapter 7

Summary and outlook

The center of the Milky Way is one of the most exciting astronomical targets because it represents the closest galactic nucleus accessible to observations. The source Sgr A* is with very high probability the electromagnetic counterpart of a supermassive Black Hole (BH). With Eddington luminosities of $L_{\mathrm{Edd}} = 10^{-9} - 10^{-10}$, Sgr A* is the most extreme sub-Eddington source known so far. It therefore serves as a template for sub-Eddington accretion onto a relativistic object. BHs play an outstanding role in theoretical physics as they belong to the intersection of thermodynamics, gravitational physics, and also fundamental quantum physics (for a review see e.g. Kiefer, 1999). The wealth of theoretical knowledge about BHs is unfortunately faced with little observational facts. Due to its vicinity Sgr A* plays an exceptional role in acquiring experimental data about the properties of a BH and its spacetime.

A characteristic feature of Sgr A* are the so-called ‘flares’, short bursts of increased radiation that last for about 60-100 min. These flares were first discovered at X-ray wavelengths, where the flux of Sgr A* may rise by factors up to $\sim$100 during such an event (e.g. Baganoff et al., 2003; Porquet et al., 2003; Eckart et al., 2004). At near-infrared (NIR) wavelengths the flares show very similar timescales, but the flux varies only by factors of ≤ 10 (Genzel et al., 2003a; Eckart et al., 2006a). Although the exact cause of the flares is still unclear, it is generally accepted that they are caused by synchrotron and synchrotron self-Compton emission processes within $\lessapprox$ 10 Schwarzschild radii (R_S) of the black hole (Eckart et al., 2006a; Gillessen et al., 2006). The non-thermal nature of the flares has recently been shown directly by detecting polarized NIR radiation from Sgr A* (Eckart et al., 2006b).

The most intriguing feature related to these flares are quasi-periodic oscillations (QPOs) with a period of 16-21 min, which have been detected in several of these events and are the topic under investigation in this thesis (see also Genzel et al., 2003a; Belanger et al., 2006; Eckart et al., 2006b). These periodicities may be related to the high-frequency quasi-periodic oscillations (HFQPO) observed in some black hole binaries. These HFQPOs scale inversely with the mass of the BH and are thought to be related to plasma in a relativistic flow within a few Schwarzschild radii of the black hole. Although their mechanism has still not been clearly understood, they appear to be promising tools in probing the space time around Black Holes (for a review of black hole binaries and HFQPOs, see Nowak & Lehr, 1998; McClintock et al., 2004). The QPOs observed in Sgr A* are similar to HFQPOs in the sense that they appear to fit into the mass-scaling relationship. However, the exact relation between the XRB HFQPOs and Sgr A* QPOs is not clear yet. In particular, XRB HFQPOs are observed at X-ray wavelengths, arise in thin accretion disks, and show amplitude modulations of just a few percent. Contrary to this, no stationary thin disk is thought to be present in Sgr A*, the QPOs are observed at NIR wavelengths, and they show a modulation of $> 50\%$.

However, it is important to note that these suggestive QPOs from Sgr A* have only been observed in a few cases, which has raised some doubts about their nature, particularly whether they may just be related to a red-noise-like process in the source.

This thesis showed that some near-infrared flares clearly are accompanied by sub-flares, i.e. flux peaks superimposed on the broader main flare, and that these sub-flares likely constitute a quasi-periodic structure. We derived that the ~ 18 min periodicity reported by (Genzel et al., 2003a) is on a 4.2σ level *not* due to red noise. Furthermore, also Eckart et al. (2006b) find an excess at 20 min in their periodogram of a flare from 2005. And, finally, the results from 2006 reported by Meyer et al. (2006a, see Fig. 3.2) again strongly support the existence of an 16-21 min QPO. As can be seen in Fig. 3.2, the high amplitude of the two sub-flares separated by 16 min makes red noise as the source of periodicity unlikely.

The timescale of the lightcurve variations of Sgr A* indicate that rapid orbital motion in strong gravity may be the cause for the quasi-periodicity. This suggests a model consisting of a locally heated and confined plasma blob which is in a relativistic orbit around Sgr A*. The timescale of 16-21 min means that this spot orbits close to the event horizon of the BH. There, relativistic effects are of major importance (e.g. Connors & Stark 1977, Broderick & Loeb 2006, Dovciak et al. 2004; Hollywood et al. 1995; Hollywood & Melia 1997). **We used recent and carried out new NIR polarimetric observations to show that the polarized flux variations from Sgr A* can very well be fitted within the plasma blob model, where the interplay of relativistic effects plays the main role. This fitting constrains the dimensionless spin paramter of the Kerr BH to regions $a_\star \gtrsim 0.5$ and the inclination of the accretion flow onto Sgr A* to $i \gtrsim 30°$ on a 3σ level.**

Furthermore, the mean polarization angle in the near-infrared was shown to be almost constant from 2003-2006, and the position angle of Sgr A* from this preferred direction in terms of the orbiting spot model was inferred. **For a high inclination angle the 3σ range for the position angle of a temporary disk around Sgr A* is derived to be** $\sim 60° - 108°$. This supports the findings of Markoff et al. (2007), and – less likely in terms of the χ^2 – Muzic et al. (2007) who arrived at position angles of $\sim 105°$ (see also Muno et al., 2007) and $\sim 60°$, respectively, with complementary methods. However, there are some caveats. The unknown magnetic field structure, the uncertain foreground polarization, and the lack of a clear understanding of the detailed hydrodynamics of the blob bring some ambiguity to our conclusions.

What does the future of GC research look like? Across all wavelengths, improvements in interferometry will allow to investigate Sgr A* at smallest angular scales and therefore to study directly the accretion flow and the spacetime in the vicinity of a SMBH. In the near-infrared, the adaptive optics assisted VLT interferometer (VLTI) instrument – GRAVITY – for precision narrow-angle astrometry and interferometric phase referenced imaging of faint objects is being planned (e.g. Paumard et al., 2005). Precision astrometry and phase-referenced interferometric imaging will realize the most advanced vision of optical/infrared interferometry with the VLT. The most ambitious science goal is to study motions within a few times the event horizon size of the Galactic center massive Black Hole and to test General Relativity in its strong field limit. The installation of the instrument at the VLTI is planned for 2012.

As we have seen throughout this thesis, recent evidence from multi-wavelengths studies and infrared polarimetry strongly suggests that the emitting region of Sgr A* in the NIR sometimes consists of a compact spot of hot plasma emitting synchrotron radiation. Of course, such a spot cannot remain static in the potential well of the BH, but its velocity must be comparable to the Keplerian circular velocity $v \sim (r/R_S)^{-1/2} \times 10\mu\text{as min}^{-1} \sim 5\mu\text{as min}^{-1}$. Therefore, measuring the 2D astrometry of flares with 10μas accuracy and a time resolution of a few minutes will not only allow us to determine the location of the flares with respect to the SMBH, but also their proper motions. Hence, GRAVITY should be able to determine the centroid motion of a hot spot orbiting around Sgr A*. Due to lensing and time delays the observed trajectory won't be circular. Using a ray tracing code such as KY (see Chapter 4), the expected path as seen on earth in a Kerr metric can be calculated (e.g. Broderick & Loeb, 2005). This will probe General Relativity in the strong field regime and – above all – verify or falsify the orbiting spot picture.

The mm/sub-mm regime offers another exciting prospect. At these frequencies the synchrotron emission appears to be optically thin, as inferred from the turnover in the spectrum. However, it is also the regime where the intrinsic source size becomes apparent over the scatter-broadening effects of the intervening screen (see Section 1.3.1). So, we might expect to see the black hole directly through the murky medium.

This idea of imaging the BH goes back to Falcke et al. (2000). What we can expect to see – at least in a steady, spherical accretion flow – is a depression of flux in the center, literally a black hole. This ‘shadow of the black hole’ arises because there is a closed curve on the sky plane that divides a region where photon geodesics intersect the horizon from a complementary region whose geodesics miss it. This apparent boundary of the BH has a radius of $\frac{3}{2}\sqrt{3}\,R_S$ for the Schwarzschild case $a_\star = 0$ (inferred from the value of the effective potential in the Schwarzschild metric at the photon radius $r = \frac{3}{2}R_S$, e.g. Falcke et al., 2000). Note that this boundary is much larger than the event horizon itself due to the strong bending of light.

The technical methods to achieve the necessary resolution to form these images directly are currently being developed for wavelengths shorter than $\sim 1.3\,\mathrm{mm}$ (e.g. Krichbaum et al., 2006). The challenge will be to push this technology toward sub-mm VLBI, where the coherence time is much shorter and the telescope performance deteriorates. Of equal importance will also be to establish mm-VLBI antennae on the southern hemisphere, because Sgr A* is at a declination of $-29°$. From an optimistic point of view, these experiments may be feasible within the next decade. Then, the dramatic effects of strong gravity will be directly visible.

Bibliography

Abramowicz, M. A., Kluzniak, W., Stuchlik, Z., Török, G. 2004, in "Proceedings of RAGtime 4/5 Workshops on black holes and neutron stars", edited by Hledik, S. ans Stuchlik, Z., Silesian University in Opava, p.1

Aitken, D. K., Greaves, J., Chrysostomou, A., et al., 2000, ApJL, 534, 173

Aschenbach, B., Grosso, N., Porquet, D., Predehl, P. 2004, A& A, 417, 71A

Aschenbach, B. 2004, A& A, 425, 1075A

Aschenbach, B. 2006, ChJAS, 6, 221

Baganoff, F. K., Bautz, M. W., Brandt, W. N., et al. 2001, Nature, 413, 45

Baganoff, F. K., Maeda, Y., Morris, M., et al. 2003, ApJ, 591, 891

Balbus, S. A., Hawley, J. F., 1991, ApJ, 376, 197

Balick, B., Brown, R. L., 1974, ApJ, 194, 265

Bardeen, J. M., Press, W. H., Teukolsky, S. A. 1972, ApJ, 178, 347

Bardeen, J. M., Petterson, J. A., 1975, ApJL, 195, 65L

Belanger, G., Terrier, R., De Jager, O., Goldwurm, A., Melia, F. 2006, submitted to ApJL; astro-ph/0604337

Benlloch, S., Wilms, J., Edelson, R., Yaqoob, T., Staubert, R. 2001, ApJ, 562, L121

Binney, J., Tremaine, S., 1987, "Galactic Dynamics", Princton University Press

Blandford, R. D., Begelman, M. C., 1999, MNRAS, 303L, 1

Bower, G. C., Wright, M. C. H., Falcke, H., Backer, D. C., 2001, ApJL, 555, 103

Bower, G. C., Wright, M. C. H., Falcke, H., Backer, D. C., 2003, ApJ, 588, 331

Bower, G. C., Falcke, H., Herrnstein, R. M., Zhao, J.-H., Goss, W. M., Backer, D. C., 2004, Science, 304, 704

Bower, G. C., Goss, W. M., Falcke, H., Backer, D. C., Lithwick, Y., 2006, ApJL, 648, 127

Bozza, V., Mancini, L. 2004, GReGr, 36, 435

Brandner, W., Rousset, G., Lenzen, R. et al., 2002, The Messenger, 107, 1

Broderick, A. E., Loeb, A. 2006, MNRAS, 367, 905

Broderick, A. E., Loeb, A. 2005, MNRAS, 363, 353

Bromley, B. C., Melia, F., Liu, S. 2001, ApJ, 555L, 83B

Bursa, M., Abramowicz, M. A., Karas, V., Kluźniak, W., 2004, ApJ, L45

Carroll, S., 2004, "Spacetime and Geometry – An introduction to General Relativity", Addison Wesley

Carter, B., 1968, Phys. Rev., 174, 1559

Chan, C., Liu, S., Fryer, C. S., et al. 2006, subm. to ApJ, astro-ph/0611269

Coker, R. F., Melia, F. 1997, ApJ, 488L, 149C

Connors, P. A., Stark, R. F., 1977, Nature, 269, 128

Connors, P. A.; Stark, R. F.; Piran, T., 1980, ApJ, 235, 224

Cunningham, C. T., 1975, ApJ, 202, 788

De Villiers, J., Hawley, J. F., Krolik, J. H. 2003, ApJ, 599, 1238

Diolaiti, E., Bendinelli, O., Bonaccini, D., et al. 2000, A&A Suppl., 147, 335

Dovciak, M., Karas, V., Yaqoob, T. 2004, ApJS, 153, 205

Dovciak, M., 2004, PhD-Thesis, Charles University, Prague

Eckart, A., Genzel, R., Hofmann, R., Sams, B. J., Tacconi-Garman, L. E. 1995, ApJ, 445L, 23

Eckart, A., Genzel, R., 1996, Nature, 383, 415

Eckart, A., Baganoff, F. K., Morris, M., et al. 2004, A&A, 427, 1

Eckart, A., Baganoff, F. K., Schödel, R., et al. 2006a, A&A, 450, 535

Eckart, A., Schödel, R., Meyer, L., et al. 2006b, A&A, 455, 1

Eckart, A., Schödel, R., Straubmeier, C., 2005, "The black hole at the center of the milky way", Imperial College Press, London

Eisenhauer, F., Genzel, R., Alexander, T., et al. 2005, ApJ, 628, 246

Falanga, M., Melia, F., Tagger, M., Goldwurm, A., Belanger, G. 2007, ApJL in press

Falcke, H., Melia, F., Agol, E. 2000, ApJ, 528L, 13F

Fried, D. L., 1966, Optical Society of America Journal, 56, 1372

Genzel, R., Schödel, R., Ott, T., et al. 2003a, Nature, 425, 934

Genzel, R., Schödel, R., Ott, T., et al. 2003b, ApJ, 594, 812

Ghez, A. M., Klein, B. L., Morris, M., Becklin, E. E. 1998, ApJ, 509, 678

Ghez, A. M., Morris, M., Becklin, E. E., Tanner, A., Kremenek, T., 2000, Nature, 407, 349

Ghez, A. M., Becklin, E., Duchene, G., et al., 2003a, ANS, 324, 527

Ghez, A. M., Duchêne, G., Matthews, K., et al., 2003b, ApJL, 586L, 127

Ghez, A. M., Wright, S. A., Matthews, K., et al., 2004, ApJ, 601, L159

Ghez, A. M., Salim, S., Hornstein, S. D., et al. 2005a, ApJ, 620, 744

Ghez, A. M., Hornstein, S. D., Lu, J. R., et al. 2005b, ApJ, 635, 1087G

Gillessen, S., Eisenhauer, F., Quataert, E., et al. 2006, ApJ, 640, L163

Hartle, J. B., 2003, "Gravity: an introduction to Einstein's general relativity", Addison Wesley

Herrnstein, R. M., Zhao, J.-H., Bower, G. C., Goss, W. M., 2004, AJ, 127, 3399

Hirose, S., Krolik, J. H., DeVilliers, J.-P., Hawley, J. F., 2004, ApJ, 606, 1083

Hollywood, J. M., Melia, F., Close, L. M., McCarthy, D. W. Jr., Dekeyser, T. A. 1995, ApJL, 448, 21

Hollywood, J. M., Melia, F. 1997, ApJS, 112, 423

Horák, J., Karas, V. 2006a, MNRAS, 365, 813

Horák, J., Karas, V. 2006b, PASJ, 58, 203

Hornstein, S. D., Matthews, K., Ghez, A. M., Lu, J. R., Morris, M., Becklin, E. E., Baganoff, F. K., Rafelski, M., 2006, JPhCS, 54, 399

Huang, L., Cai, M., Shen, Z., Yuan, F. 2007, MNRAS accepted, astro-ph/0703254

Kiefer, C., 1999, in "Classical and Quantum Black Holes", ed. by P. Fre, V. Gorini, G. Magli and U. Moschella, IOP Publishing, Bristol, p.19

Krabbe, A., Genzel, R., Eckart, A., et al., 1995, ApJL, 447, 95

Krichbaum, T. P., Graham, D. A., Bremer, M., Alef, W., Witzel, A., Zensus, J. A., Eckart, A., 2006, JPhCS, 54, 328

Krolik, J. H., Hawley, J. F. 2002, ApJ 573, 754

Liu, S., Melia, F. 2002, ApJL, 566, L77

Liu, S., Melia, F., Petrosian, V. 2006, ApJ, 636, 798

Loeb, A., Waxman, E., 2007, JCAP, 3, 11

Lourakis, M. I. A. 2004, levmar:Levenberg-Marquardt nonlinear least squares algorithms in C/C++, webpage: www.ics.forth.gr/∼lourakis/levmar/

Lu, J. R., Ghez, A. M., Hornstein, S. D., et al. 2006, JPhCS, 54, 279

Lucy, L. B., 1974, AJ, 19, 745

Luminet, J.-P., 1979, A&A, 75, 228

Machida, M., Matsumoto, R. 2003, ApJ, 585, 429

Markoff, S., Falcke, H., Yuan, F., Biermann, P. L. 2001, A&A, 379, L13

Markoff, S., Bower, G., Falcke, H. 2007, 2007, MNRAS, 379, 1519

Marrone, D. P., Moran, J. M., Zhao, J.-H., Rao, R., 2006a, ApJ, 640, 308

Marrone, D. P., Moran, J. M., Zhao, J.-H., Rao, R., 2006b, JPhCS, 54, 354

Marrone, D. P., Moran, J. M., Zhao, J.-H., Rao, R., 2007, ApJ, 654, L57

Martins, F., Genzel, R., Hillier, D. J., et al. 2007, A&A, 468, 233

Mashhoon, B., 1973, Phys. Rev. D, 7, 2807

Mauerhan, J. C., Morris, M., Walter, F., Baganoff, F. K. 2005, ApJL, 623, 25

McClintock, J. E., Remillard, R. A. 2004, Chapter 4 in "Compact Stellar X-Ray Sources", eds. Lewin, W. H. G., van der Klis, M., Cambridge University Press.

Melia, F., 2007, The Galactic Supermassive Black Hole, Princeton Univerity Press, Princeton

Meyer, F., 1984, A&A, 131, 303

Meyer L., Schödel R., Eckart A., Karas, V., Dovciak, M., Duschl, W. J., 2006a, A&A, 458, L25

Meyer L., Eckart A., Schödel R., Duschl, W. J., Muzic, K., Dovciak, M., Karas, V., 2006b, A&A, 460, 15

Meyer, L., Schoedel, R., Eckart, A., Duschl, W. J., Karas, V., Dovciak, M., 2007, A&A, 473, 707

Morris, M., 1993, ApJ, 408, 496

Moscibrodzka, M., Das, T. K., Czerny, B. 2006, MNRAS, in press (astro-ph/0604516)

Müller, A. 2007, arXiv:astro-ph/0701228

Muno, M. P., Baganoff, F. K., Brandt, W. N., Morris, M. R., Starck, J.-L., 2007, submitted to ApJ, arXiv:0707.1907

Muzic, K., Eckart, A., Schödel, R., Meyer, L., Zensus, A. 2007, A&A, 469, 993

Nowak, M., Lehr, D., 1998, in "Theory of Black Hole Accretion Disks", edited by Marek A. Abramowicz, Gunnlaugur Bjornsson, and James E. Pringle, Cambridge University Press, p.233

Narayan, R., Yi, I., 1994, ApJL, 428, 13

Ott, T., Eckart, A., Genzel, R., 1999, ApJ, 523, 248

Ott, T., 2002, PhD thesis, Ludwig-Maximilians-Universität München

Paumard, T., Perrin, G., Eckart, A., et al. 2005, Astron. Nachr., 326, 568

Paumard, T., Genzel, R., Martins, F., et al. 2006, ApJ, 643, 1011

Pineault, S. 1981, ApJ, 246, 612

Porquet, D., Predehl, P., Aschenbach, B., et al. 2003, A&A, 407, L17

Rauch, K. P., Blandford, R. D., 1994, ApJ, 381, 39

Reid, M. J., Readhead, A. C. S., Vermeulen, R. C., Treuhaft, R. N., 1999, ApJ, 524, 816

Reid, M. J., Brunthaler, A., 2004, ApJ, 616, 872

Schnittman, J. D., 2005, ApJ, 621, 940

Tagger, M., Melia, F. 2006, ApJ, 636L, 33T

Timmer, J., König, M. 1995, A&A, 300, 707

Schödel, R., Ott, T., Genzel, R., et al. 2002, Nature, 419, 694

Schödel, R., Genzel, R., Ott, T., et al. 2003, ApJ, 596, 1015

Schödel, R., Eckart, A., Alexander, T., et al. 2007, A&A, 469, 125

Serkowski, K., 1962, in "Advances in Astronomy and Astrophysics", Edited by Zdentek Kopal, Academic Press, p.290

Shakura, N. I., Sunyaev, R. A. 1973, A&A, 24, 337

Stolovy, S., Ramirez, S., Arendt, R. G., et al. 2006, JPhCS, 54, 176

Straumann, N., 2004, "General relativity with applications to astrophysics", Springer Texts and monographs in physics, Berlin

Trippe, S., Paumard, T., Gillessen, S., et al. 2007, MNRAS, 375, 764

Vaughan, S. 2005, A&A, 431, 391

Viergutz, S. U., 1993, A&A, 272, 355

Wald, R. M., 1984, "General Relativity", University of Chicago Press

Wald, R. M., 1997, "Gravitational Collapse and Cosmic Censorship", eprint arXiv:gr-qc/9710068

Walker, M., Penrose, R. 1970, Commun. Math. Phys., 18, 265

Yuan, F., Quataert, E., Narayan, R. 2003, ApJ, 598, 301

Yuan, F., Quataert, E., Narayan, R. 2004, ApJ, 606, 894

Yusef-Zadeh, F., Roberts, D., Wardle, M., Heinke, C. O., Bower, G. C., 2006, ApJ, 650, 189

Zhao, J.-H., Goss, W. M. 1998, ApJL, 499, L163

Zhao, J.-H., Young, K. H., Herrnstein, R. M., et al. 2003, ApJL, 586, 29

Zhao, J.-H., Herrnstein, R. M., Bower, G. C., Goss, W. M., Liu, S. M., 2004, ApJL, 603, 85

List of Abbreviations

A_K	extinction in K-band
ADAF	Advection Dominated Accretion Flow
AGB	Asymptotic Giant Branch
AGN	Active Galactic Nucleus
AO	Adaptive Optics
BH	Black Hole
CND	Circum Nuclear Cisk
ESO	European Southern Observatory
FWHM	Full Width at Half Maximum
GC	Galactic Center
GR	General Relativity
HFQPO	High-frequency Quasi-Periodic Oscillation
ISCO	Innermost Stable Circular Orbit, also: marginally stable orbit
K-band	$1.9 - 2.4\,\mu$m wavelength range
Keck	W. M. Keck Observatory – two 10m telescopes
KY	Ray tracing code by Dovciak et al. (2004)
L'-band	$3.48 - 4.08\,\mu$m wavelength range
MBH	Massive Black Hole
MHD	Magneto-Hydrodynamics
NACO	NAOS/CONICA adaptive optics device/near-infrared camera at the VLT
NIR	Near-infrared

PSF	Point Spread Function
QPO	Quasi-Periodic Oscillation
RIAF	Radiatively Inefficient Accretion Flow
$R_S = 2\,GM/c^2$	Schwarzschild Radius
$r_g = GM/c^2$	Gravitational Radius
Sgr A*	Sagittarius A*
SMBH	Supermassive Black Hole
VLBI	Very Long Baseline Interferometry
VLT	Very Large Telescope
XRB	X-ray binary

List of Figures

1.1 Galactic center overview 12

1.2 GC at 6cm 13

1.3 GC at 13mm 14

1.4 GC in the NIR 15

1.5 The central cusp of stars 18

1.6 Keplerian orbits 19

1.7 Enclosed mass 20

1.8 Angular size of Sgr A* 22

1.9 Spectrum of Sgr A* 25

1.10 NIR flare 28

1.11 Simultaneous X-ray/NIR observations 30

2.1 The seeing phenomenon 34

2.2 Adaptive optics 36

2.3 The VLT 38

2.4 VLT mirror 39

2.5 Deconvolution 43

3.1 QPO significance 48

3.2 Flare from 31 May 2006 52

3.3 Periodogram 31 May 2006 53

3.4 Flare 29 July 2005 55

3.5 Periodogram 29 July 2005 56

4.1 Horizons around a black hole 64

5.1 Orbiting spot 77

5.2 Magnetic fields 79

5.3 Best fit 2005 83

5.4 Best fit 2005, azimuthal magnetic field 84

5.5 Confidence contours 2005 85

5.6 Best fit 2006 87

5.7 Confidence contours 2006 88

6.1 Flare October 2003 93

6.2 The mean angle 95

6.3 The orientation of Sgr A* 98

6.4 The orientation of Sgr A*, azimuthal field 100

Acknowledgements

No effort is undertaken in vacuum. I am extremely grateful to all the people that supported me directly or indirectly during my studies. Above all, I want to thank my supervisor Prof. Dr. Eckart and my co-referee Prof. Dr. Kiefer for putting me on this exciting subject and supporting me without restrictions throughout my thesis. Many thanks also to Prof. Dr. Tezkan for taking the chair of the examination board. Also, the collaboration with Prof. Dr. Duschl from Kiel, Dr. Karas and Dr. Dovciak from Prague was immensely fruitful. It was a very exciting and enjoyable experience to work together with such established scientists.

A particular thank you also belongs to Dr. Rainer Schödel, my co-supervisor, office, beer and foosball mate. Now I know that pain really is good for me. I am very happy that fate also brought my fellow student Marc Hitschfeld from Aachen to Cologne. Without the daily coffee and chat life would have been much harder.

I am very grateful for the nice working atmosphere within our group. Just to name a few personally, Jens Zuther and Sebastian Fischer always lost at the football table just to cheer me up, Thomas Bertram and Dr. Christian Straubmeier kindly helped me with every easy and not-so-easy computer problem, Koraljka Muzic was the perfect travel companion, Serife Sanli had answers to really every philosophical and administrative question, Gunther Witzel is the perfect fireman for urgent scientific work, Christoph Olczak, Bettina&Uwe Lindhorst, and Prof. Dr. Susanne Pfalzner are the best conversational partners during a not-so-yummy mensa lunch, Devaky Kunneriath and Mohammad Zamaninasab have the unique skill to turn a rainy trip to Sauerland into a very nice and funny event.

The work could not have been done without the financial support by the University of Cologne and the International Max Planck Research school at the Universities of Bonn and Cologne. It was a pleasure and honor to be a member of IMPRS, and the retreats with my fellows IMPRS students have been great – I really suck at Powerpoint Karaoke, though.

Last but not least, the warmest thank you is reserved for my family and friends, and in praticular my significant other Julia. She, her parents, my siblings, and my parents gave me the necessary support and drive to accomplish this work. They can take credit for what has been achieved.

Erklärung

Ich versichere, daß ich die von mir vorgelegte Dissertation selbständig angefertigt, die benutzten Quellen und Hilfsmittel vollständig angegeben und die Stellen der Arbeit – einschließlich Tabellen, Karten und Abbildungen –, die anderen Werken im Wortlaut oder dem Sinn nach entnommen sind, in jedem Einzelfall als Entlehnung kenntlich gemacht habe; daß diese Dissertation noch keiner anderen Fakultät oder Universität zur Prüfung vorgelegen hat; daß sie – abgesehen von unten angegebenen Teilpublikationen – noch nicht veröffentlicht worden ist sowie, daß ich eine solche Veröffentlichung vor Abschluß des Promotionsverfahrens nicht vornehmen werde.

Die Bestimmungen dieser Promotionsordnung sind mir bekannt. Die von mir vorgelegte Dissertation ist von Prof. Dr. Eckart betreut worden.

Köln,

Teilpublikationen

Meyer, L.; Schödel, R.; Eckart, A.; Duschl, W. J.; Karas, V.; Dovciak, M.: ,,On the orientation of the Sagittarius A* system", 2007, Astronomy and Astrophysics, Volume 473, Issue 3, pp.707-710

Meyer, L.; Eckart, A.; Schödel, R.; Dovciak, M.; Karas, V.; Duschl, W. J.: ,,Using the orbiting spot model to give constrains on the parameters of the supermassive black hole in the Galactic center", 2007, Proceedings of the IAU symposium No. 238, Cambridge University Press, pp.407-408

Meyer, L.; Eckart, A.; Schödel, R.; Duschl, W. J.; Dovciak, M.; Karas, V.: ,,A two component hot spot/ring model for the NIR flares of Sagittarius A*", 2006, Journal of Physics: Conference Series, Volume 54, Issue 1, pp. 443-447

Meyer, L.; Eckart, A.; Schödel, R.; Duschl, W. J.; Muzic, K.; Dovciak, M.; Karas, V.: ,,Near-infrared polarimetry setting constraints on the orbiting spot model for Sgr A* flares", 2006, Astronomy and Astrophysics, Volume 460, Issue 1, pp.15-21

Meyer, L.; Schödel, R.; Eckart, A.; Karas, V.; Dovciak, M.; Duschl, W. J.: ,,K-band polarimetry of an Sgr A* flare with a clear sub-flare structure", 2006, Astronomy and Astrophysics, Volume 458, Issue 2, pp.L25-L28

Eckart, A.; Schödel, R.; **Meyer, L.**; Trippe, S.; Ott, T.; Genzel, R.: ,,Polarimetry of near-infrared flares from Sagittarius A*", 2006, Astronomy and Astrophysics, Volume 455, Issue 1, pp.1-10

Weitere Publikationen

Muzic, K.; Eckart, A.; Schödel, R.; **Meyer, L.**; Zensus, A.: ,,Proper motions of the thin filaments at the Galactic Center", 2007, Astronomy and Astrophysics, Volume 469, Issue 3, pp.993-100

Schödel, R.; Eckart, A.; Alexander, T.; Merritt, D.; Genzel, R.; Sternberg, A.; **Meyer, L.**; Kul, F.; Moultaka, J.; Ott, T.; Straubmeier, C.: ,,The structure of the nuclear stellar cluster of the Milky Way", 2007, Astronomy and Astrophysics, Volume 469, Issue 1, pp.125-146

Schödel, R.; Eckart, A.; Muzic, K.; **Meyer, L.**; Viehmann, T.; Bower, G. C.: ,,The possibility of detecting Sagittarius A* at 8.6 μm from sensitive imaging of the Galactic center", 2007, Astronomy and Astrophysics, Volume 462, Issue 1, pp.L1-L4

Eckart, A.; Schödel, R.; **Meyer, L.**; Straubmeier, C.; Dovciak, M.; Karas, V.; Baganoff, F. K.; Morris, M.: ,,Variable and polarized emission from Sgr A*", 2006, Proceedings of the IAU symposium No. 238, in press

Eckart, A.; Schödel, R.; **Meyer, L.**; Trippe, S.; Ott, T.; Genzel, R.; Muzic, K.; Moultaka, J.; Straubmeier, C.; Baganoff, F. K.; Morris, M.; Bower, G. C.: ,,Multi-wavelength and polarimetric observations of Sagittarius A*", 2006, Journal of Physics: Conference Series, Volume 54, Issue 1, pp. 391-398

Muzic, K.; Eckart, A.; Schödel, R.; **Meyer, L.**; Zensus, A.: ,,Thin filaments at the Galactic Center: identification and proper motions", 2006, Journal of Physics: Conference Series, Volume 54, Issue 1, pp. 311-315

Eckart, A.; Schödel, R.; **Meyer, L.**; Muzic, K.; Pott, J.; Moultaka, J.; Straubmeier, C.; Dovciak, M.; Karas, V.; Genzel, R.; Ott, T.; Trippe, S.; Najarro, F.; Morris, M.; Baganoff, F.: ,,The Galactic Centre: The Flare Activity of Sgr A* and High-Resolution Explorations of Dusty Stars", 2006, The Messenger, Vol. 125, p.2

Eckart, A.; Schödel, R.; Straubmeier, C.; Bertram, T.; Pott, J.; Muzic, K.; **Meyer, L.**; Moultaka, J.; Viehmann, T.; Rost, S.; Herbst, T.: ,,Interferometric observations of the galactic center: LBT and VLTI", 2006, Advances in Stellar Interferometry. Edited by Monnier, John D.; Schöller, Markus; Danchi, William C.; Proceedings of the SPIE, Volume 6268, pp. 62681

Eckart, A.; Schödel, R.; **Meyer, L.**; Trippe, S.; Ott, T.; Genzel, R.: ,,The flare activity of Sagittarius A*", 2006, proceedings of the conference Relativistic Astrophysics and Cosmology - Einstein's Legacy -, ESO Astrophysics Symposia, in press